# Modeling of electrochemical and photoelectrochemical impedance functions for films

## Didrik Rene Småbråten

# Acknowledgment

First of all I would like to thank my supervisor Professor Svein Sunde for excellent guidance during this thesis. He has shown brilliant knowledge in the electrochemistry field through countless of discussions and working sessions, and it has been an honor to work closely with him the last year. Ph.D. Morten Tjelta and Ph.D. Lars-Erik Owe are acknowledged for the preliminary work with electrochemical and photoelectrochemical impedance calculations this thesis is based upon.

I would also like to thank to my classmates of the M.Sc. program in Chemical Engineering and fellow students at the Department of Materials Science and Engineering (DMSE) at the Norwegian University of Science and technology (NTNU) for all the academic and non-academic moments we have spent together throughout the 5 years in Trondheim. A special thanks goes to "Langemann og Støtteapparatet" for all the countless hours of funny moments we have shared.

Finally I would like to thank my family for all the support during my studies at NTNU, and for two fun years with my brother as roommates. I am certain that the studies would have been much harder without you being there for me.

# Preface

This master thesis gives a summary of the work in my final semester of the M.Sc. program in Chemical Engineering, and specialization in Material Chemistry and Energy Technology at the Department of Materials Science and Engineering, at the Norwegian University of Science and Technology (NTNU), spring 2014.

This thesis is a mathematical modeling study of electrochemical and photoelectrochemical impedance of thin films. The goal of this study is to derive mathematical models used as aid to analyze experimental data collected in impedance spectroscopy measurements of mixed conducting thin films. The study is based upon preliminary work developed by Professor Svein Sunde, Ph.D. Morten Tjelta, and Ph.D. Lars-Erik Owe. Throughout this study, the existing preliminary work has been completed, and developed further to include more impedance spectroscopy methods.

# Summary

The aim of this study was to develop mathematical models for electrochemical and photoelectrochemical impedance transfer functions for mixed conducting films. These models include electrochemical impedance spectroscopy (EIS), photoelectrochemical impedance spectroscopy (EIS), intensity-modulated photovoltage spectroscopy (IMVS), and intensity-modulated photocurrent spectroscopy (IMPS) for mixed conducting photoelectrochemical thin films, and intensity-modulated photocurrent spectroscopy (IMPS) for mixed conducting microporous thin films. In addition a short study of the step size dependency of the convergence for numerical modeling approach using Newman's BAND(J) subroutine to solve a second order diffusion equation has beed performed.

It was found that the derived photoelectrochemical impedance (EIS) transfer function and the intensity-modulated photocurrent spectroscopy (IMPS) transfer function were dependent on the degree of mixed conductivity, while the intensity-modulated photovoltage spectroscopy (IMPS) transfer function was independent with degree of mixed conductivity. This was explained by the steady-state concentration profiles for the extreme cases of $t_+ = 1$ and $t_+ = t_- = 0.5$. The concentration at solution interface increases with increasing light intensity when a sufficiently large light adsorption coefficient is assumed. For the pure electrical conducting system ($t_+ = 1$), the concentration close to the support is constant. So when the current oscillates, only the concentration close to the solution interface oscillates. For the mixed conducting system ($t_+ = 0.5$), concentration at both the electrode interfaces oscillates. Thus, the electrode kinetics at both interfaces affect the impedance measurements for an applied current density. Under open circuit conditions for IMVS measurements, only the photogenerated charge carriers close to the solution will contribute to the impedance, since the applied current is zero and the transfer function is independent of the transport numbers.

Newman's BAND(J) subroutine has been proven to be valid to solve partial differential equations with complex numbers, needed to calculate impedance spectra, in previous work. It was found in this study that the convergence of the BAND(J) subroutine does not follow the expected convergence toward the numerical solution with decreasing step size. One possible source for this unexpected trend was proposed to be that the error related to this numerical approach is dependent on higher derivatives of the solution. It was advised that a Richardson's iteration method study for higher order derivatives should be performed for this routine to find the appropriate error dependency.

The electrochemical impedance transfer function for the mixed conducting thin film electrode showed a reflective-like behavior, as expected from previous work. A dome in the low frequency region of the impedance plane plot was observed. The dome occurs at a frequency equal to the effective rate constant $k$. Thus, this dome corresponds to the charge limiting process of recombination across the bulk electrode. By decreasing the rate constant of recombination, the impedance increases, in

accordance with previous work.

The photoelectrochemical impedance transfer function for the mixed conducting thin film electrode showed two domes in the impedance plane plot with different imaginary parts in the low frequency region of the impedance spectrum corresponding to two distinct charge transfer limiting processes in opposite directions. It was found that the current associated with charge transfer limiting process oscillating in the same direction as the potential occurred at a frequency equal to the chosen effective rate constant $k$. Thus, this dome corresponds to the charge limiting process of recombination in the bulk of the electrode material. The current oscillating in the opposite direction of the potential was assumed to be associated with a back charge transfer process between the electrode and the electrolyte, and should be described by the electrode kinetics at the solution interface. In the high frequency region, the system is diffusion limited, and for high light intensities the system shows a reflective-like behavior.

The intensity-modulated photovoltage spectroscopy (IMVS) impedance transfer function for the mixed conducting thin film electrode showed one dome in the impedance plane plot. It was found that the dome occurs at a frequency equal to the chosen value for the effective rate constant $k$. Thus, the dome corresponds to the charge limiting process of recombination across the bulk electrode. For sufficiently low $k$-values, the system is charge transfer limiting in the low frequency region, and diffusion limiting in the high frequency region.

The intensity-modulated photocurrent spectroscopy (IMPS) impedance transfer function for the mixed conducting thin film electrode showed two distinct domes in the impedance plane plot in the same quadrant for large rate constants and applied steady state current densities, corresponding to two different charge limiting processes. It was found that one of the domes occurred at a frequency equal to the chosen value of the effective rate constant $k$. Thus, this dome corresponds to the charge limiting process of recombination across the electrode. The other dome is assumed to correspond to back charge transfer with the electrolyte, and the rate of the charge transfer should be described by the electrode kinetics at the solution interface. By decreasing the applied current density and increasing the light intensity, a shift in the quadrant of the impedance plane plot was observed. The proposed explanation to this is the competition between recombination and charge generation to keep the potential constant. When the rate of generation exceeds the recombination, the charge transfer at the solution interface changes direction in order to maintain a constant potential.

This was investigated in more detail for steady-state conditions, where it was found that for high rate constants the current increases with increasing light intensity to keep a constant potential, in accordance with Fick's first law of diffusion. For low rate constants the current decreases with increasing potential, thus the charge transfer between the electrode and electrolyte changes sign and the net cur-

rent density is in opposite direction than the light intensity. For intermediate rate constants, a change from increasing to decreasing current with increasing light intensity is observed. This indicates that the recombination process accommodates for the increased current by increasing the light intensity in order to keep the potential constant for low light intensities. At a threshold light intensity, the current density is changing from increasing to decreasing with increasing light intensity, indicating that the recombination cannot accommodate for the increased current by increasing the light intensity to keep the potential constant, and the potential is kept constant by changing the direction of the charge transfer between electrode and electrolyte.

The intensity-modulated photocurrent spectroscopy (IMPS) transfer function for the microporous mixed conducting thin film electrode showed a reflective-like behavior, where a charge transfer limiting process in the lower frequency limit and a diffusion controlled process in the high frequency region where observed. The charge limiting process was found to be the recombination process described by the effective rate constant $k$. The model, however, seemed to break for low rate constants, and a further study of this model was suggested.

A limitation of the derived model was that the steady-state concentration under zero light and zero illumination is zero. In previous work, an additive term in the steady-state concentration expression corresponding to the equilibrium concentration was proposed. By including an additive term directly does not fulfill the steady-state diffusion equation as written. One possible solution was proposed, in which the equilibrium concentration is introduced in the diffusion equation, and the diffusion equation is then solved with appropriate boundary conditions. This was suggested to be studied in more detail in further work.

# Sammendrag

Målet med denne oppgaven var å utlede matematiske modeller for elektrokjemiske og fotoelektrokjemiske impedance funksjoner for filmer med blandet ledningsevne. Disse modellene inkluderer elektrokjemisk impedansspektroskopi (EIS), fotoelektrokjemisk impedansspektroskopi (EIS), lysmodulert fotospenningspektroskopi (IMVS) og lysmodulert fotostrømspektroskopi (IMPS) for fotoelektrokjemiske tynnfilmer med blandet ledningsevne, og lysmodulert fotostrømspektroskopi (IMPS) for mikroporøse tynnfilmer med blandet ledningesvne. I tillegg ble en analyse av skrittlengdeavhengigheten til en numerisk fremgangsmåte for å løse partielle differensialligninger med Newman's BAND(J) subrutine utført.

Det ble vist at den fotoelektrokjemiske impedansfunksjonen (EIS) og den lysmodulert fotostrømspektroskopifunksjonen (IMPS) var avhengig av grad av blandet ledningsevne, mens lysmodulert fotospenningspektroskopifunksjonen (IMVS) var uavnheig av grad av blandet ledningsevne. Dette ble forklart ved at for den rene elektriske elektroden definert i studiet, er det bare konsentrasjonen nær elektrolyttgrenseflaten som modulerer med modulerende strøm. For en elektrode med blandet ledningsevne vil modulering av strøm påvirke konsentrasjonen nær begge grenseflatene til elektroden. Modulering av lys vil påvirke konsentrasjonen nær elektrolyttgrenseflaten i begge tilfeller. For lysmodulert fotospenningsspektroskopi (IMVS) er påført strøm konstant og lik null, så det kun er modulering av lys som påvirker konsentrasjonen nær elektrolyttgrenseflaten. Dermed er IMVS uavhengig av grad av blandet ledningsevne.

Newman's BAND(J) subrutine viste ikke forventet konvergens med skrittlengde, og en analyse av påvirkning av høyereordens deriverte ved hjelp av høyereordens Richardson's iterasjonsmetoder ble foreslått for videre studie.

Den elektrokjemiske imepdansfunksjonen (EIS) for tynnfilmelektrode med blandet ledningsevne viste en kuppel i impedansplanplottet som svarer til rekombineringsprosessen i elektroden, i samvsar med tidligere arbeid.

Den fotoelektrokjemiske impedansfunksjonen (EIS) for tynnfilmelektrode med blandet ledningsevne viste to kupler i impedansplanplottet. Det ble funnet at den ene kuppelen svarer til rekombineringsprosessen i elektroden, og den andre ble antatt å svare til ladningsoverføring fra elektrode til elektrolytt ved lav frekvens.

Den lysmodullerte fotospenningspectroskopifunksjonen (IMVS) viste en kuppel i impedansplanplottet, som ble funnet til å tilsvare rekombineringsprosessen i elektroden.

Den lysmodulerte fotostrømspektroskopifunksjonen (IMPS) viste to kupler i impedansplanplottet i samme kvadrant for lave lysintensiteter. Det ble funnet at den ene tilsvarer rekombineringsprosessen i elektroden, og den andre ble antatt å tilsvare ladningsoverføring over elektrolyttgrenseflaten

gitt av elektrodekinetikken på grenseflaten. Ved å øke lysintensiteten, redusere rekombineringshastigheten og redusere påført strøm ble et skift i kvadrant for IMPSfunksjonen observert. Dette ble forklart ved at en redusering i ladningsoverføring over elektrolyttgrenseflaten ved høy lysintensitet må skje for å opprettholde et konstant potensial om rekombineringshastigheten ikke kan kompensere for foto-genererte ladningsbærere.

En sammenheng mellom potensial, strømtetthet og lysintensitet under stasjonære betingelser ble utledet for å forklare impedansspektrene matematisk.

Det ble foreslått en videre studie av modellen for lysmodulert fotostrømsspektroskopi (IMPS) av mikroporøse elektroder med blandet ledningsevne, hvor rekombineringsprosessen sees på som hastigheten til ladningsoverføring mellom elektrode og elektrolytt langs poreoverflaten.

En begrensning med de utledede modellene er at konsentrasjonen under stasjonære betingelser blir lik null ved null påført strøm og lysintensitet. Det ble foreslått en metode å inkludere et konsentrasjonsledd i diffusjonsligningen som tilsvarer likevektskonsentrasjonen under null påført strøm og null lysintensitet. Den løste diffusjonsligningen kan kombineres direkte med modellene i dette studiet.

# Table of contents

# List of symbols

$A$    $\partial i_f/\partial c$, A mol$^{-1}$ cm

$B$    $\partial i_f/\partial(\Phi_1 - \Phi_2)$, $\Omega^{-1}$ cm$^{-2}$

$c$    concentration of neutral hole-vacancy pair, mol cm$^{-3}$

$c_e$    equilibrium concentration of neutral hole-vacancy pairs, mol cm$^{-3}$

$c_i$    concentration of species $i$, mol cm$^{-3}$

$D$    diffusion coefficient, cm$^2$ s$^{-1}$

$D_i$    diffusion coefficient of species $i$, cm$^2$ s$^{-1}$

$F$    Faraday constant, 96485 C mol$^{-1}$

$i$    current density, A cm$^{-2}$

$I_0$    light intensity, mol cm$^{-2}$ s$^{-1}$

$I(t)$    total time-dependent current, A

Im( )    imaginary part of complex number in parenthesis

$j$    complex number, $\sqrt{-1}$

$k$    effective rate constant, s$^{-1}$

$k_B$    Boltzmann constant, $1.38 \times 10^{-23}$ J K$^{-1}$

$L$    electrode thickness, cm

$N_a$    acceptor dopant concentration, cm$^{-3}$

$N_d$    donor dopant concentration, cm$^{-3}$

$N_i$    flux of species $i$, mol cm$^{-2}$ s$^{-1}$

$q_i$    charge of species $i$, C cm$^{-2}$

$R$    gas constant, 8.314 J K$^{-1}$ mol$^{-1}$

$R_{CT}$    charge transfer resistance, $\Omega$ cm$^2$

$R_E$    electrolyte resistance, $\Omega$ cm$^2$

Re( )    real part of complex number in parenthesis

$s$    Laplace variable

$t_i$    transference number of species $i$

$T$    temperature, K

$u'_i$    mobility of species $i$, cm$^2$ (Vs)$^{-1}$

$V(t)$    total time-dependent voltage, V

$x$    coordinate normal to the electrode, cm

$y$    dimensionless coordinate, $x/L$

$z_i$    charge number of species $i$

$Z$    impedance, $\Omega$ cm$^2$

$Z_D', Z_D''$   diffusion impedances, $\Omega$ cm$^2$

Greek

$\alpha$   light adsorption coefficient, cm$^{-1}$

$\partial$   partial derivative

$\kappa$   electrode conductivity, $\Omega^{-1}$ cm$^{-1}$

$\nabla$   del-operator, $\hat{x}\partial/\partial x + \hat{y}\partial/\partial y + \hat{z}\partial/\partial z$

$\mu_e$   electrochemical potential of electrons in electrode backing, J mol$^{-1}$

$\mu_h$   electrochemical potential of holes in electrode, J mol$^{-1}$

$\nu_+$   number of holes per electron extracted

$\nu_-$   number of proton vacancies per electron extracted

$\sigma$   electrolyte conductivity, $\Omega^{-1}$ cm$^{-1}$

$\theta$   phase shift

$\Phi_1, \Phi_2, \Phi_M$   electrode, electrolyte and metal support potentials, V

$\omega$   angular frequency, s$^{-1}$

Subscripts

$i$   species number

1   electrode phase in mixed conducting system

2   electrolyte phase in mixed conducting system

$f$   faradaic

$M$   metal support

$W$   Warburg

Superscripts

0   reference value

Overline

$\sim$   time-dependent part of quantity

$\wedge$   unit vector

Others

$\mathscr{L}\{\}$   Laplace transform

# 1 Introduction

## 1.1 Background

Earth's population has exceeded 7 billion, and prognoses say that the increase in earth's population will continue until it flattens at around 10 billions [1]. With a continuous increase in the standards of living and industrialization of the third world countries, the worlds energy demand will grow in a large extent the next years. The historical and predicted energy demand for different energy resources is given in Figure 1.1 [2].
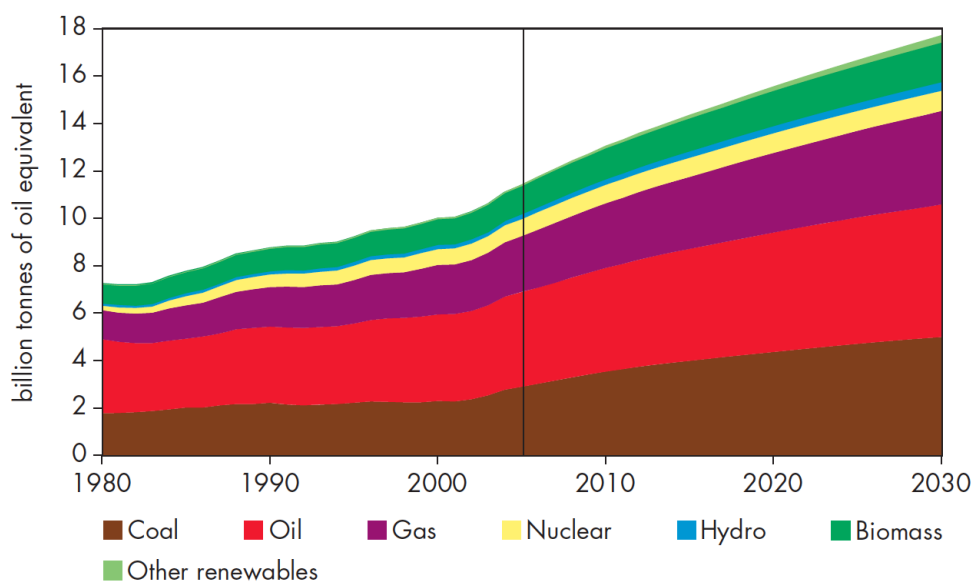


Figure 1.1: The historical and predicted energy demand for different energy sources. From [2].

From Figure 1.1 it can be seen that most of the energy demand is supplied by high $CO_2$ emitting, non-sustainable energy sources, like oil and coal. The largest source to $CO_2$ emission is energy produced from fossil fuels, where the emission has increased with 145% the last 30 years [3]. Researchers agree that the emission of greenhouse gases, as $CO_2$, methane and nitrous gases, may contribute to global warming.

Solar energy is a promising low $CO_2$ emitting, sustainable energy source to meet the future energy demand. Solar irradiation supplies energy equal to the earth's entire annual energy demand in about 1.5 hours [4]. However, there are issues regarding the utilization, harvest and storage of this energy, and there is a constant research in the solar energy technology field. Photovoltaic cells or photovoltaics, commonly known as solar cells, convert light energy to usable energy in form of electricity.

## 1.2 Semiconductor technology and solar cells

Solar cells are based on semiconducting materials. In order to explain the working principle of photovoltaics, a brief introduction to semiconductors and semiconductor technology is required.

### 1.2.1  Electronic structure of materials used for electronics

There are three types of materials used in electronics; metals, insulators, and semiconductors. These are characterized by the electronic conductivity, where metals have a high conductivity, insulators a very low conductivity, and semiconductors are located between these to extrema. The difference in the electronic conductivity of these material groups may be explained by the electronic structure of the materials. For a crystalline solid, electrons are allowed to travel in quasi-continuos bands. These quasi-continuous bands, referred to as energy bands, are caused by overlap between allowed energy states in each atom (a more detailed description can be found elsewhere []). The allowed energy bands may accommodate for $2N$ electrons, where $N$ is the total number of electrons in each unit cell of the crystal. The energy bands may either be separated by quasi-continuos forbidden energy bands (referred to as band gaps), or overlap in energy. The highest energy band occupied by electrons is referred to as the valence band (VB), and the following energy band, that is, the lowest unfilled energy band is referred to as the conduction band (CB).

The characteristics of the different materials are explained by how the valence band and conduction band are filled and separated. Metals typically either have a partially filled valance band, or overlapping completely filled valance band and conduction band as sketched in Figure 1.2a and 1.2b, respectively. Electrons in the valence band are easily excited, as there are accessible energy states close to the electron. Insulators are characterized by having a completely filled valence band and a completely empty conduction band, separated by a large band gap $E_g$ as sketched in Figure 1.2c. Electrons does not excite in the conduction band as there are no energy states available in the valence band, and the energy barrier to excite electrons across the band gap is to large at room temperature. Semiconductors are similar to insulators in electronic structure, where a completely filled valence band and completely empty conduction band is separated by a band gap $E_g$ as sketched in Figure 1.2d. However, for semiconductors the band gap is of a magnitude so that electrons may excite across the band gap under room temperature and the conduction band conduct electricity. There are also available states in the valence band for electrons to excite, and the valance band also contributes to the conduction. Distinction of insulators and semiconductors can be quite ambiguous, but as a rule of thumbs insulators are defined by a band gap exceeding 2-3 eV.

### 1.2.2  Semiconductors under illumination

When a semiconductor is illuminated, electrons may excite across the band gap if the photon energy exceeds the size of the band gap [5]. If excited electrons can be extracted from the conduction band in an outer circuit, we have a generated photocurrent. This is sketched schematically in Figure 1.3, where electrons are drained from the conduction band, forced through an outer circuit, and fed to
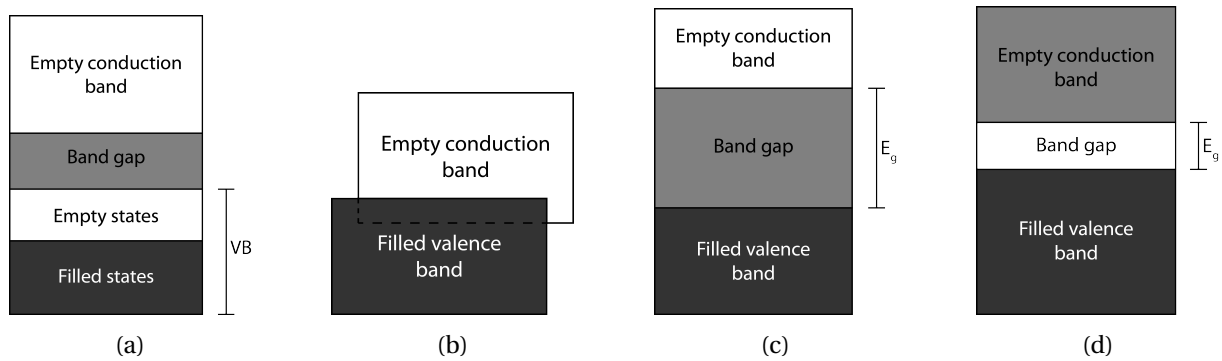
Figure 1.2: Different electronics material types. a Metal with partially filled valance band and conduction band. b Metal with overlapping valance band. c Insulator with a large band gap. d Semiconductor with a lower band gap.

the valence band to maintain charge neutrality. Thus, the incident light energy is transformed into usable energy in form of an electric current. The photogenerated current may be fed directly to the local energy mixture, or stored by different storage methods. The same analogy may be used for
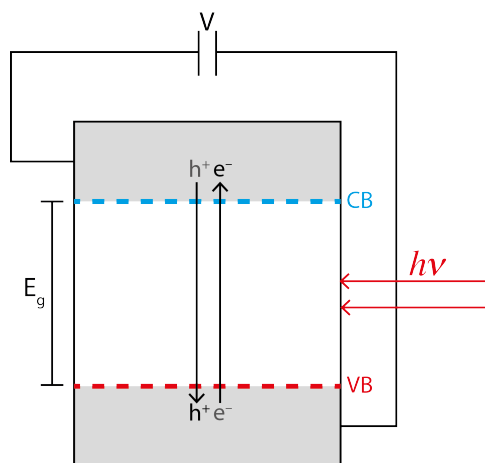


Figure 1.3: Sketch of generated photocurrent in a semiconductor. Electrons excite from the valence band to the conduction band, drained from the conduction band and forced through an outer circuit where it is utilized, and fed to the valence band to maintain charge neutrality. Here $h\nu$ represents the photon energy.

holes, as they excite simultaneously from the conduction band to the valence band, drained from the valence band and forced through the outer circuit, and finally fed to the conduction band. Thus, the flow of negative and positive species are defined in opposite directions.

### 1.2.3 Conventional heterojunction solar cells

Industrially, conventional silicon (Si) based solar cells are the largest on the market. Silicon is quite abundant, and the Si-based solar cells have a reasonable efficiency. Essentially, a conventional Si-based solar cells consists of two Si-materials with different charge concentration in a heterojunction. One of the Si-materials is doped with an element with an excess of electrons compared to Si, typically

phosphor (P), and is referred to as an $n$-type semiconductor. The other material is doped with an element with a deficit of electrons, typically boron (B), and is referred to as a $p$-type semiconductor. When these two semiconductor materials are connected in a junction, the charge carrier concentration difference causes diffusion of majority carriers across the junction, that is, holes from $p$-side to $n$-side and electrons from $n$-side to $p$-side. This creates a potential barrier close to the junction referred to as the depletion layer. When minority carriers (holes in the $n$-type material and electrons in the $p$-type material) are excited close to the depletion layer, they are immediately swept across the junction by the potential across the junction causing an increase in the current. These processes are described in Figure 1.4.

There is extensive research on even more promising solar cell technologies than the conventional to either reduce the cost or increase the efficiency, preferably both simultaneously. These technologies include, amongst others, thin film solar cells, intermediate band solar cells, and photoelectrochemical solar cells. In this study, photoelectrochemical cells are studied in more detail.



Figure 1.4: Illustrative sketch of the depletion layer across the pn-junction, and the current caused by excited minority carriers that are swept across the depletion layer.

## 1.3   The photoelectrochemical system

### 1.3.1   Electrochemical photovoltaic cells

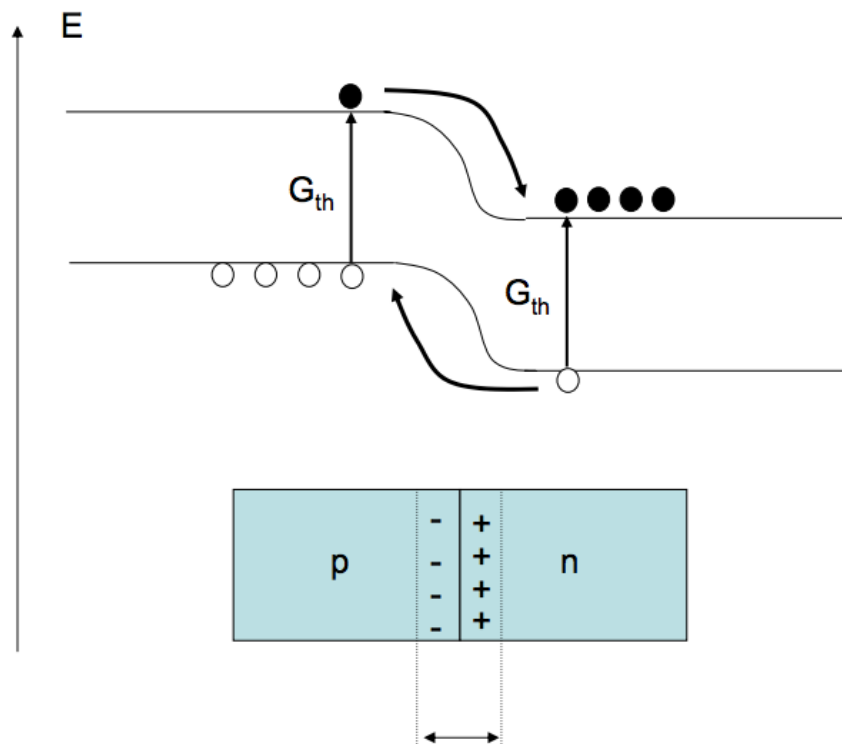In traditional solar cells, such as Si-based solar cells, the system consists of two solids with similar electronic structure but different charge concentration in a heterojunction. In a photoelectrochemical cell, however, the potential barrier is created by a liquid phase rather than another solid phase, as described below.

If a semiconductor electrode is brought in contact with an electrolyte, a potential barrier may be created at the surface of the electrode [5]. When the interface is illuminated and the semiconducting electrode is connected to a conducting counter-electrode, a photocurrent may flow between the electrodes. The most important process of creating a photocurrent is the generation of electron-hole pairs in the bulk of the semiconductor as described above. In the presence of a depletion layer, the majority carriers will be transported into the interior of the electrode and minority carriers will be transported to the surface [6]. If transfer to a redox couple in the electrolyte whose energy lies within the band-gap can take place, a photocurrent is seen. This process is described below.

An $n$-type is assumed to be semiconductor is immersed in an electrolyte with a redox couple, that is, containing an oxidized (Ox) and reduced (Red) state of a species. Under illumination, minority carrier holes generated in the semiconductor move to the electrolyte interface where the redox couple in the electrolyte is oxidized [6]

$$\text{Red} + h^+ \rightarrow \text{Ox}^+ \tag{1.1}$$

When the semiconductor is connected to a counter electrode immersed in the same electrolyte, electrons reduce the redox couple at the counter electrode interface by

$$\text{Ox}^+ + e^- \rightarrow \text{Red} \tag{1.2}$$

A schematic of such a photoelectrochemical cell is given in Figure 1.5 [5]. Here, an $n$-type titanium oxide ($TiO_2$) semiconductor is immersed in an $Fe^{2+}/Fe^{3+}$ redox couple electrolyte, and connected to a platinum (Pt) counter electrode. The redox couple is oxidized at the semiconductor and reduced at the counter electrode.

### 1.3.2   Operating principle og dye-sensitized solar cells (DSSC)

Commercially available photovoltaic solar cells up to now are based on inorganic materials, which require high costs and highly energy consuming preparation methods. Several of the conventional materials are also toxic. The use of organic materials have been proposed to solve these issues. However, conventional organic heterojunction photovoltaic cells have a significantly lower efficiency

$$Fe^{2+} + h^+ \rightarrow Fe^{3+} \qquad\qquad Fe^{3+} + e^- \rightarrow Fe^{2+}$$
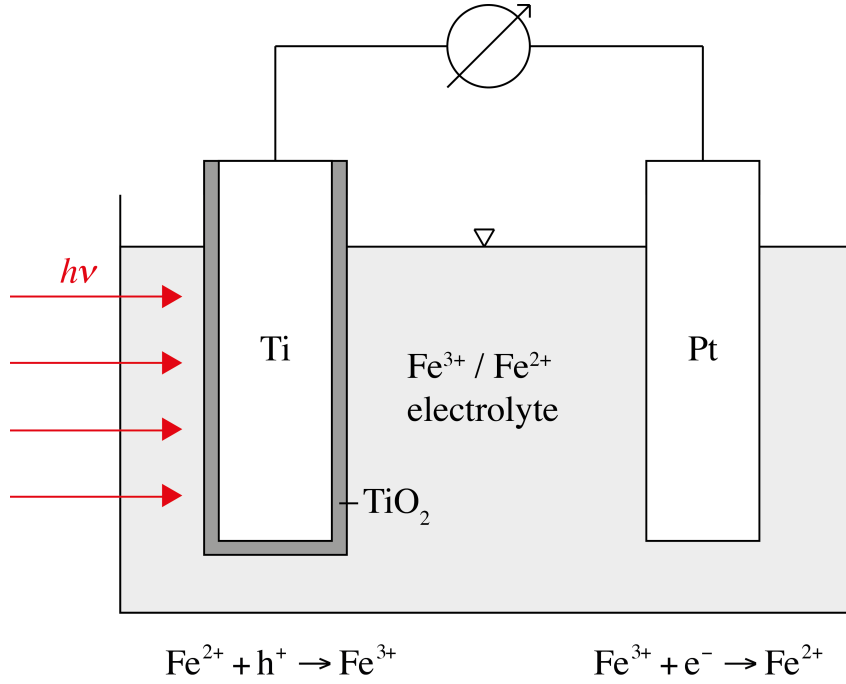
Figure 1.5: Example of an electrochemical photovoltaic cell consisting of a $TiO_2$ semiconductor anode, a Pt counter electrode cathode, and an $Fe^{3+}/Fe^{2+}$ redox couple electrolyte. From [5].

compared to the commercial inorganic photovoltaic cells [7]. The organic materials should have both good light harvesting properties and good carriers transport properties which is difficult to achieve.

Dye-sensitized solar cells (DSSC) are promising organic-based photoelectrochemical cells that may solve many of the issue with organic photovoltaics. DSSCs separates the two requirements above, as the light harvesting is done by a semiconductor-dye interface and charge transport is done by the semiconductor and the electrolyte [7]. A schematic of a DSSC is given in Figure 1.6. A porous $TiO_2$ semiconductor film is mounted on a transparent conductive oxide (TCO), and an organic sensitizer material consisting of a ruthenium complex is adsorbed onto the $TiO_2$ particle surface. The semiconductor is immersed in a triiodide/iodine redox couple electrolyte. A Pt counter electrode immersed in the electrolyte is connected in an outer circuit with the semiconductor through the TCO. [7].

Under illumination, the dye $S$ absorbs photons to an excited sensitizer state $S^*$. The excited state injects an electron in the conduction band of the semiconductor $TiO_2$, leading to an oxidized sensitizer state $S^+$. The electron is transferred to the counter electrode through an external circuit. At the counter electrode the electron is ejected by reducing the triiodide/iodine redox couple. The reduced redox couple then regenerates the oxidized dye. These operating principles may be summarized by the following chemical reactions [7]

$$S_{(ads)} + h\nu \rightarrow S^*_{(ads)} \tag{1.3}$$

$$S^*_{(ads)} \rightarrow S^+_{(ads)} + e^-_{(inj, \, TiO_2)} \tag{1.4}$$
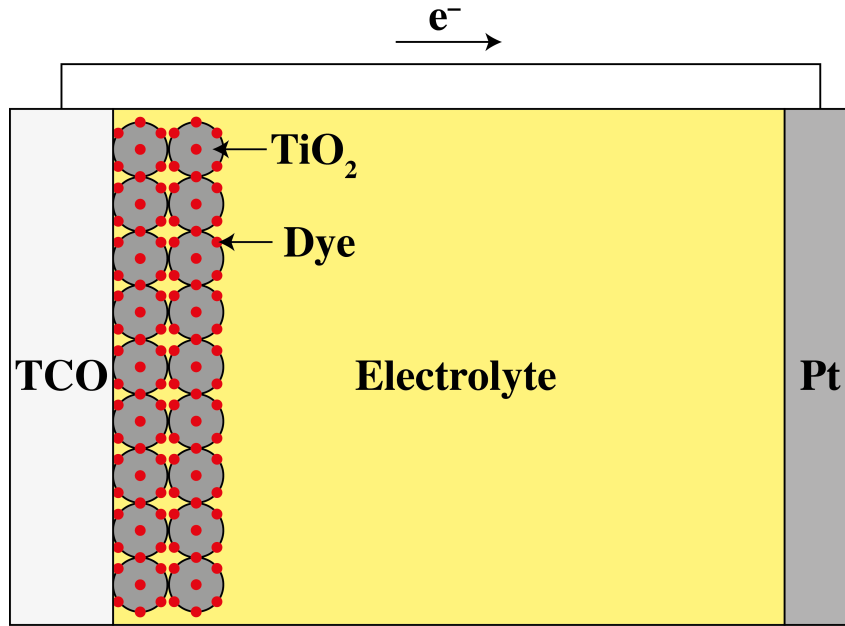
Figure 1.6: Schematic representation of the dye-sensitized solar cell. A ruthenium-complex sensitizer are adsorbed on the $TiO_2$ semiconductor particles mounted on a transparent conducting oxide (TCO). The Pt counter electrode is connected to the semiconductor through an outer circuit and through the triiodide/iodine redox couple electrolyte.

$$I_3^- + 2e_{(Pt)}^- \rightarrow 3I^- \tag{1.5}$$

$$S_{(ads)}^+ + \frac{3}{2}I^- \rightarrow S_{(ads)} + \frac{1}{2}I_3^- \tag{1.6}$$

### 1.3.3 Photoelectrochemical water splitting

Photoelectrochemical water splitting is a photoelectrolysis cell that utilizes illumination to produce hydrogen by water electrolysis [6]. Water electrolysis by photoelectrolysis is said to be the most green solution to produce hydrogen. No emission of greenhouse gases is associated in the production process, as the energy supplied is emission free (here the production process of the photoelectrochemical system is neglected).

An *n*-type semiconductor is assumed to be immersed in a redox couple electrolyte. At the semiconductor interface an oxidation reaction occurs. For the case of water splitting, the reaction at the semiconductor is [6]

$$H_2O + 2p^+ \rightarrow \frac{1}{2}O_2 + 2H^+ \tag{1.7}$$

At the counter electrode the reduction reaction

$$2H^+ + 2e^- \rightarrow H_2 \tag{1.8}$$
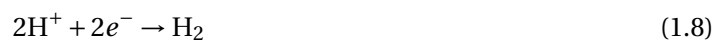
occurs, which give the net process reaction

$$2H_2O \rightarrow 2H_2 + O_2 \tag{1.9}$$
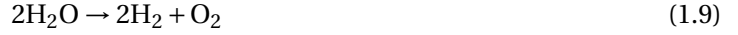
A schematic figure of such a photoelectrochemical water splitting cell with a TiO$_2$ semiconductor electrode, a Pt counter electrode and a KOH electrolyte [5] is given in Figure 1.7. Here, H$_2$O is the redox couple. The electrolyte consisting KOH is present to serve as a medium for charge transfer between the electrodes without short circuiting the system.
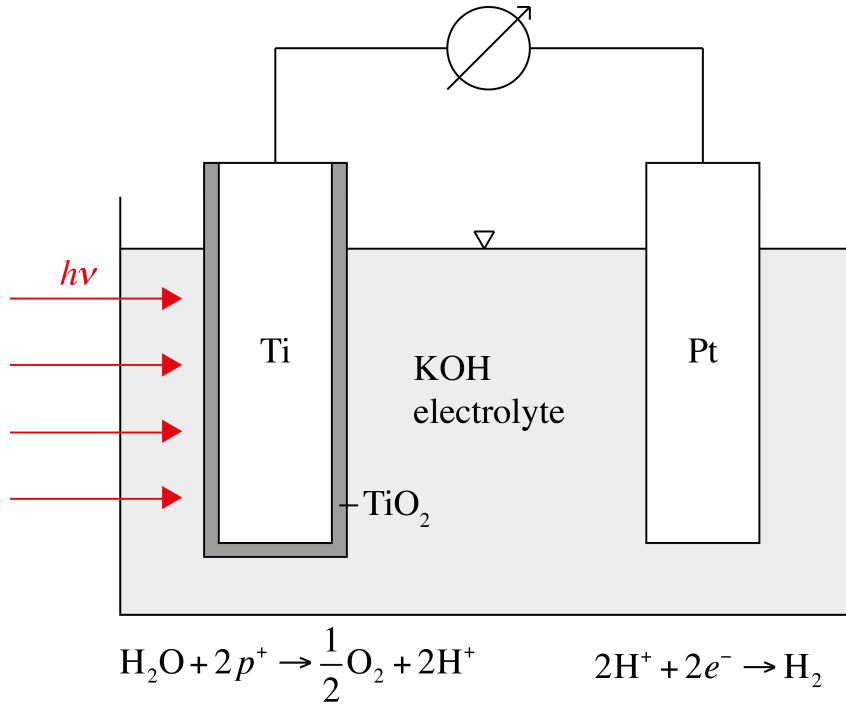


Figure 1.7: Example of a photoelectrochemical water splitting cell consisting of a TiO$_2$ semiconductor anode, a Pt counter electrode cathode, and an KOH electrolyte.

### 1.3.4   Aim of this study

Modeling of impedance transfer functions reported in the literature is usually performed for pure electrical conducting electrode systems. In this study, we introduce mixed electronic/ionic conductivity to the modeled electrode system, and investigate how this introduction of mixed conductivity affect the charge flow, and thus the impedance transfer functions, in photoelectrochemical systems. We propose that mixed conducting systems may show significantly different charge flows than pure electrical conducting systems, depending on the degree of mixed conductivity. This will be investigated by comparing calculations for a nearly pure electrical conducting system and the other extrema of equal transport numbers.

An investigation on the physical properties for the modeled system that may be described by

impedance spectra will be investigated, and what material properties may be extracted from the calculated spectra.

## 2  Impedance measurement techniques and representation

### 2.1  Introduction

In this section, the principle of impedance spectroscopy measurements, representation of impedance spectra, and introduction to the modeled impedance transfer functions are described. In Section 2.2 the motivation and principle for impedance spectroscopy measurements to investigate electrical properties of materials is introduced. An introduction to the methods for representation of impedance spectra used in this study is given in Section 2.3. In Section 2.4 we give a quick introduction to analysis of impedance spectra, and describe typical trends in impedance spectra by assuming a half electrode system where an electrode is immersed in an electrolyte. Photoelectrochemical impedance spectroscopy (EIS) is described in Section 2.5. Intensity-modulated photovoltage spectroscopy (IMVS) is described in Section 2.6 and intensity-modulated photocurrent spectroscopy (IMPS) is described in Section 2.7. The expected trends in these measurements are found in the literature described below. In Section 2.8, modeling with equivalent circuits is introduced, and in Section 2.9 the mathematical treatment of impedance spectroscopy by Laplace transform is introduced.

### 2.2  Impedance spectroscopy and the importance of interfaces

The interface of a material is important in the study of material properties. Physical properties – crystallographic, mechanical and electrical – change rapidly at an interface and polarization reduce the conductivity of the system [8]. Each interface in the system will polarize differently when subjected to an applied potential difference. The rate of polarization change when the applied voltage is reversed is characteristic for the interface type; slow for chemical reactions at the electrode–electrolyte surface, substantially faster in the aqueous electrolyte [8].

Impedance spectroscopy (IS) is a characterization method where electrical properties and interfacial transfer processes in a system can be determined. In impedance spectroscopy measurements, a harmonically modulated electrical stimulus is applied to the electrodes and the modulating response is measured.

$$Z(t) = \frac{\text{response}(t)}{\text{stimulus}(t)} \tag{2.1}$$

The electrical response is a result of several microscopic processes throughout the system. Amongst the processes, and usually the most important in the characterization of the electrical properties of the system, are charge transport through the electrode and electrolyte phases, and charge transfer across heterogeneous interfaces. For a semiconductor under illumination, a contribution from the generation of photocurrent when electrons are excited gives a contribution to the electrical response. Application of modulating potential forces these processes to oscillate with the applied frequency. If

a reversible couple is present at the electrode surface, the concentrations of both the reduced and oxidized species will also oscillate not only at the surface but away of the electrode [5]. The motion of charge across the system is thus affected by the ohmic resistance in the different phases, and the rate of the charge transfer at the interfaces [8]. Usually, the impedance defined by (2.1) is referred to as an impedance transfer function, since it gives a relation of the change in phase and amplitude of the stimulus and response across an electrical system.

Impedance spectroscopy measurements are well suited to characterize the electrical behavior of the system, including characterization of the motion of charge control and measuring material properties like diffusion coefficients, rate constants, mobilities, transport numbers and conductivities. It may be used to investigate the dynamics of charge species of any kind of solid or liquid material: ionic, semiconducting, mixed ionic-electronic and so on [8].

There are several impedance spectroscopy techniques, where single-frequency impedance spectroscopy is the most common and will be modeled in this study. One single frequency of the electrical stimulus is chosen, and the phase shift and amplitude of the electrical response is measured. This process is then repeated across a frequency range, typically between 1 mHz to 1MHz [8], and a series of data is collected. In this study we will investigate the impedance spectroscopy transfer functions photoelectrochemical impedance spectroscopy (EIS), intensity-modulated photovoltage spectroscopy (IMVS), and intensity-modulated photocurrent spectroscopy (IMPS).

### 2.3   Representation of impedance spectra

The phase shift and amplitude of the impedance can be used to represent the impedance as a complex number

$$Z = \text{Re}(Z) + j\,\text{Im}(Z) = |Z|\cos\theta + j|Z|\sin\theta \tag{2.2}$$

This relation can be represented in an impedance plane plot, often referred to as Nyquist plot [5], where the impedances at different frequencies are plotted as a planar vector in the real and imaginary plane given by Eq. (2.2). As an example, an impedance plane plot for a Ni/Ti-doped YSZ solid-oxide fuel cell (SOFC) is given in Figure 2.1.

These plots give a good representation of the phase shift and amplitude of the impedance. However, it can be difficult to determine at which frequency each point in the plot is measured. The impedance plane plot often does not give the frequency at each measured point explicit. This can be shown explicit by plotting the impedance versus the frequency in a Bode plot [5]. Typically, the imaginary part of the impedance is plotted if an investigation of the phase shift is required, and the magnitude is plotted if an investigation of the resistance is required. A Bode plot of the electrical impedance spectrum of a microporous $TiO_2$ dye-sensitized solar cell (DSSC) is given in Figure 2.2
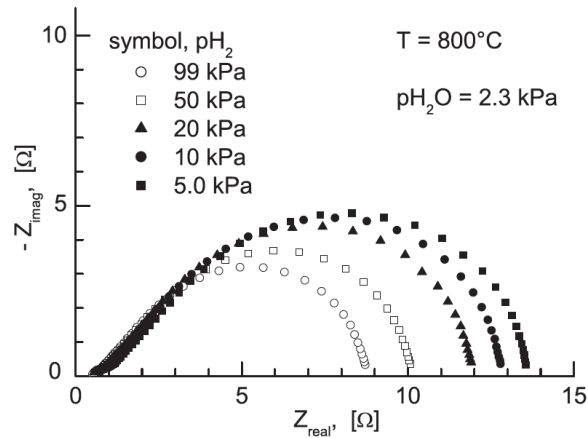
Figure 2.1: Impedance plane plot representation of the impedance for a Ni/Ti-doped YSZ SOFC as a function of $P_{H_2}$. From [9].

[10], where solid symbols represent the imaginary part of the impedance, and the open symbols represent the magnitude of the impedance.
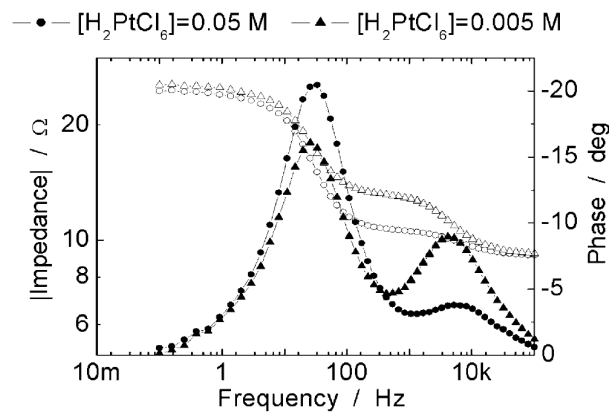


Figure 2.2: Bode representation of the electrical impedance spectrum for a DSSC with different concentration of Pt at the counter electrode. From [10].

## 2.4 Analysis of impedance spectra

We assume a half electrode system where an electrode is immersed in an electrolyte. It can be shown [5] that the current flow in the system is given by an electron-transfer resistance across the interface, $R_{CT}$, and a Warburg impedance across the diffusion layer, $Z_W$, in series. In practice, this is connected in parallel with the double layer capacitance, $C_D$, and in series with the electrolyte resistance, $R_E$ [5]. An equivalent circuit of this half-cell system is given in Figure 2.3.

### 2.4.1 Diffusion limited process

For a diffusion limited process, the Warburg diffusion impedance is rate determining. In an impedance plane plot, it can be shown that the diffusion impedance is a straight line for all frequencies [5]. In
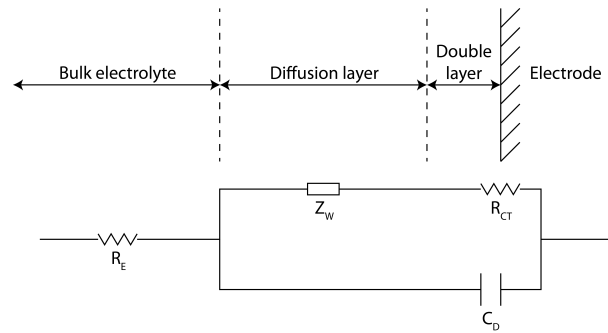
Figure 2.3: Equivalent circuit for the electrode half-cell. $R_{CT}$ is the charge transfer resistance, $Z_W$ is the Warburg impedance, $C_D$ is the double layer capacitance, and $R_E$ is the electrolyte resistance.

general, a system is diffusion controlled for a specific frequency region if the impedance plane plot is a straight line with an inclination angle $-\phi = \alpha = 45°$ for all frequencies within the region. Physically, the system shows a infinite-Warburg-like diffusion impedance behavior in this frequency region.

### 2.4.2   Charge-transfer limited process

We assume that the Warburg diffusion impedance becomes sufficiently small compared to the charge transfer so that the equivalent circuit in Figure 2.3 is reduced to that of Figure 2.4a [5]. In this limiting case, the system is only electron-transfer limited. It can be shown [5] that the impedance plane plot gives a perfect semi-circle. The length of the real part of the semi-circle equals the charge transfer resistance, and the center of the semi-circle is located at a frequency of $\omega = 1/R_{CT}C_D$. Thus, the double-layer capacitance can be investigated for this plot. A schematic impedance plane plot of an electron-transfer limited process is given in Figure 2.4b. The system effectively charges and discharges the electrical double layer in this frequency region.
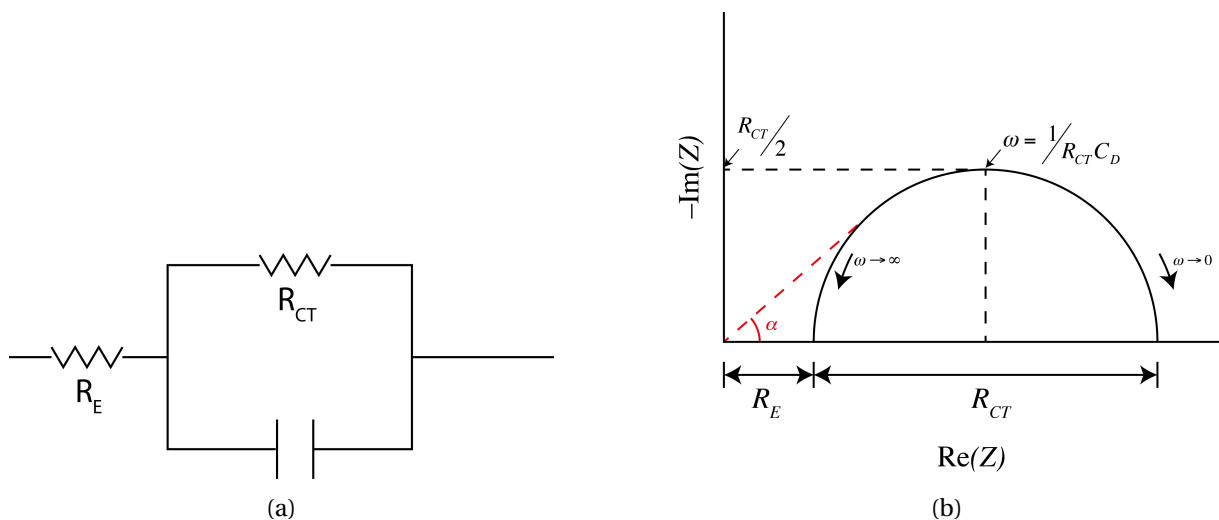


Figure 2.4: a Equivalent circuit for a rate limiting process, and b impedance plane plot for a rate limiting process. $R_{CT}$ is the charge transfer resistance, $C_D$ the double layer capacitance, and $R_E$ the electrolyte resistance.

## 2.5   Photoelectrochemical impedance spectroscopy (EIS)

In photoelectrochemical impedance spectroscopy (EIS) a harmonically modulated voltage $V(t) = V_0 \sin(\omega t)$ with angular frequency $\omega$ is applied, and an AC current $i(t) = i_0 \sin(\omega t + \phi)$ results. A phase difference $\phi$ between the stimuli and response may be observed [10]. $I_0$ and $V_0$ are the steady-state current and voltage, respectively. The EIS signal is the electrical impedance

$$Z(j\omega) = \frac{V(\omega)}{i(\omega)} \tag{2.3}$$

where $V(\omega)$ and $I(\omega)$ are the modulating perturbation in the voltage and current, respectively.

The equivalent circuit for the electrical impedance spectroscopy setup is given in Figure 2.5, where $\Phi_0$ is the incident light intensity. EIS measurements can be performed under any bias illumination, either for one wave length, one sun, or several suns, depending on the wanted conditions
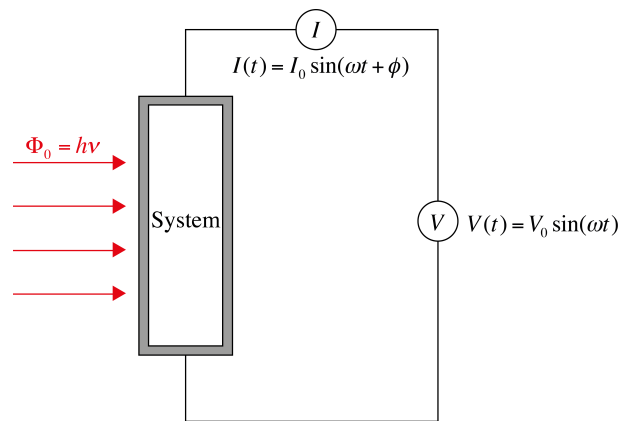


Figure 2.5: Equivalent sketch of an EIS measurement. $\Phi_0$ is the incident light intensity, $\omega$ the angular frequency, $\phi$ the phase shift, and $I_0$ and $U_0$ are the steady-state current and voltage, respectively.

Photoelectrochemical impedance modeling is not reported extensively in the literature. Södergren et al. [11] define a diffusion equation which takes photogenerated charge carriers under illumination into account

$$D\frac{\partial^2 n(x)}{\partial x^2} - \frac{n(x) - n_0}{\tau} + I_0 \alpha e^{-\alpha x} = 0 \tag{2.4}$$

The photoelectrochemical impedance spectrum is characterized by the assumed or designed interfaces in the system. Kim et al. [12] observed three distinct charge transfer limiting processes in multilayer stacked $TiO_2$ nanoparticle photoelectrodes, as shown in Figure 2.6. It was found that these processes where corresponding to charge transfer at the counter electrode, charge transfer at the $TiO_2$ electrode, and Nernstian diffusion within the electrolytes.

Kern et al. [10] similarly observed three charge limiting processes for modeled photoelectrochemical impedance spectra, as shown in Figure 2.7
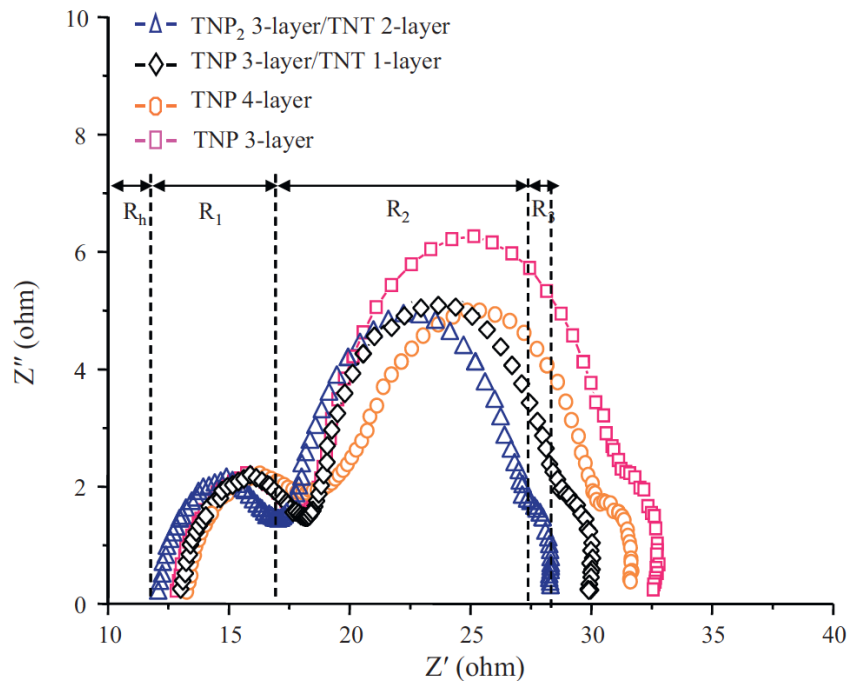
Figure 2.6: EIS results of the DSSCs fabricated with multilayer TNP/TNT combined electrodes. From [12].
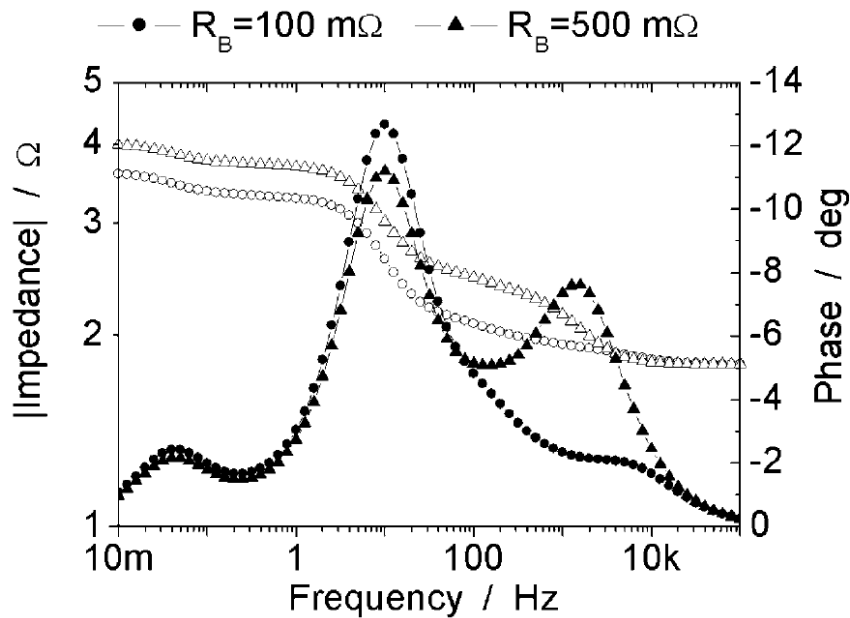


Figure 2.7: Calculated EIS with variation of the resistance of the boundaries. The high frequency peak increases and shifts to lower frequencies, as RB increases from 100 to 500 mV. open symbols, $|Z|$; solid symbols, phase $\phi$. From [10].

Hoshikawa et al. [13], however, showed by photoelectrochemical impedance measurements of dye-sensitized solar cells that their internal resistance consisted of at least five components, shown in Figure 2.8. This indicates five interfaces in the photoelectrochemical system with distinct time constants for charge transfer transport.
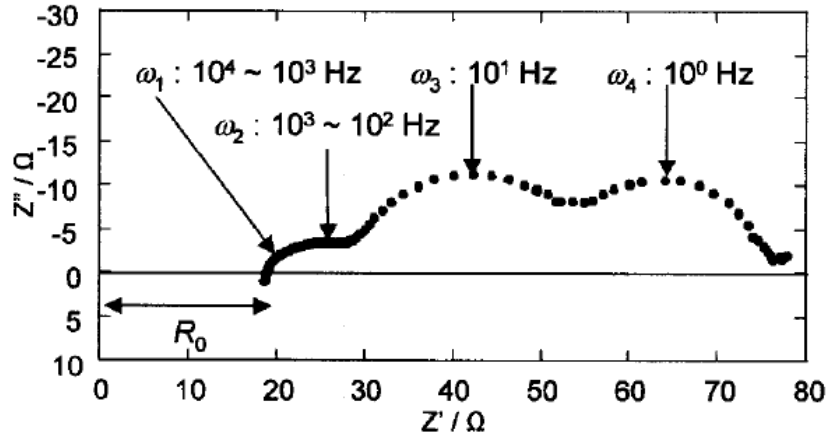


Figure 2.8: An impedance spectrum in Nyquist presentation obtained from $TiO_2$-based standard dye-sensitized solar cell. Bias, OCV; light intensity, 100 mW cm$^{-2}$. Electrolyte: 0.6 M DMPImI, 0.1 M LiI, 0.05 M $I_2$, 0.5 M t-BuPy in methoxyacetonitrile. Structure of cell: FTO|$TiO_2$(P25)|dye($RuN_3$)|electrolyte|sputtered Pt (FTO). From [13].

## 2.6 Intensity-modulated photovoltage spectroscopy (IMVS)

Intensity-modulated photovoltage spectroscopy involves measuring a modulating photovoltage under open-circuit conditions when illuminated with a modulating light intensity. Kern et al. [10] states that under illumination by a steady-state bias illumination $I_0$, superimposed by a harmonically perturbed light intensity, $I_{AC} = \Delta I e^{i\omega t}$, the measured photovoltage $V$photo under open-circuit conditions consists of a large stationary photovoltage $V_0$ and a small transient component $V_{AC}$ varying with the light frequency and a phase shift $\phi$ between the modulating light and the resulting AC voltage signal

$$V_{\text{photo}} = V_0 + \underbrace{\Delta V e^{i(\omega t - \phi)}}_{V_{AC}} \tag{2.5}$$

The IMVS-transfer function is defined by the fraction of measured photovoltage and modulating illumination [10]

$$Z_{\text{IMVS}}(\omega) = \frac{\Delta V}{\Delta I_0} \tag{2.6}$$

Slichthörl et al. [14] describes the IMVS response by looking at the transport equation for a sinusoidal modulated light intensity

$$\frac{\partial n}{\partial t} = D\frac{\partial^2 n}{\partial x^2} - kn + \eta I_0 \alpha e^{i\omega t} e^{-\alpha x} \tag{2.7}$$

where $n$ is the sum of photoinduced electron concentration and trap states, $k$ is the rate constant of recombination, $\eta I_0 \alpha e^{i\omega t} e^{-\alpha x}$ is a generation term $G(x, t)$, and $\eta$ accounts for reflection losses. $I_0$ and $\alpha$ are the light intensity and penetration depth, respectively. A similar transport equation is reported numerous in the literature [15, 16, 10], where Peter et al. [15] define $\tau = k^{-1}$ as the electron lifetime.

The IMVS response is typically a semicircle with positive real part and negative imaginary part, as reported by Peter et al. [15] in Figure 2.9. Here the boundary conditions [15]

$$D_n \frac{\partial n}{\partial x}\bigg|_{x=0} = k_{\text{ext}} n_{x=0}; \qquad \frac{\partial n}{\partial x}\bigg|_{x=d} = 0 \tag{2.8}$$

is assumed, where $k_{\text{ext}}$ is the rate constant for electron extraction at the substrate ($x = 0$) and $d$ the film thickness. For IMVS measurements, $k_{\text{ext}} = 0$. It is found that the minimum of the impedance plane plot of the IMVS response is located at a frequency $\omega_{\text{min}} = \tau_n^{-1} = k$ [15, 16, 10].
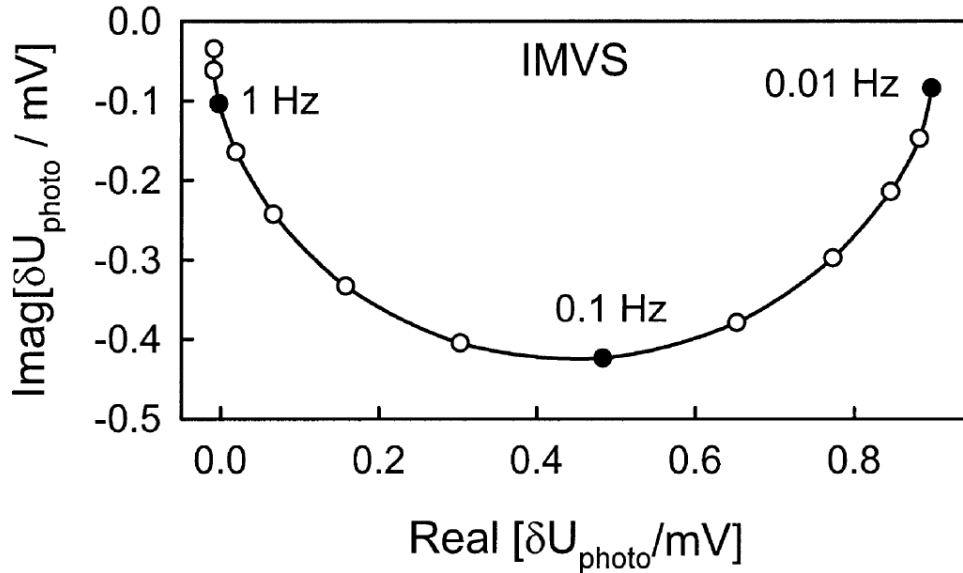


Figure 2.9: Typical IMVS plots for DSSC at dc intensity $\sim 4 \times 10^1 3 \text{ cm}^{-2} \text{ s}^{-1}$. From [15].

Schlichthörl et al. [17] investigate the charge-recombination kinetics and band edge movement in dye-sensitized nanocrystalline $TiO_2$ solar cells (DSSC) by IMVS. They assume that optical excitation leads to an injection current density, $J_{\text{inj}}$, into the conduction band, and also a irreversible current density caused by recombination $J_r$. They proceed to express the accumulated charge in the conduction band $Q_{cb}$ and in surface states $Q_{ss}$ as a function of the rate constant of electron capture by surface states, thermal emission of electrons back into the conduction band, back electron transfer from the conduction band, and back electron transfer from surface states to an electron acceptor at the electrode/electrolyte interface. This is given in the electron-transfer kinetic scheme in Figure 2.10. The modeled IMVS response consists of one or two semi circle minima, depending on the rate constants of the physical processes in the system described above. This is given in Figure 2.11. $\tau_1$
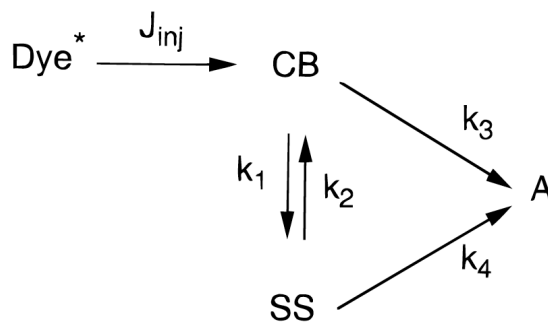
Figure 2.10: Scheme for electron-transfer kinetics. $J_{inj}$ is the electron-injection current from excited dye molecules into the semiconductor conduction band, $k_1$ and $k_2$ are the respective rate constants for electron capture by surface states and the thermal emission of electrons back into the conduction band, and $k_3$ and $k_4$ are the respective rate constants for the back electron transfer from the conduction band and surface states to an electron acceptor at the nanocrystalline semiconductor/redox electrolyte interface. $J_{inj}$ is assumed to not limit the recombination kinetics. Electron transfer from the semiconductor to the oxidized dye and charge injection from the redox electrolyte to the semiconductor are neglected. From [17].

and $\tau_2$ are the two different time constants given by the electron-transfer kinetics, $S$ and $T$ are linear combinations of the electron kinetics. Thus, detailed information of the recombination kinetics and edge movements may be obtained by IMVS with this model.

Kern et al. [10] describes a similar reaction path scheme as Schlichthörl et al. [17], given in Figure 2.12. $k_1$ and $k_2$ are the rate constants for trapping and detrapping of electrons, respectively, and $k_3$ and $k_4$ the rate constants for recombination of conduction band electrons and trapped electrons, respectively. They found that the IMVS spectra are not influenced by diffusion in the electrolyte since no current flows through the system. Thus, only one peak is found in the IMVS spectra. This is given in Figure 2.13 where the imaginary part of the calculated IMVS transfer function is plotted against the frequency. The maximum peak is associated with the recombination process.

Each semicircle in any resulting IMVS spectra should reflect a distinct step in the electron-transfer kinetics assumed for the system. Thus, if one kinetic step is assumed, one semicircle is expected, if two steps are assumed, two semicircles are assumed, and so on. It is to be noted that the if the rate constants are similar in magnitude they may not be separated, but occurs at similar frequencies.

We expect an IMVS transfer function that is a complete or nearly complete semicircle, where the minimum of the calculated IMVS impedance plane plot is expected to be observed at a value equal to the effective rate constant $k = \tau^{-1}$.

## 2.7 Intensity-modulated photocurrent spectroscopy (IMPS)

Intensity-modulated photovoltage spectroscopy involves measuring a modulating photocurrent under sort-circuit conditions when illuminated with a modulating light intensity. The time-dependent

a) $\tau_1 \ll \tau_2$ and T > S

$\omega = 1/\tau_2$

$\omega = 1/\tau_1$

Im($\Delta V_{OC}$)

Re($\Delta V_{OC}$)

b) $\tau_1 \ll \tau_2$ and T < S

$\omega = 1/\tau_1$

$\omega = 1/\tau_2$

Im($\Delta V_{OC}$)

Re($\Delta V_{OC}$)

c) $\tau_1 < \tau_2$ and T < S

$\omega = 1/\tau_1$

$\omega = 1/\tau_2$

Im($\Delta V_{OC}$)

Re($\Delta V_{OC}$)
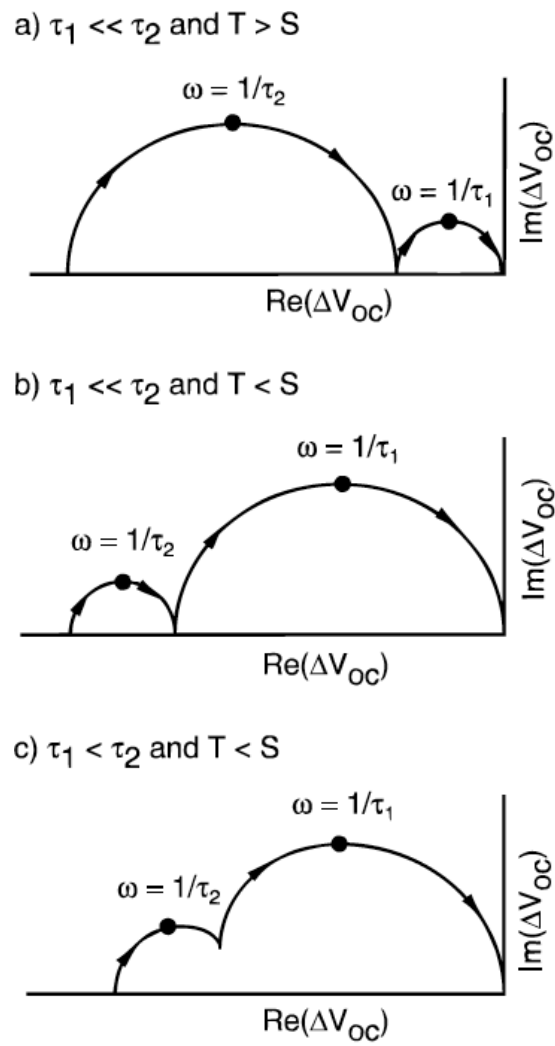
Figure 2.11: Schematic plot of the frequency response of potential modulation according to the reaction scheme in Figure 2.10. $\tau_1$ and $\tau_2$ are time constants, $\omega$ the angular frequency, and *S* and *T* depend on the rate constants. From [17].

Dye  $\xrightarrow{\ e^-\ }$  **TiO$_2$ Conductionband**

$k_1$    $k_2$

$k_3$

**TiO$_2$ Surface states**

$k_4$

**Redox Electrolyte**
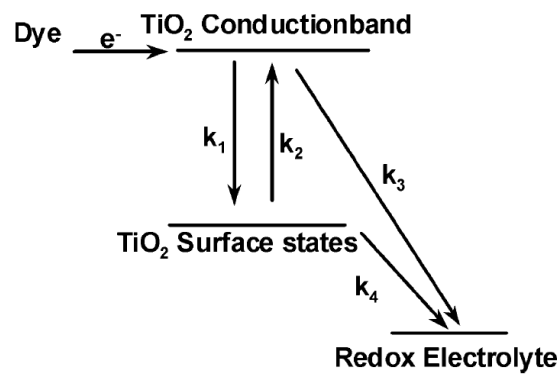
Figure 2.12: Reaction paths within a DSSC considered in [10].
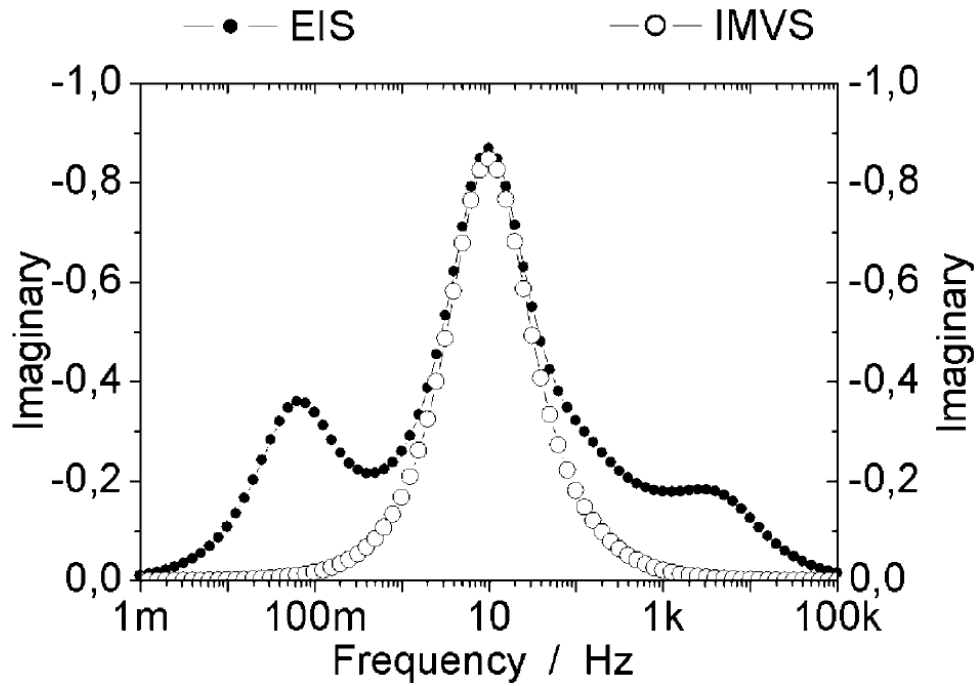
Figure 2.13: Imaginary part of the calculated IMVS spectrum, also plotted with the calculated EIS spectrum in [10]. The peak is associated with the recombination process. From [10].

incident illumination is assumed to be a sinusoidal perturbation on the form [18]

$$I(t) = I_0(1 + \delta\sin(\omega t)) \tag{2.9}$$

where $\delta$ is the depth of modulation and $I_0$ is the mean intensity. The intensity-modulated photocurrent spectroscopy (IMPS) is defined as the measurement of the complex ratio of photocurrent flux $i_{\text{photo}}(\omega)$ to incident light flux $I_0(\omega)$ [18, 19]

$$\frac{\mathscr{L}\{i_{\text{photo}}\}(\omega)}{\mathscr{L}\{I_0\}(\omega)} = \text{Re}\left(\frac{\mathscr{L}\{i_{\text{photo}}\}(\omega)}{\mathscr{L}\{I_0\}(\omega)}\right) + \text{Im}\left(\frac{\mathscr{L}\{i_{\text{photo}}\}(\omega)}{\mathscr{L}\{I_0\}(\omega)}\right) \tag{2.10}$$

If surface recombination occurs at an illuminated semiconductor electrode, the response to intensity-modulated illumination will be made up of two components associated first with the photogenerated minority carriers and second with the majority carriers that must flow to the surface in order to take part in surface recombination. The two currents have opposite signs, and generally they will not be in phase [19].

A set of different reaction routes of photogenerated minority holes for an n-type semiconductor may be assumed[19, 20], as shown in Figure 2.14. If the recombination is complete, i.e. $k_1 \gg k_0$, the response extends into the fourth quadrant of the complex plane, described in Figure 2.15a. The intercept at the origin in the upper quadrant is determined by the kinetics of surface recombination, whereas the response in the lower quadrant depends on the time constant $R_{\text{sol}}C_{\text{sc}}$, where $R_{\text{sol}}$ is the
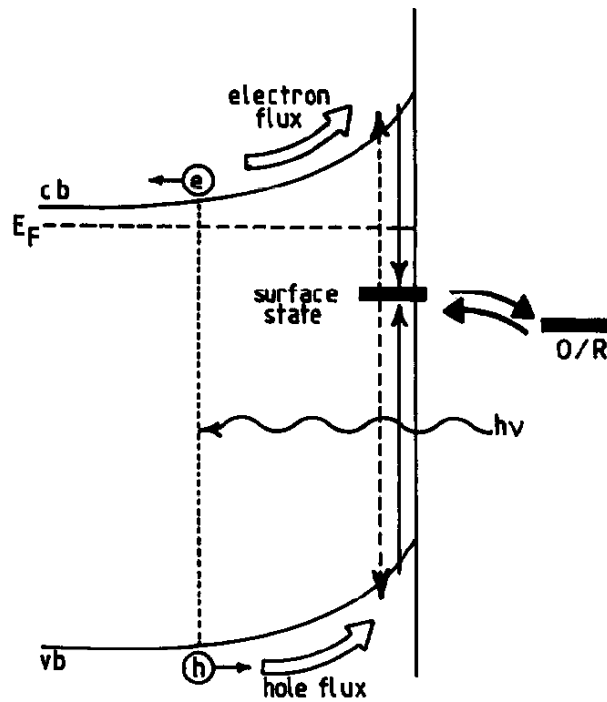
Figure 2.14: Simplified scheme illustrating the routes available for the reaction of photogenerated minority holes at the surface og an n-type semiconductor under depletion conditions. Note that a recombination via the set of surface states induces a flux of electrons into the surface. From [19].

solution resistance and $C_{\text{sc}}$ the space charge capacitance [19]. If the indirect charge transfer is negligible, the frequency of the maximum in the upper quadrant is related simply to the pseudo first rate constant for majority capture by the surface states. In a more general case where partial generation occurs is given in Figure 2.15b, where only half of the minority carriers are captured by surface states $k_1 = k_0$.

If the light intensity use for IMPS measurements is sufficiently low, the band bending, space-charge capacitance and density of majority carriers are not changed significantly from their values in dark. Provided that charge transfer, recombination and capture by surface states are linear processes, they can be described by first-order kinetic equations [20]. The general shape of the IMPS response is a semicircle arising from charge transfer/recombination and RC attenuation appear in the upper and lower quadrants of the complex plane, respectively. However, if the depletion layer capacitance is large and charge transfer is fast, the IMPS plots develop two semicircles in the lower complex plane [20].

A single time constant process would result in a semicircle in a complex plane plot of the quantum efficiency where the frequency at the apex of the semicircle can be related to the time constant of the process [21]. The observed depressed semicircle indicates a nonexponential or multi-time constant process consistent with the transient measurements. The continuity equation in the absence of

(a)                                                              (b)
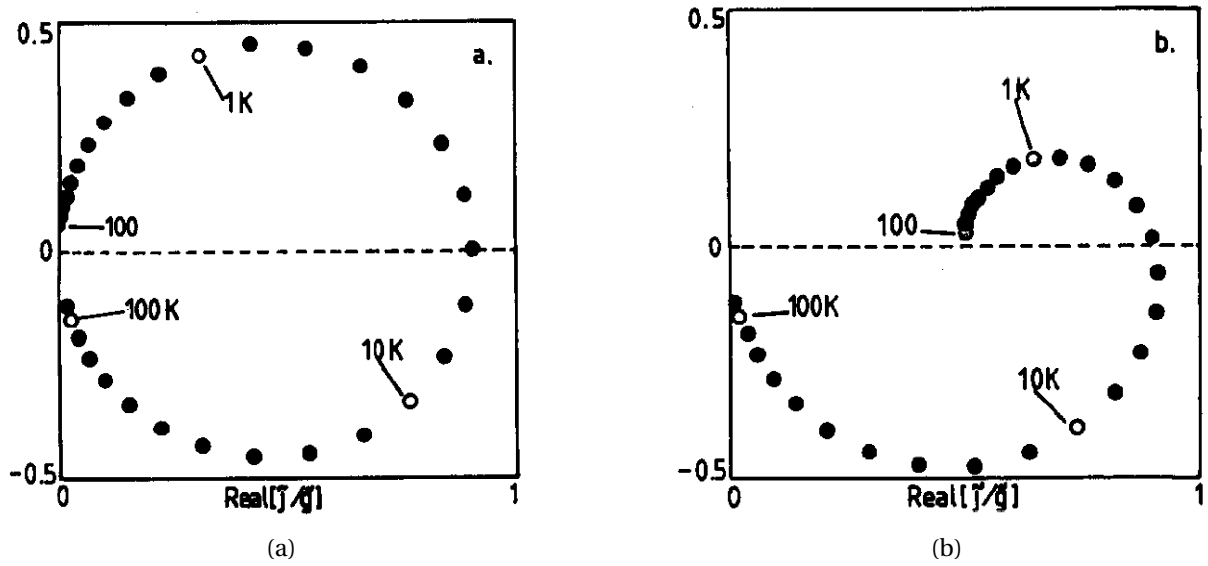
Figure 2.15: Theoretical IMPS plots calculated for a complete recombination ($k_1 \gg k_2$; $k_3 = 10^{-4}$ s$^{-1}$), and b partial recombination ($k_1 = k_2$). The low frequency interception at 0.5 corresponds to the steady-state photocurrent response. From [19].

electron migration is described by [21, 14, 15, 16, 10]

$$D\frac{\partial^2 n(x,t)}{\partial x^2} - \frac{\partial n(x,t)}{\partial t} - \frac{n(x,t) - n_0}{\tau_0} + I_0 \alpha e^{-\alpha x} = 0 \tag{2.11}$$

The solution of this equation predicts that the steady-state photocurrent is proportional to the light intensity. The solution gives a nonexponential rise and the characteristic rise time is independent of light intensity [21]. The recombination term described by the lifetime $\tau$ only modifies the rise time of the transients; it does not change the essential features of the solution. The diffusion coefficient $D$ represents the thermally activated transport of electrons through the particle network [21]. Physically, this model is consistent with an electron transport process controlled by thermal excitation from trap states in the particles [21]. Impedance plane plots for the work done by Cao et al. [21] is given in Figure 2.16, where $\beta = I_0 \alpha d^2 / n_0 D_0$.



(a)                                                              (b)
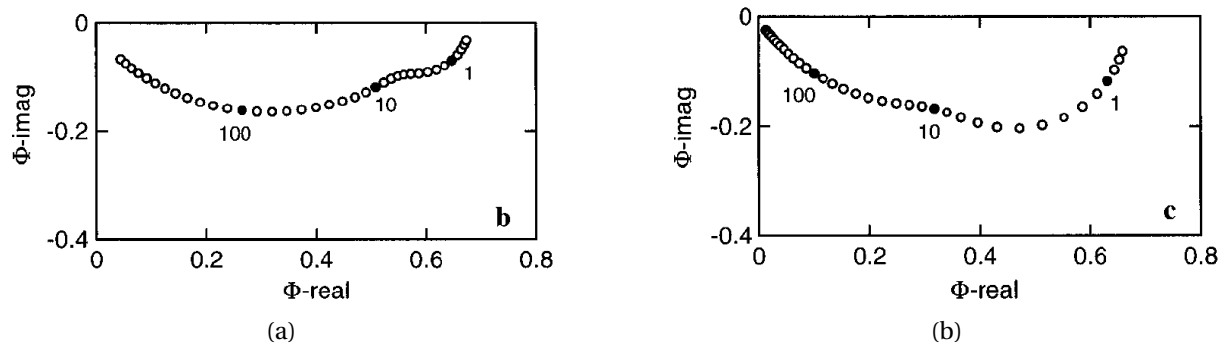
Figure 2.16: IMPS impedance plane plot for a $\alpha d = 10$ and $\beta = 1000$ and b $\alpha d = 3$ and $\beta = 300$. From [21].

The transport of photogenerated carriers through a porous network, consisting of nanometer sized particles, can be studied by IMPS [22]. The optoelectrical admittance is defined as $\Delta i(\omega)/eI_0(\omega)$, where and $\Delta i(\omega)$ is a harmonically varying photocurrent density and $I_0(\omega)$ i small amplitude harmonically component of the absorbed light intensity, respectively [22]. At sufficiently low frequencies, the optoelectrical admittance is real and corresponds to the photocurrent quantum yield $\Delta i/I_0$, and $\Delta i(\omega)/eI_0(\omega)$ becomes zero at sufficiently high frequencies [22]. For a sample of given thickness, it was found that $\omega_{min}$ increases strongly with the background light intensity $I_0$ as shown in Figure 2.17 [22]. The optoelectrical admittance corresponds to a semicircle in the [Re = positive, Im = negative] quadrant [22]. $\omega_{min}^{-1}$ is equal to the number of trapping events in the deepest unoccupied states times the lifetime of electron in this state before thermal release to the conduction band [22].



| (a) | (b) | (c) |
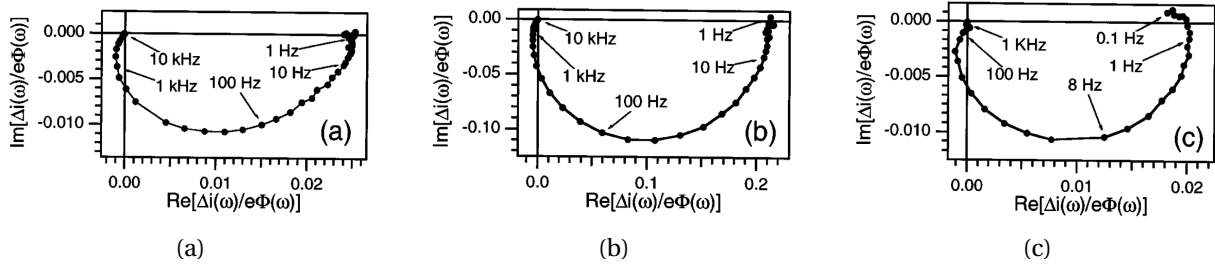
Figure 2.17: Complex plane representation of the optoelectrical admittance measured with the particulate $TiO_2$ electrodes of different thickness $d$, absorbed light intensity $\Phi$. a $d = 0.3$ $\mu$m, $\Phi = 1.2 \times 10^{16}$ cm$^{-2}$ s$^{-1}$, b $d = 0.9$ $\mu$m, $\Phi = 1.6 \times 10^{16}$ cm$^{-2}$ s$^{-1}$, and c $d = 4.0$ $\mu$m, $\Phi = 4.1 \times 10^{16}$ cm$^{-2}$ s$^{-1}$. From [22].

Due to slow transport through particulate electrodes, back transfer of electrons into the electrolyte can occur, which is believed to be one of the recombination mechanisms in $TiO_2$-based solar cells [23]. If the *RC* time of the porous electrode is shorter than the transient time of the photogenerated charge carriers through the porous network, the externally measured photocurrent response $\Delta i(\omega)$ corresponds to the internal photocurrent flow in the porous electrode which is due to the motion of charge carriers. In such a case, transit time of photogenerated charge carriers through the porous network can be obtained from IMPS studies [23]. The inverse of the frequency at which the imaginary component shows a minimum $\omega_{min}$ is a measure for the transit time of the photogenerated electrons. It was found that the transit time increases with increasing electrode thickness. The photocurrent quantum yield shows that photogenerated holes are consumed in two competing processes: hole transfer to the electrolyte and electron–hole recombination [23].

The electron transport in DSSCs must involve diffusion coupled to relaxation of the ionic atmosphere in the electrolyte phase [24]. The lifetime of excess electrons in the nanocrystalline solid is presumed to be determined by back reactions with the oxidized component of the sensitizer couple $(I^-/I_3^-)$. The IMPS plot for illumination from the electrolyte side crosses into the negative real quadrant and the positive imaginary quadrant before tending towards zero in the high frequency limit.

This behavior can be understood in terms of the diffusion-controlled transit time required for carriers generated outside the film to reach the substrate [24]. If the lifetime of electrons is sufficiently long, all photoinjected electrons are collected, and the dc value of $I_0$ is determined by the fraction of incident light absorbed [24]. For a finite electron lifetime, the dc photocurrent conversion efficiency depends on the ratio between the electron diffusion length $L = (D\tau)^{1/2}$ and the film thickness [24].

A convenient order of magnitude estimate of the diffusion coefficient can be obtained by noting that the minimum in the IMPS response occurs at an angular frequency corresponding to the inverse of the mean transit time for the electrons diffusing to the substrate [25]. The IMPS response can be described by an effective diffusion coefficient that determines $\tau_d$, where $\tau_d$ is the mean transit time for photogenerated electrons [25].

The diffusion of electrons to the substrate contact gives rise to a time delay between electron injection and collection. This delay is manifest as a phase lag in the photocurrent response to intensity-modulated light. IMPS measurements gives information about kinetics and transport [15]. If $\tau_n$ becomes large, it no longer influences the IMPS response. Under these conditions, $\omega_{\min}$ is directly proportional to $D_n$, with the coefficient of proportionality being determined by $\alpha$ and $d$ [15].

The time constant for charge collection $\tau_{cc}$ cannot be measured directly but is inferred from the relation between the open circuit time constant $\tau_{oc}$ and the time constant for the combined processes at short circuit $\tau_{sc}$ that is obtained from IMPS measurements (assuming linear and independent processes) [14]

$$\frac{1}{\tau_{sc}} = \frac{1}{\tau_{oc}} + \frac{1}{\tau_{cc}} \tag{2.12}$$

The IMPS response depends on how fast the steady-state carrier-concentration profile adjusts to a change of light intensity [14].

The apparent electron diffusion coefficient $D_n$ determined by IMPS is intensity-dependent [16]. It can be shown that the apparent diffusion coefficient for electrons is determined by the density of trapping states located at the electron quasi fermi level (QFL) [16]. If the first-order rate constants for trapping ($k_t$) and detrapping ($k_d$) are large compared with measurement frequency, the IMPS response is expected to have the same shape as in the absence of trapping [16]. The only change is that the frequency response is determined by the effective diffusion coefficient $D_n = D_{cb}(k_d/k_t)$, where $D_{cb}$ is the diffusion coefficient of electrons in the conduction band [16].

The phase shift between the modulated light component and the induced photocurrent is related to the transient time of electrons through the TiO$_2$ network [26]. At low frequencies the plots converge to a point in the real axis, which implies that low-frequency recombination does not occur under the used light conditions. The intercept corresponds to the IPCE [26].

As current is passing through the solar cel, IMPS measures a combined response from the photo

electrode, the counter electrode, and the electrolyte [27].

## 2.8  Equivalent circuit approach

One approach to derive impedance transfer functions is by the equivalent circuit approach. An equivalent circuit of the modeled system is assumed, where appropriate circuit elements are added either by looking at the electron flow processes throughout the system, or may be added randomly to fit experimental data. The latter is not recommended, as the physical understanding of the electrode system may be completely disregarded in order to fit the experimental data.

Bay et al. [27] establish a model of the dynamics of dye-sensitized solar cells by an equivalent circuit approach. Here, the porous electrode is modeled by a general branched transmission line model, in which a idealized porous photomodel network is assumed. The electronic coupling assumed between the electrode and the surrounding electrolyte is given in Figure 2.18. The upper and lower branches, $Z_e$ and $Z_i$ corresponds to the electronic and ionic transport, respectively. $Z_3$ corresponds to the impedance associated with charge transfer between the electrode and electrolyte. By using the charge balance for the electronic branches and the potential difference between the back contact and the electrode, the electrochemical impedance for the network $Z_{EC}$ and the transfer function accounting for photogeneration is obtained. By assuming open circuit voltage, an IMVS transfer
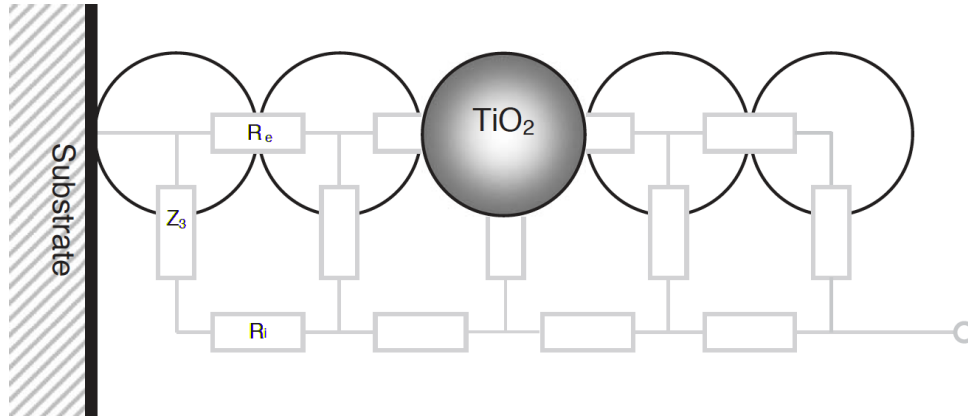


Figure 2.18: Transmission line model of the idealized porous photomodel network. $R_e$ is the resistivity of charge transport between electrode particles, $R_i$ is the resistivity of the electrolyte phase, and $Z_3$ is the impedance associated with transfer across the electrode–electrolyte interface. From Bay et al. [27].

function is obtained. From this IMVS transfer function, the diffusion coefficient is found to be given by $D_n = [C_s(R_i + R_e)]^{-1}$, where $C_s$ is the surface capacity. The electron lifetime in the conduction band is found to be given by $\tau_n = R_s C_s$ where $R_s$ is the reaction resistance for the recombination reaction. From previous results by e.g. Peter et al [15], they state that the diffusion length is given by $L_n = (D_n \tau_n)^{1/2} \sim (R_s/R_e)^{1/2}$. Further, they say that both the rate of recombination and number of free carriers in the electrode phase increases exponentially with decreasing potentials, and they ex-

pect thus the diffusion length is only weakly dependent of the potential of the photoelectrode. By assuming short circuit conditions, an IMPS transfer function is obtained by a similar approach.

## 2.9 Mathematical treatment by Laplace transform

In general, the mathematical treatment of impedance spectra by Laplace transform is rarely reported in the literature. The analytical expressions derived are thus difficult to compare to existing literature. However, the modeled impedance plane plots and bode plots may be compared to existing literature in order to compare and verify the derived models.

The relation between the system response and system properties are usually very complex in the time domain [8]. One method to greatly simplify the mathematical treatment of the system is to use Laplace transform from the time domain to the frequency domain. It can be shown that the impedance can be derived by setting $s = j\omega$ in the Laplace-transformed time region equations, where $j = \sqrt{-1}$. This proof is given in Appendix A, established by Professor Svein Sunde. Thus, the impedance in Eq. (2.1) can be expressed by the Laplace-transform of the voltage and the current by

$$Z(j\omega) = \frac{\mathscr{L}\{\tilde{r}\}(j\omega)}{\mathscr{L}\{\tilde{s}\}(j\omega)} \tag{2.13}$$

where $\tilde{r}$ and $\tilde{s}$ are the modulated frequency-dependent response and stimulus, respectively. This mathematical treatment of the impedance is used in this study.

The use of the Laplace transform approach to analyze the electrochemical impedance of nanostructured iridium oxide electrocatalysts is reported by Sunde et al. [28]. Sunde et al. [29] uses the Laplace transform approach to calculate the electrochemical impedance for porous intercalating electrodes. Peter [18] states that the response to be expected for a defined laser pulse shape in intensity modulated photocurrent spectroscopy may be obtained from the time-dependent solution of the diffusion problem using Laplace transform techniques. He introduces a interfacial transfer function $T_1(s)$ in terms of the rate constants

$$T_1(s) = \frac{\mathscr{L}\{j_{\text{photo}}\}(t)}{\mathscr{L}\{g\}(t)} = \frac{\tilde{j}_{\text{photo}}(s)}{\tilde{g}(s)} \tag{2.14}$$

where $j_{\text{photo}}(t)$ is the time-dependent photocurrent in the external circuit and $g(t)$ is the time-dependent excitation function (incident light profile). Macdonald et al. [8] states that the impedance of an electrochemical system may be described by Laplace transform. However, their focus is on the use of Fourier transform rather than Laplace transform, and is of little use for this thesis.

# 3 Modeling of electrochemical and photoelectrochemical impedance

## 3.1 Introduction

In this section the photoelectrochemical impedance transfer functions are derived. In Section 3.2 we introduce a numerical modeling approach to calculate photoelectrochemical impedance spectra using Newman's BAND(J) subroutine [30], studied in more detail in previous work [31]. In Section 3.3, the photoelectrochemical thin film electrode is described, and in Section 3.3.1 a physical description of a mixed conducting thin film electrode under steady-state conditions is introduced, assuming binary electrolyte and dilute solution theory. In Section 3.3.2 the steady-state physical description is extended to non-steady state conditions to calculate the frequency dependent impedance models. In section 3.3.3, the electrochemical faradaic impedance under zero illumination is derived, and in Section 3.3.4 the faradaic impedance under steady-state illumination is derived. A model for intensity-modulated photovoltage spectroscopy (IMVS) is derived in Section 3.3.5, and a model for intensity-modulated photocurrent spectroscopy (IMPS) is derived in Section 3.3.6. We introduce micropores to the thin film in Section 3.4 assuming a similar analogy as Södergren et. al [11], and an IMPS model for this system is derived in Section 3.4.2.

## 3.2 Numerical modeling of the impedance spectra with Newman's BAND(J) subroutine

The mathematical treatment of modeling impedance spectra involves solving partial differential equations, as described below. There are two approaches to solve these differential equations; analytical and numerical. Analytical modeling involves combining existing models, expressions and equations to solve a certain problem. This is preferred since a full control of the mathematical treatment is obtained, that is, at all times the assumed approximations are done physically. In this study, the focus is mainly on the analytical modeling approach. Numerical modeling involves approximating the mathematical problem with appropriate numerical methods. This is not preferred, as the assumptions made are purely mathematical, and not based on any physical aspects of the system. However, for complex systems analytical models are not obtainable, and numerical modeling is required.

Solving the partial differential equations involved in modeling of impedance spectra has been investigated in previous work [31]. The study used a subroutine BAND(J) for solving a set of $n$ coupled, linear, second-order differential equations numerically given by Newman [30]. The main goal of the study was to investigate if the subroutine could be applied to complex numbers, and proper convergence for the numerical approach was observed. However, several issues regarding the step size sensitivity of the convergence for the subroutine where observed. In this study, a small analysis of the convergence of this subroutine will be performed. It is noted that the numerical modeling is

not the focus of this study. For a more detailed description and study of the BAND(J) subroutine, see previous work [31].

## 3.3　Photoelectrochemical thin film electrode

The system to be modelled consists of a thin film electrode deposited on a planar substrate at $x = L$, sketched in Figure 3.1. The (planar) surface of the electrode faces the solution at $x = 0$. We assume that only the electrons may react with solution species, as normally only one of the bands are active in faradaic processes. The model can easily be reworked for hole transfer, so we do this without loss of generality.
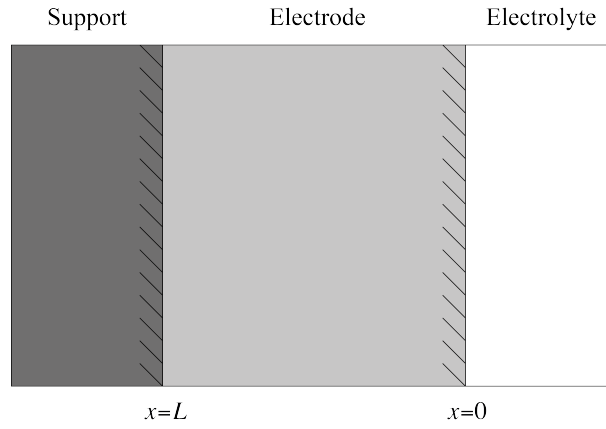


Figure 3.1: Schematics of the modeled thin film electrode system.

We assume the following species in the solid phase of the porous electrode: electrons of concentration $p$, holes of concentration $n$, acceptor dopants of concentration $N_a$, and donor dopants of concentration $N_d$. Assuming electroneutrality outside of space charge regions the following condition applies there [6]:

$$n - N_d - (p - N_a) = 0 \tag{3.1}$$

where the quantities are lumped so as to suggest a description in terms of the variables $c_+ = p - N_a$ and $c_- = n - N_d$. This gives the charge balance

$$z_+ \nu_+ c_+ + z_- \nu_- c_- = 0 \tag{3.2}$$

### 3.3.1　Physical description of mixed conducting thin film electrode

We employ the dilute-solution approximation in which the flux density vector of species $i$ in the film, $\boldsymbol{N}_i$, is described by [30]

$$\boldsymbol{N}_i = -z_i u_i F c_i \nabla \Phi_1 - D_i \nabla c_i \tag{3.3}$$

where $z_i$ is the charge number, $u_i$ the mobility, $c_i$ the concentration, and $D_i$ the diffusion coefficient of species $i$. Here we have neglected convection.

The material balance [30]

$$\frac{\partial c_i}{\partial t} = -\nabla \boldsymbol{N}_i + R_i \tag{3.4}$$

becomes, by combination of the expressions for $c_+$ and $c_-$ and Eq. (3.2) [30]

$$\frac{\partial c}{\partial t} = D\nabla^2 c + R_c \tag{3.5}$$

where

$$D = \frac{z_+ u_+ D_- - z_- u_- D_+}{z_+ u_+ - z_- u_-} \ , \ R_c = \frac{z_+ u_+ R_- - z_- u_- R_+}{z_+ u_+ - z_- u_-} \tag{3.6}$$

and the concentration of neutral hole-vacancy pair in the electrolyte phase $c$ is given by

$$c = \frac{c_+}{\nu_+} = \frac{c_-}{\nu_-} \tag{3.7}$$

$\nu_+$ and $\nu_-$ are the numbers of cations and anions produced by the dissociation of one molecule of electrolyte, respectively.

We assume first order kinetics for the charged species, and define the production per unit volumes $R_i$ in terms of the respective rate constants $R_i$ and charge carrier concentrations $c_i$ by

$$R_i = k_- c_- \tag{3.8}$$

With the definition of the concentration of neutral hole-vacancy pair in Eq. (3.7) we get the expression for $R_c$

$$R_c = \underbrace{\frac{z_+ u_+ \nu_- k_- - z_- u_- \nu_+}{z_+ u_+ - z_- u_-}}_{-k} c = -kc \tag{3.9}$$

where we have introduced a rate constant $k$ corresponding to recombination or trapping of charge carriers [32], rather than production of charge carriers, thus a negative sign is needed. $k$ includes all rate constants and any other pre-factors stemming from linearization of $R_+$ and $R_-$. We also introduce a source term due to photon absorption [11]

$$I_0 \alpha e^{-\alpha x} \tag{3.10}$$

where $I_0$ is the light intensity and $\alpha$ is the light adsorption coefficient.

Under steady-state conditions, the concentration is independent of the time, that is $\partial c/\partial t = 0$.

For a one-dimensional electrode system, the steady-state diffusion equation in Eq. (3.5) becomes

$$0 = D\frac{\partial^2 c_e}{\partial x^2} - kc_e + I_0\alpha e^{-\alpha x} \tag{3.11}$$

where "$e$" refers to steady-state.

The current in the electrolyte is given by [30]

$$\boldsymbol{i}_e = F\sum_i z_i N_i \tag{3.12}$$

and the net flux density is [30]

$$\sum_i N_i = \frac{\boldsymbol{i}_e}{F\sum_i z_i} \tag{3.13}$$

We see that $\boldsymbol{N}_i$ is the integrated form of Eq. (3.4). We get [30]

$$-\frac{\boldsymbol{i}_e}{z_+\nu_+F} = (z_+u_+ - z_-u_-)Fc\nabla\Phi_1 + (D_+ - D_-)\nabla c = N_+ \tag{3.14}$$

We assume that electronic species are blocked at the solution interface $x = 0$, in the present example the positive species, and we get the species fluxes [30]

$$N_{+x} = 0 = -z_+u_+F\nu_+c\frac{\partial\Phi}{\partial x} - D_+\nu_+\frac{\partial c}{\partial x} \tag{3.15}$$

$$N_{-x} = \frac{i_{x,e}}{z_-F} = -z_-u_-F\nu_-c\frac{\partial\Phi}{\partial x} - D_-\nu_-\frac{\partial c}{\partial x} \tag{3.16}$$

where $N_{ix}$ is the flux of species $i$ in x-direction. These fluxes are shown schematically in Figure 3.2 for a positive current $i_{x,e} > 0$. Positive charge carriers are blocked at the solution interface. Electrons are transferred from the electrode to the solution, that is in negative x-direction, since $N_{-x} < 0$ from Eq. (3.16) when we assume $z_- = -1$.

By elimination of the potential in Eq. (3.15) and (3.16), we get

$$\frac{i_{x,e}}{z_-\nu_-F} = \frac{z_-u_-D_+ - z_+u_+D_-}{z_+u_+}\frac{\partial c}{\partial x} \tag{3.17}$$

We introduce the transport number of the positive species [30]

$$t_+ = 1 - t_- = \frac{z_+u_+}{z_+u_+ - z_-u_-} \tag{3.18}$$

and the boundary condition at the electrolyte interface $x = 0$ becomes [30]

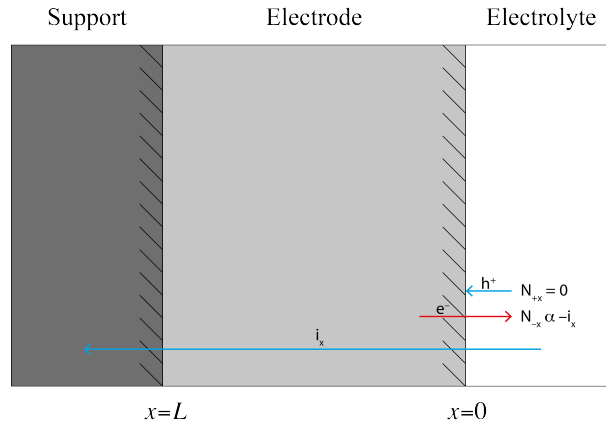$$\frac{i_{x,e}}{z_-\nu_-F} = -\frac{D}{1-t_-}\frac{\partial c}{\partial x}\bigg|_{x=0} \tag{3.19}$$

Figure 3.2: Schematics of the charge carrier fluxes across the solution interface ($x = 0$). Positive species are assumed to be blocked at the interface, $N_{+x} = 0$ (here represented by holes), and negative species flow from the electrode to the solution, $N_{-x} < 0$ (here represented by electrons).

At the substrate interface $x = L$, we assume that electrons are blocked in order to preserve charge balance and prevent charge accumulation, and get the species fluxes [30]

$$N_{+x} = \frac{i_{x,e}}{z_+ F} = -z_+ u_+ v_+ c \frac{\partial \Phi}{\partial x} - D_+ v_+ \frac{\partial c}{\partial x} \tag{3.20}$$

$$N_{-x} = 0 = -z_- u_- F v_- c \frac{\partial \Phi}{\partial x} - D_- v_- \frac{\partial c}{\partial x} \tag{3.21}$$

These fluxes are shown schematically in Figure 3.3 for a positive current $i_{x,e} > 0$. Negative charge carriers are blocked at the substrate interface. Holes are transferred from the electrode to the support, that is in positive $x$-direction, since $N_{-x} > 0$ from Eq. (3.20) when we assume $z_+ = 1$.
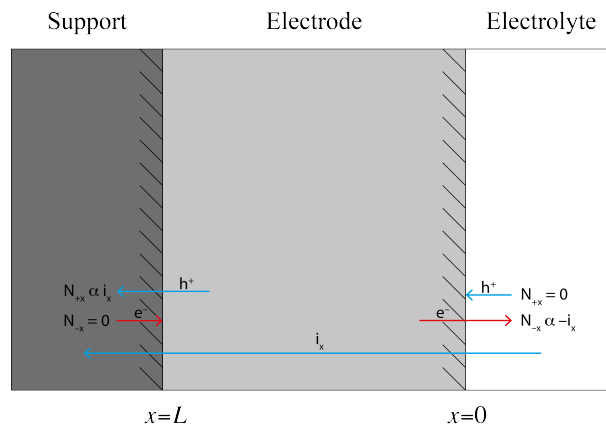


Figure 3.3: Schematics of the charge carrier fluxes across the substrate interface ($x = L$). Negative species are assumed to be blocked at the interface, $N_{-x} = 0$ (here represented by electrons), and positive species flow from the electrode to the support, $N_{-x} < 0$ (here represented by holes).

By eliminating the potential in Eq. (3.20) and (3.21), gives the boundary condition at $x = L$ [30]

$$\frac{i_{x,e}}{z_+ \nu_+ F} = -\frac{D}{1 - t_+}\frac{\partial c}{\partial x}\bigg|_{x=L} \tag{3.22}$$

The diffusion equation in Eq. (3.11) is solved with the boundary conditions in Eq. (3.19) and (3.22), which gives the specific solution of steady-state concentration profile

$$
\begin{aligned}
c_e(x) = {} & \frac{i_{x,e}}{F\sqrt{Dk}\sinh\left(\sqrt{\frac{k}{D}}L\right)} \\
& \cdot \left\{ K_{3,e}\cosh\left[\sqrt{\frac{k}{D}}(x - L)\right] - K_{4,e}\cosh\left(\sqrt{k}D\right)\right\} \\
& - \frac{I_0 \alpha e^{-\alpha x}}{D\alpha^2 - k}
\end{aligned}
\tag{3.23}
$$

with

$$K_{3,e} = \frac{1 - t_-}{z_- \nu_-} + \frac{FDI_0\alpha^2}{i_{f,e}(D\alpha^2 - k)} \tag{3.24}$$

$$K_{4,e} = \frac{1 - t_+}{z_+ \nu_+} + \frac{FDI_0\alpha^2 e^{-\alpha L}}{i_{f,e}(D\alpha^2 - k)} \tag{3.25}$$

This concentration profile is given in Figure 3.4 for $i_{x,e}, I_0 > 0$. We observe a positive gradient close to the solution interface $x = 0$ and a negative gradient close to the substrate interface $x = L$, as expected from the boundary conditions in Eq. (3.19) and (3.22), respectively.
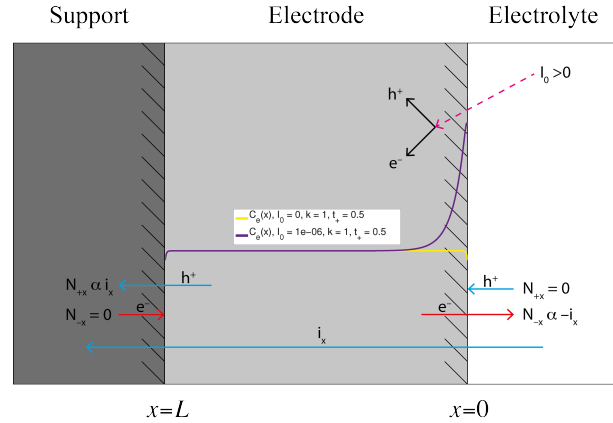


Figure 3.4: Calculated charge carrier concentration $c_e(x)$ across the electrode. A positive gradient close to the solution interface ($x = 0$) in accordance to Eq. (3.19) corresponds to the flux of negative species from electrode to solution from Eq. (3.16). A negative gradient close to the substrate interface $x = L$ in accordance to Eq. (3.22) corresponds to the flux of positive species from the electrode to the support from Eq. (3.20)

When we apply a positive light intensity change, we expect to observe an increase in the charge carrier concentration close to the interfaces, and a larger increase close to the solution interface ($x =$

0) where the illumination occurs than at the substrate interface ($x = L$). This is given in Figure 3.5, where $\Delta c_e(x)$ is the calculated change in steady-state concentration when applying a positive light intensity change ($\Delta I_0 > 0$). To prevent charge accumulation, we expect a net increase in the hole flux out of the electrode at the substrate interface ($x = L$), and a net increase in electron flux out of the electrode at solution interface ($x = 0$), described by $\Delta N_{ix}$ in Figure 3.5
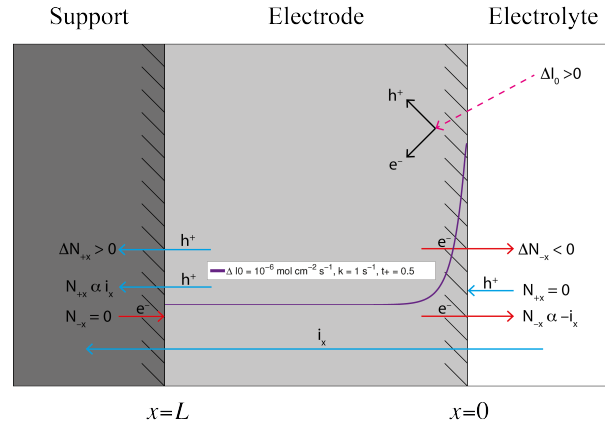


Figure 3.5: Calculated change in charge carrier concentration $\Delta c_e(x)$ when applying a positive light intensity change $\Delta I_0 > 0$. A net increase in concentration close to the interfaces is observed, where the increase is larger near the solution interface ($x = 0$). An increase in carrier concentration fluxes out of the interfaces is expected, and illustrated by $\Delta N_{ix}$.

The flux of negative carriers in the x-direction, $N_{-x}$, is related to the faradaic current as

$$i_{f,e} = -z_- F N_{-x} \tag{3.26}$$

since a vacancy flux in the direction from $x = 0$ to $x = L$ ($N_{-x} > 0$) represent oxidation of the oxide ($z_- = -1$ implies that $i_{f,e} = F N_{-x}$). Therefore $i_{f,e} = -i_{x,e}$, as shown schematically in Figure 3.6. The steady-state concentration profile in terms of the faradaic current becomes

$$c_e(x) = -\frac{i_{f,e}}{F\sqrt{Dk}\sinh\left(\sqrt{\frac{k}{D}}L\right)}$$
$$\cdot \left\{ K_{1,e}\cosh\left[\sqrt{\frac{k}{D}}(x-L)\right] - K_{2,e}\cosh\left(\sqrt{k}D\right) \right\}$$
$$- \frac{I_0 \alpha e^{-\alpha x}}{D\alpha^2 - k} \tag{3.27}$$

with

$$K_{1,e} = \frac{1-t_-}{z_- \nu_-} - \frac{FDI_0\alpha^2}{i_{f,e}(D\alpha^2 - k)} \tag{3.28}$$

$$K_{2,e} = \frac{1-t_+}{z_+ \nu_+} - \frac{FDI_0\alpha^2 e^{-\alpha L}}{i_{f,e}(D\alpha^2 - k)} \tag{3.29}$$

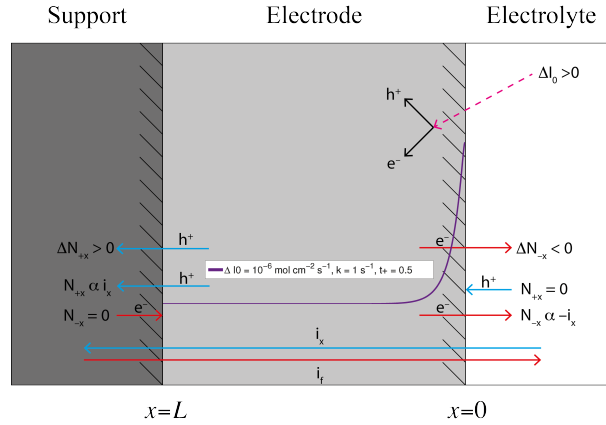Figure 3.6: Full schematic of the current flow in the modeled electrode system for $I_0, \Delta I_0, i_{x,e} > 0$. The faradaic current $i_{f,e}$ is defined in the opposite direction as the current $i_{x,e}$.

### 3.3.2    Solution of the nonsteady-state diffusion equation for mixed conducting thin film electrode

A harmonic perturbation is assumed applied in the driving force for current flow for $t > 0$. The concentration may be written

$$c = c(\boldsymbol{r},0) + \tilde{c}(\boldsymbol{r},t) \tag{3.30}$$

where $c(\boldsymbol{r},0)$ describes the steady-state concentration, and $\tilde{c}(\boldsymbol{r},t)$ describes the harmonic perturbation. The Laplace transform of the time derivative may be written as [33]

$$\mathscr{L}\left\{\frac{\partial c}{\partial t}\right\}(s) = s\,\mathscr{L}\{\tilde{c}\}(s) - \overbrace{\tilde{c}(0)}^{=0} = s\,\mathscr{L}\{\tilde{c}\}(s) \tag{3.31}$$

Combination of Eq. (3.31), (3.5), (3.9) and (3.10) gives, for a one-dimensional electrode system

$$s\,\mathscr{L}\{\tilde{c}\}(s) = D\frac{\partial^2\,\mathscr{L}\{\tilde{c}\}(s)}{\partial x^2} - k\,\mathscr{L}\{\tilde{c}\}(s) + \mathscr{L}\left\{\tilde{I}_0\right\}(s)\alpha e^{-\alpha x} \tag{3.32}$$

where the Laplace constant for impedance spectroscopy measurements is set to $s \to j\omega$, derived in Appendix A. We introduce the shortened nomenclature $\mathscr{L}\{\tilde{f}\}(s) = \mathscr{L}\{\tilde{f}\}$, for simplicity.

We assume that positive species are blocked at the solution interface $x = 0$ and negative species are blocked at the support interface $x = L$, as described above. The boundary conditions for the non-steady-state system is found by doing the Laplace transform of the steady-state boundary conditions in Eq. (3.19) and (3.22) [30], where we assume that $\mathscr{L}\{\tilde{i}_f\} = -\mathscr{L}\{\tilde{i}_x\}$

$$\frac{\mathscr{L}\left\{\tilde{i}_f\right\}}{z_-\nu_-F} = \frac{D}{1-t_-}\frac{\partial\,\mathscr{L}\{\tilde{c}\}}{\partial x}\bigg|_{x=0} \tag{3.33}$$

$$\frac{\mathscr{L}\{\tilde{i}_f\}}{z_+ \nu_+ F} = \frac{D}{1-t_+} \left.\frac{\partial \mathscr{L}\{\tilde{c}\}}{\partial x}\right|_{x=L} \tag{3.34}$$

Boundary conditions (3.33) and (3.34) are used to solve the diffusion equation (3.32), which give the specific solution

$$
\begin{aligned}
\mathscr{L}\{\tilde{c}\} = &-\frac{\mathscr{L}\{\tilde{i}_f\}}{F\sqrt{D(j\omega+k)}\sinh\left(\sqrt{\frac{j\omega+k}{D}}L\right)} \\
&\cdot\left\{ K_1(\omega)\cosh\left[\sqrt{\frac{j\omega+k}{D}}(x-L)\right]\right. \\
&\left.-K_2(\omega)\cosh\left(\sqrt{\frac{j\omega+k}{D}}x\right)\right\} \\
&-\frac{\mathscr{L}\{\tilde{I}_0\}\alpha}{D\alpha^2-k-j\omega}e^{-\alpha x}
\end{aligned}
\tag{3.35}
$$

where

$$K_1(\omega) = \frac{1-t_-}{z_- \nu_-} - \frac{FD\mathscr{L}\{\tilde{I}_0\}\alpha^2}{\mathscr{L}\{\tilde{i}_f\}(D\alpha^2-k-j\omega)} \tag{3.36}$$

$$K_2(\omega) = \frac{1-t_+}{z_+ \nu_+} - \frac{FD\mathscr{L}\{\tilde{I}_0\}\alpha^2}{\mathscr{L}\{\tilde{i}_f\}(D\alpha^2-k-j\omega)}e^{-\alpha L} \tag{3.37}$$

### 3.3.3   Electrochemical impedance of the thin film electrode (EIS)

For electrochemical impedance spectroscopy (EIS) measurements, we assume the conditions

$$
\begin{aligned}
\mathscr{L}\{\tilde{i}_f\} \neq 0; \quad &\mathscr{L}\{\tilde{V}\} \neq 0 \\
\mathscr{L}\{\tilde{I}_0\} = 0; \quad &I_0(x,0) = 0
\end{aligned}
\tag{3.38}
$$

The electrochemical (faradaic) impedance transfer function is given by [8]

$$Z_f(j\omega) = \frac{\mathscr{L}\{\tilde{V}\}}{\mathscr{L}\{\tilde{i}_f\}} \tag{3.39}$$

The faradaic current at the electrode-electrolyte interface, $i_f$, is assumed to be a function of the proton concentration in the oxide film and the potential difference between electrode and electrolyte, $\Phi_1 - \Phi_2$, given by the linearized expression

$$
\begin{aligned}
i_f &= \left(\frac{\partial i_f}{\partial c}\right)_{\Phi_1-\Phi_2,x=0} c(x=0) + \left[\frac{\partial i_f}{\partial(\Phi_1-\Phi_2)}\right]_{c,x=0}[\Phi_1(0)-\Phi_2(0)] \\
&= A_0 c(0) + B_0[\Phi_1(0)-\Phi_2(0)]
\end{aligned}
\tag{3.40}
$$

with $A_0 = \left(\frac{\partial i_f}{\partial c}\right)_{\Phi_1-\Phi_2,x=0}$ and $B_0 = \left[\frac{\partial i_f}{\partial(\Phi_1-\Phi_2)}\right]_{c,x=0}$.

The local admittance at the electrode-electrolyte interface for the combined faradaic reaction and

diffusion, $Y_0$, is found by combining Eq. (3.35) and the Laplace transformed Eq. (3.40) evaluated at $x = 0$

$$Y_0 = \frac{\mathscr{L}\{\tilde{i}_f\}}{\mathscr{L}\{\tilde{\Phi}_1(0) - \Phi_2(0)\}} = \frac{B_0}{1 - A_0 Z'_D} \tag{3.41}$$

with

$$Z'_D = -\frac{1}{F\sqrt{D(j\omega + k)}\sinh\left(\sqrt{\frac{j\omega+k}{D}}L\right)}$$
$$\cdot \left\{ \frac{1-t_-}{z_-\nu_-}\cosh\left(\sqrt{\frac{j\omega+k}{D}}L\right) - \frac{1-t_+}{z_+\nu_+}\right\} \tag{3.42}$$

By similar approach, the local admittance at the metal-oxide boundary, $Y_L$, is given by

$$Y_L = \frac{\mathscr{L}\{\tilde{i}_f\}}{\mathscr{L}\{\tilde{\Phi}_M(L) - \Phi_1(L)\}} = \frac{B_L}{1 - A_L Z'_D} \tag{3.43}$$

with

$$Z''_D = -\frac{1}{F\sqrt{D(j\omega + k)}\sinh\left(\sqrt{\frac{j\omega+k}{D}}L\right)}$$
$$\cdot \left\{ \frac{1-t_-}{z_-\nu_-} - \frac{1-t_+}{z_+\nu_+}\cosh\left(\sqrt{\frac{j\omega+k}{D}}L\right)\right\} \tag{3.44}$$

where $\tilde{\Phi}_M(L)$ is the potential of the metal support at $x = L$.

To relate the potential difference $\mathscr{L}\{\tilde{\Phi}_1(0) - \Phi_2(0)\}$ to the potential measured with respect to a reference electrode, we assume the equilibrium at the interface to the electrode support connecting the electrode

$$0 \rightleftharpoons \mathrm{h}^+ + \mathrm{e}^- \tag{3.45}$$

The electrochemical potential of electrons in the connecting leads is given through (in the dilute solution limit [30])

$$-\mu_e = \mu_h = \mu_h^0 + RT\ln c(L) + F\Phi_1(L) \tag{3.46}$$

when Eq. (3.45) is assumed to be in equilibrium. The measured potential is related to the electrochemical potential in a reference electrode as $\mu_e - \mu_e^{\mathrm{ref}} = -FV$.

We assume that $\mu_e^{\mathrm{ref}}$ can be measured by a reference electrode so that its value is representative of $\Phi_2(0)$ plus a constant. The amplitude and phase of the measured electrode potential is derived by taking the time dependent part of the linearized Eq. (3.46)

$$F\mathscr{L}\{\tilde{V}\} = \frac{RT}{c_e}\mathscr{L}\{\tilde{c}(L)\} + F\mathscr{L}\{\tilde{\Phi}_1(L)\} - F\mathscr{L}\{\Phi_2(0)\} \tag{3.47}$$

The potential $\Phi_1$ can in turn be related to the concentration $c$ and the faradaic current $i_f$ through [30]

$$\frac{i_f}{z_+ \nu_+ F} = (z_+ u_+ - z_- u_-)Fc\nabla\Phi + (D_+ - D_-)\nabla c \tag{3.48}$$

where we have used that $i_f = -i_x$ as described above. We assume that the potential gradient can be written $c\nabla\Phi_1 \approx c_e \frac{\partial\Phi_1}{\partial x} + c\frac{\partial\Phi_{1,e}}{\partial x}$, where we have neglected terms beyond first order. Eq. (3.48) becomes

$$\frac{i_f}{z_+ \nu_+ F} = (z_+ u_+ - z_- u_-)F\left(c_e\frac{\partial\Phi_1}{\partial x} + c\frac{\partial\Phi_{1,e}}{\partial x}\right) + (D_+ - D_-)\frac{\partial c}{\partial x} \tag{3.49}$$

We expect the steady-state concentration $c_e$ to be independent of the position [34]. For zero current, the relation [30]

$$F\frac{\partial\Phi_{1,e}}{\partial x} = -\frac{D_+ - D_-}{z_+ u_+ - z_- u_-}\frac{\partial\ln c_e}{\partial x} \tag{3.50}$$

implies that $\partial\Phi_{1,e}/\partial x = 0$. Using this result in the Laplace-transformed Eq. (3.49) and integrating from $x = 0$ to $x = L$ gives

$$\mathscr{L}\{\tilde{\Phi}_1(L)\} = \mathscr{L}\{\tilde{\Phi}_1(0)\} - \frac{D_+ - D_-}{Fc_e(z_+ u_+ - z_- u_-)}[\mathscr{L}\{\tilde{c}(L)\} - \mathscr{L}\{\tilde{c}(0)\} + \frac{\mathscr{L}\{\tilde{i}_f\}L}{\kappa} \tag{3.51}$$

with $\kappa = F^2\sum_i z_i^2 u_i c_i$ being the film conductivity. The phase and amplitude of the measured potential in Eq. (3.47) becomes

$$
\begin{aligned}
F\mathscr{L}\{\tilde{V}\} &= \frac{RT}{c_e}\mathscr{L}\{\tilde{c}(L)\} \\
&\quad + F\mathscr{L}\{\tilde{\Phi}_1(0)\} - \frac{D_+ - D_-}{c_e(z_+ u_+ - z_- u_-)}[\mathscr{L}\{\tilde{c}(L)\} - \mathscr{L}\{\tilde{c}(0)\}] - F\mathscr{L}\{\Phi_2(0)\} + \frac{F\mathscr{L}\{\tilde{i}_f\}L}{\kappa} \\
F\mathscr{L}\{\tilde{V}\} &= F\mathscr{L}\{\tilde{\Phi}_1(0) - F\Phi_2(0)\} \\
&\quad + \left[\frac{RT}{c_e} - \frac{D_+ - D_-}{c_e(z_+ u_+ - z_- u_-)}\right]\mathscr{L}\{\tilde{c}(L)\} + \frac{D_+ - D_-}{c_e(z_+ u_+ - z_- u_-)}\mathscr{L}\{\tilde{c}(0)\} + \frac{F\mathscr{L}\{\tilde{i}_f\}L}{\kappa} \\
F\mathscr{L}\{\tilde{V}\} &= F\mathscr{L}\{\tilde{\Phi}_1(0) - F\Phi_2(0)\} \\
&\quad + \left[\frac{(z_+ - 1)D_+ - (z_- - 1)D_-}{c_e(z_+ u_+ - z_- u_-)}\right]\mathscr{L}\{\tilde{c}(L)\} + \frac{D_+ - D_-}{c_e(z_+ u_+ - z_- u_-)}\mathscr{L}\{\tilde{c}(0)\} + \frac{F\mathscr{L}\{\tilde{i}_f\}L}{\kappa}
\end{aligned} \tag{3.52}
$$

where we have used the Nernst-Einstein relation $D_i = RTu_i$ [30]. Inserting the expressions for $\mathscr{L}\{\tilde{c}(0)\}$ and $\mathscr{L}\{\tilde{c}(L)\}$ described in Eq. (3.35), and that for the potential difference $F\mathscr{L}\{\tilde{\Phi}_1(0) - \Phi_2(0)\}$ implied by Eq. (3.41), the faradaic impedance for the electrode, $Z_f(j\omega)$, may be written

$$Z_f(j\omega) = \frac{\mathscr{L}\{\tilde{V}\}}{\mathscr{L}\{\tilde{i}_f\}} = Z_0 + Z_\phi + Z_\Omega \tag{3.53}$$

where $Z_0 = Y_0^{-1}$ from Eq. (3.41), $Z_\Omega = L/\kappa$ and

$$Z_\phi = \frac{D_+ - D_-}{Fc_e(z_+u_+ - z_-u_-)}Z_D' + \left[\frac{(z_+ - 1)D_+ - (z_- - 1)D_-}{Fc_e(z_+u_+ - z_-u_-)}\right]Z_D'' \tag{3.54}$$

### 3.3.4 Photoelectrochemical impedance of the thin film electrode (EIS)

For photoelectrochemical impedance spectroscopy (EIS) measurements, we apply a harmonically oscillating current under steady-state illumination and measure the potential response. That is

$$\mathcal{L}\{\tilde{i}_f\} \neq 0; \qquad i_{f,e} \neq 0; \quad \mathcal{L}\{\tilde{V}\} \neq 0$$
$$I_0(x,0) \neq 0; \quad \mathcal{L}\{\tilde{I}_0\} = 0 \tag{3.55}$$

The photoelectrochemical (faradaic) impedance transfer function is given by [8]

$$Z_f(j\omega) = \frac{\mathcal{L}\{\tilde{V}\}}{\mathcal{L}\{\tilde{i}_f\}} \tag{3.56}$$

Under these conditions the steady-state concentration $c_e$ cannot be assumed independent of the length as assumed in Section 3.3.3. In fact, the steady-state concentration $c_e(x)$ under illumination is given by Eq. (3.27). This is essentially the steady-state equivalent of Eq. (3.35), where the frequency is set to $\omega = 0$ and all time dependent quantities are replaced by steady-state ones,

$$c_e = -\frac{i_{f,e}}{F\sqrt{Dk}\sinh\left(\sqrt{\frac{k}{D}}L\right)}$$
$$\cdot \left\{K_{1,e}\cosh\left(\sqrt{\frac{k}{D}}(x-L)\right) - K_{2,e}\cosh\left(\sqrt{\frac{k}{D}}x\right)\right\} \tag{3.57}$$
$$-\frac{I_0\alpha}{D\alpha^2 - k}e^{-\alpha x}$$

with

$$K_{1,e} = \frac{1 - t_-}{z_-\nu_-} - \frac{FDI_0\alpha^2}{i_{f,e}(D\alpha^2 - k)}$$
$$K_{2,e} = \frac{1 - t_+}{z_+\nu_+} - \frac{FDI_0\alpha^2}{i_{f,e}(D\alpha^2 - k)}e^{-\alpha L} \tag{3.58}$$

The faradaic current at the electrode-electrolyte interface is again a function of the concentration and the potential difference by

$$i_f = \left(\frac{\partial i_f}{\partial c}\right)_{\Phi_1 - \Phi_2, x=0} c(x=0) + \left[\frac{\partial i_f}{\partial(\Phi_1 - \Phi_2)}\right]_{c, x=0} [\Phi_1(0) - \Phi_2(0)]$$
$$= A_0 c(0) - B_0[\Phi_1(0) - \Phi_2(0)] \tag{3.59}$$

with $A_0 = \left(\frac{\partial i_f}{\partial c}\right)_{\Phi_1 - \Phi_2, x=0}$ and $B_0 = \left[\frac{\partial i_f}{\partial(\Phi_1 - \Phi_2)}\right]_{c,x=0}$.

The local admittance at the electrode-electrolyte interface for the combined faradaic reaction and diffusion. $Y_0$, is found by combining Eq. (3.35) and the Laplace transformed Eq. (3.59) evaluated at $x = 0$

$$Y_0 = \frac{\mathcal{L}\{\tilde{i}_f\}}{\mathcal{L}\{\tilde{\Phi}_1(0) - \Phi_2(0)\}} = \frac{B_0}{1 - A_0 Z_D'} \tag{3.60}$$

with

$$Z_D' = -\frac{1}{F\sqrt{D(j\omega + k)}\sinh\left(\sqrt{\frac{j\omega+k}{D}}L\right)}$$
$$\cdot \left\{\frac{1-t_-}{z_- v_-}\cosh\left(\sqrt{\frac{j\omega+k}{D}}L\right) - \frac{1-t_+}{z_+ v_+}\right\} \tag{3.61}$$

By similar approach, the local admittance at the metal-oxide boundary, $Y_L$, is given by

$$Y_L = \frac{\mathcal{L}\{\tilde{i}_f\}}{\mathcal{L}\{\tilde{\Phi}_M(L) - \Phi_1(L)\}} = \frac{B_L}{1 - A_L Z_D'} \tag{3.62}$$

with

$$Z_D'' = -\frac{1}{F\sqrt{D(j\omega + k)}\sinh\left(\sqrt{\frac{j\omega+k}{D}}L\right)}$$
$$\cdot \left\{\frac{1-t_-}{z_- v_-} - \frac{1-t_+}{z_+ v_+}\cosh\left(\sqrt{\frac{j\omega+k}{D}}L\right)\right\} \tag{3.63}$$

where $\Phi_M(L)$ is the potential of the metal support at $x = L$. We also introduce a "diffusion impedance"-expression across the electrode, $Z_D(x)$, for simplicity in further derivation

$$Z_D(x) = -\frac{1}{F\sqrt{D(j\omega + k)}\sinh\left(\sqrt{\frac{j\omega+k}{D}}L\right)}$$
$$\cdot \left\{\frac{1-t_-}{z_- v_-}\cosh\left[\sqrt{\frac{j\omega+k}{D}}(x-L)\right] - \frac{1-t_+}{z_+ v_+}\cosh\left(\sqrt{\frac{j\omega+k}{D}}x\right)\right\} \tag{3.64}$$

The amplitude and phase of the measured electrode potential is derived by taking the time dependent part of the linearized Eq. (3.46)

$$F\mathcal{L}\{\tilde{V}\} = \frac{RT}{c_e(L)}\mathcal{L}\{\tilde{c}(L)\} + F\mathcal{L}\{\tilde{\Phi}_1(L)\} - F\mathcal{L}\{\Phi_2(0)\} \tag{3.65}$$

where $c_e(L)$ is the steady-state concentration in Eq. (3.57) evaluated at $x = L$.

The steady-state equivalent of Eq. (3.50) with no linearization is [30]

$$F\frac{\partial \Phi_{1,e}}{\partial x} = -\frac{D_+ - D_-}{z_+ u_+ - z_- u_-}\frac{\partial \ln c_e}{\partial x} + \frac{i_{f,e}}{z_+ v_+ F c_e(z_+ u_+ - z_- u_-)} \tag{3.66}$$

This gives the steady-state potential gradient $\partial \Phi_{1,e}/\partial x$ to be used in Eq. (3.49) and (3.51)

$$
\begin{aligned}
F\mathscr{L}\{\tilde{\Phi}_1(L)\} = {} & F\mathscr{L}\{\tilde{\Phi}_1(0)\} \\
& + \int_0^L \frac{\mathscr{L}\{\tilde{i}_f\}}{c_e z_+ \nu_+ F(z_+ u_+ - z_- u_-)} - F\frac{\mathscr{L}\{\tilde{c}\}}{c_e}\frac{\partial \Phi_{1,e}}{\partial x} - \frac{D_+ - D_-}{c_e(z_+ u_+ - z_- u_-)}\frac{\partial \mathscr{L}\{\tilde{c}\}}{\partial x} dx
\end{aligned}
\tag{3.67}
$$

or

$$
\begin{aligned}
F\mathscr{L}\{\tilde{\Phi}_1(L)\} = {} & F\mathscr{L}\{\tilde{\Phi}_1(0)\} \\
& + \int_0^L \frac{1}{c_e z_+ \nu_+ F(z_+ u_+ - z_- u_-)}\left(i_f - i_{f,e}\frac{\mathscr{L}\{\tilde{c}\}}{c_e}\right) \\
& - \frac{D_+ - D_-}{c_e(z_+ u_+ - z_- u_-)}\left(\frac{\partial \mathscr{L}\{\tilde{c}\}}{\partial x} - \frac{\mathscr{L}\{\tilde{c}\}}{c_e}\frac{\partial c_e}{\partial x}\right) dx
\end{aligned}
\tag{3.68}
$$

The phase and amplitude of the measured electrode potential is thus described by

$$
\begin{aligned}
F\mathscr{L}\{\tilde{V}\} = {} & \frac{RT}{c_e(L)}\mathscr{L}\{\tilde{c}(L)\} + F\mathscr{L}\{\tilde{\Phi}_1(0) - \Phi_2(0)\} \\
& + \int_0^L \frac{1}{c_e z_+ \nu_+ F(z_+ u_+ - z_- u_-)}\left(i_f - i_{f,e}\frac{\mathscr{L}\{\tilde{c}\}}{c_e}\right) \\
& - \frac{D_+ - D_-}{c_e(z_+ u_+ - z_- u_-)}\left(\frac{\partial \mathscr{L}\{\tilde{c}\}}{\partial x} - \frac{\mathscr{L}\{\tilde{c}\}}{c_e}\frac{\partial c_e}{\partial x}\right) dx
\end{aligned}
\tag{3.69}
$$

Again, we use the potential difference $F\mathscr{L}\{\tilde{\Phi}_1(0) - \Phi_2(0)\}$ implied by Eq. (3.60), as well as the expression for $\mathscr{L}\{\tilde{c}\}$ described in described in Eq. (3.35), and the faradaic photoelectrochemical impedance $Z_f(j\omega)$ may be written

$$
Z_f(j\omega) = \frac{\mathscr{L}\{\tilde{V}\}}{\mathscr{L}\{\tilde{i}_f\}} = Z_0 + Z_L + Z_\phi
\tag{3.70}
$$

where $Z_0 = Y_0^{-1}$, $Z_L = \frac{RT}{Fc_e(L)}Z_D''$ and

$$
\begin{aligned}
Z_\phi = {} & \int_0^L \frac{1}{c_e z_+ \nu_+ F^2(z_+ u_+ - z_- u_-)}\left(1 - i_{f,e}\frac{Z_D(x)}{c_e}\right) \\
& - \frac{D_+ - D_-}{c_e F(z_+ u_+ - z_- u_-)}\left(\frac{\partial Z_D(x)}{\partial x} - \frac{Z_D(x)}{c_e}\frac{\partial c_e}{\partial x}\right) dx
\end{aligned}
\tag{3.71}
$$

### 3.3.5   Intensity-modulated photovoltage spectroscopy of the thin film electrode (IMVS)

For intensity-modulated photovoltage spectroscopy (IMVS) measurements, we apply a harmonically perturbed light intensity and measure the voltage response under open circuit conditions. That is

$$
\begin{aligned}
& \mathscr{L}\{\tilde{i}_f\} = 0; \qquad i_{f,e} = 0; \quad \mathscr{L}\{\tilde{V}\} \neq 0 \\
& I_0(x,0) \neq 0; \quad \mathscr{L}\{\tilde{I}_0\} \neq 0
\end{aligned}
\tag{3.72}
$$

The IMVS transfer function is given by [10]

$$Z_V = \frac{\mathscr{L}\{\tilde{V}\}}{\mathscr{L}\{\tilde{I}_0\}} \tag{3.73}$$

Inserting the IMVS conditions from Eq. (3.72) in the expression for the harmonically oscillating concentration $\mathscr{L}\{\tilde{c}\}$ in Eq. (3.35) we get

$$\begin{aligned}
\mathscr{L}\{\tilde{c}\} = &-\frac{\mathscr{L}\{\tilde{I}_0\}}{F\sqrt{D(j\omega+k)}\sinh\left(\sqrt{\frac{j\omega+k}{D}}L\right)} \\
&\cdot \left\{ K_1(\omega)\cosh\left[\sqrt{\frac{j\omega+k}{D}}(x-L)\right] - K_2(\omega)\cosh\left(\sqrt{\frac{j\omega+k}{D}}\right) \right\} \\
&-\frac{\mathscr{L}\{\tilde{I}_0\}\alpha e^{-\alpha x}}{D\alpha^2 - k - j\omega}
\end{aligned} \tag{3.74}$$

with

$$K_1(\omega) = -\frac{FD\alpha^2}{D\alpha^2 - k - j\omega} \tag{3.75}$$

$$K_2(\omega) = -\frac{FD\alpha^2 e^{-\alpha L}}{D\alpha^2 - k - j\omega} \tag{3.76}$$

We introduce a "diffusion impedance" term for simplicity

$$\begin{aligned}
Z_{D,I_0} = \frac{\mathscr{L}\{\tilde{c}\}}{\mathscr{L}\{\tilde{I}_0\}} = &-\frac{1}{F\sqrt{D(j\omega+k)}\sinh\left(\sqrt{\frac{j\omega+k}{D}}L\right)} \\
&\cdot \left\{ K_1(\omega)\cosh\left[\sqrt{\frac{j\omega+k}{D}}(x-L)\right] - K_2(\omega)\cosh\left(\sqrt{\frac{j\omega+k}{D}}\right) \right\} \\
&-\frac{\alpha e^{-\alpha x}}{D\alpha^2 - k - j\omega}
\end{aligned} \tag{3.77}$$

Similarly, the steady-state concentration $c_e$ under IMVS conditions is given by combining Eq. (3.57) and (3.72)

$$\begin{aligned}
c_e = &-\frac{I_0}{F\sqrt{Dk}\sinh\left(\sqrt{\frac{k}{D}}L\right)} \\
&\cdot \left\{ K_{1,e}\cosh\left[\sqrt{\frac{k}{D}}(x-L)\right] - K_{2,e}\cosh\left(\sqrt{\frac{k}{D}}\right) \right\} \\
&-\frac{I_0\alpha e^{-\alpha x}}{D\alpha^2 - k - j\omega}
\end{aligned} \tag{3.78}$$

with

$$K_{1,e} = -\frac{FD\alpha^2}{D\alpha^2 - k} \tag{3.79}$$

$$K_{2,e} = -\frac{FD\alpha^2 e^{-\alpha L}}{D\alpha^2 - k} \tag{3.80}$$

The phase and amplitude of the voltage $\mathscr{L}\{\tilde{V}\}$ is given by combining Eq. (3.69) with the short circuit conditions from Eq (3.72) and the expressions for the harmonically oscillating concentration and steady-state concentration in Eq. (3.74) and (3.78), respectively

$$F\mathscr{L}\{\tilde{V}\} = \frac{RT}{c_e(L)} \mathscr{L}\{\tilde{c}\}(L) + F\mathscr{L}\{\tilde{\Phi}_1(0) - \Phi_2(0)\}$$
$$- \int_0^L \frac{D_+ - D_-}{c_e(z_+ u_+ - z_- u_-)} \left( \frac{\partial \mathscr{L}\{\tilde{c}\}}{\partial x} - \frac{\mathscr{L}\{\tilde{c}\}}{c_e} \frac{\partial c_e}{\partial x} \right) dx \tag{3.81}$$

where the potential difference $\mathscr{L}\{\tilde{\Phi}_1(0) - \Phi_2(0)\}$ is given by the linearized expression of the current in Eq. (3.40)

$$\mathscr{L}\{\tilde{i}_f\} = 0 = \left( \frac{\partial i_f}{\partial c} \right)_{\Phi_1 - \Phi_2} \mathscr{L}\{\tilde{c}\}(0) + \left[ \frac{\partial i_f}{\partial(\Phi_1 - \Phi_2)} \right]_{c,x=0} \mathscr{L}\{\tilde{\Phi}_1(0) - \Phi_2(0)\}$$

$$\mathscr{L}\{\tilde{\Phi}_1(0) - \Phi_2(0)\} = -\frac{A_0}{B_0} \mathscr{L}\{\tilde{c}\}(0) \tag{3.82}$$

By combination of Eq. (3.74) to (3.82) we get

$$F\mathscr{L}\{\tilde{V}\} = \mathscr{L}\{\tilde{I}_0\} \left[ \frac{RT}{c_e(L)} Z_{D,I_0}(x = L) + F\left( \frac{A_0}{B_0} Z_{D,I_0}(x = 0) \right) \right.$$
$$\left. - \int_0^L \frac{D_+ - D_-}{c_e(z_+ u_+ - z_- u_-)} \left( \frac{\partial Z_{D,I_0}}{\partial x} - \frac{Z_{D,I_0}}{c_e(x)} \frac{\partial c_e}{\partial x} \right) dx \right] \tag{3.83}$$

The IMVS transfer function becomes

$$Z_V = \frac{\mathscr{L}\{\tilde{V}\}}{\mathscr{L}\{\tilde{I}_0\}} = \frac{RT}{c_e(L)} Z_{D,I_0}(x = L) + F\left( \frac{A_0}{B_0} Z_{D,I_0}(x = 0) \right)$$
$$- \int_0^L \frac{D_+ - D_-}{c_e(z_+ u_+ - z_- u_-)} \left( \frac{\partial Z_{D,I_0}}{\partial x} - \frac{Z_{D,I_0}}{c_e(x)} \frac{\partial c_e}{\partial x} \right) dx \tag{3.84}$$

### 3.3.6   Intensity modulated photocurrent spectroscopy (IMPS)

For intensity-modulated photocurrent spectroscopy (IMPS) measurements, we apply a harmonically perturbed light intensity and measure the current response under short circuit conditions. That is

$$\mathscr{L}\{\tilde{i}_f\} \neq 0; \qquad i_{f,e} \neq 0; \quad \mathscr{L}\{\tilde{V}\} = 0$$
$$I_0(x,0) \neq 0; \quad \mathscr{L}\{\tilde{I}_0\} \neq 0 \tag{3.85}$$

The IMPS transfer function is given by [18]

$$Z_\phi(j\omega) = \frac{\mathcal{L}\{\tilde{i}_f\}}{\mathcal{L}\{\tilde{I}_0\}} \tag{3.86}$$

The harmonically oscillating concentration is given by inserting the IMPS conditions from Eq. (3.85) in the expression for $\mathcal{L}\{\tilde{c}\}$ in Eq. (3.35)

$$
\begin{aligned}
\mathcal{L}\{\tilde{c}\} = &-\frac{\mathcal{L}\{\tilde{i}_f\}}{F\sqrt{D(j\omega+k)}\sinh\left(\sqrt{\frac{j\omega+k}{D}}L\right)} \\
&\cdot \left\{ K_1(\omega)\cosh\left[\sqrt{\frac{j\omega+k}{D}}(x-L)\right] \right. \\
&\left. -K_2(\omega)\cosh\left(\sqrt{\frac{j\omega+k}{D}}x\right) \right\} \\
&-\frac{\mathcal{L}\{\tilde{I}_0\}\alpha}{D\alpha^2-k-j\omega}e^{-\alpha x}
\end{aligned}
\tag{3.87}
$$

with

$$
\begin{aligned}
K_1(\omega) &= \frac{1-t_-}{z_-v_-} - \frac{FD\mathcal{L}\{\tilde{I}_0\}\alpha^2}{\mathcal{L}\{\tilde{i}_f\}(D\alpha^2-k-j\omega)} \\
K_2(\omega) &= \frac{1-t_+}{z_+v_+} - \frac{FD\mathcal{L}\{\tilde{I}_0\}\alpha^2}{\mathcal{L}\{\tilde{i}_f\}(D\alpha^2-k-j\omega)}e^{-\alpha L}
\end{aligned}
\tag{3.88}
$$

The steady-state concentration $c_e$ under IMPS conditions is given by combining Eq. (3.57) and (3.85)

$$
\begin{aligned}
c_e = &-\frac{i_{f,e}}{F\sqrt{Dk}\sinh\left(\sqrt{\frac{k}{D}}L\right)} \\
&\cdot \left\{ K_{1,e}\cosh\left(\sqrt{\frac{k}{D}}(x-L)\right) - K_{2,e}\cosh\left(\sqrt{\frac{k}{D}}x\right) \right\} - \frac{I_0\alpha}{D\alpha^2-k}e^{-\alpha x}
\end{aligned}
\tag{3.89}
$$

with

$$
\begin{aligned}
K_{1,e} &= \frac{1-t_-}{z_-v_-} - \frac{FDI_0\alpha^2}{i_{f,e}(D\alpha^2-k)} \\
K_{2,e} &= \frac{1-t_+}{z_+v_+} - \frac{FDI_0\alpha^2}{i_{f,e}(D\alpha^2-k)}e^{-\alpha L}
\end{aligned}
\tag{3.90}
$$

In order to calculate the IMPS transfer function in Eq. (3.86), we want to express the harmonically oscillating faradaic current $\mathcal{L}\{\tilde{i}_f\}$ as a function of the oscillating light intensity $\mathcal{L}\{\tilde{I}_0\}$. This is done by expressing the harmonically oscillating concentration $\mathcal{L}\{\tilde{c}\}$ as a sum of one term dependent on $\mathcal{L}\{\tilde{i}_f\}$ only, and one term dependent on $\mathcal{L}\{\tilde{I}_0\}$ only. That is

$$\mathcal{L}\{\tilde{c}\} = \mathcal{L}\{\tilde{c}_{i_f}\} + \mathcal{L}\{\tilde{c}_{I_0}\} \tag{3.91}$$

The $\mathscr{L}\{\tilde{c}_{i_f}\}$ term includes all $\mathscr{L}\{\tilde{i}_f\}$ dependent terms in Eq. (3.87)

$$
\begin{aligned}
\mathscr{L}\{\tilde{c}_{i_f}\} = &-\frac{\mathscr{L}\{\tilde{i}_f\}}{F\sqrt{D(j\omega + k)}\sinh\left(\sqrt{\frac{j\omega+k}{D}}L\right)} \\
&\cdot \left\{ G_1(\omega)\cosh\left[\sqrt{\frac{j\omega+k}{D}}(x-L)\right] \right. \\
&\left. - G_2(\omega)\cosh\left(\sqrt{\frac{j\omega+k}{D}}x\right) \right\}
\end{aligned}
\tag{3.92}
$$

where

$$
\begin{aligned}
G_1(\omega) &= \frac{1-t_-}{z_- \nu_-} \\
G_2(\omega) &= \frac{1-t_+}{z_+ \nu_+}
\end{aligned}
\tag{3.93}
$$

For simplicity in the rest of the derivation, we introduce the "duffusion impedance"-term $Z_{D,i_f}(\omega,x)$, and write $\mathscr{L}\{\tilde{c}_{i_f}\}$ as

$$
\mathscr{L}\{\tilde{c}_{i_f}\} = \mathscr{L}\{\tilde{i}_f\}\cdot Z_{D,i_f}(\omega,x)
\tag{3.94}
$$

where

$$
\begin{aligned}
Z_{D,i_f}(\omega,x) = &-\frac{1}{F\sqrt{D(j\omega+k)}\sinh\left(\sqrt{\frac{j\omega+k}{D}}L\right)} \\
&\cdot \left\{ G_1(\omega)\cosh\left[\sqrt{\frac{j\omega+k}{D}}(x-L)\right] \right. \\
&\left. - G_2(\omega)\cosh\left(\sqrt{\frac{j\omega+k}{D}}x\right) \right\}
\end{aligned}
\tag{3.95}
$$

The $\mathscr{L}\{\tilde{c}_{I_0}\}$ term includes all $\mathscr{L}\{\tilde{I}_0\}$ dependent terms in Eq. (3.87)

$$
\begin{aligned}
\mathscr{L}\{\tilde{c}_{I_0}\} = &-\frac{1}{F\sqrt{D(j\omega+k)}\sinh\left(\sqrt{\frac{j\omega+k}{D}}L\right)} \\
&\cdot \left\{ G_3(\omega)\cosh\left[\sqrt{\frac{j\omega+k}{D}}(x-L)\right] \right. \\
&\left. - G_4(\omega)\cosh\left(\sqrt{\frac{j\omega+k}{D}}x\right) \right\} \\
&-\frac{\mathscr{L}\{\tilde{I}_0\}\alpha}{D\alpha^2 - k - j\omega}e^{-\alpha x}
\end{aligned}
\tag{3.96}
$$

where

$$G_3(\omega) = -\frac{FD\,\mathscr{L}\{\tilde{I}_0\}\alpha^2}{D\alpha^2 - k - j\omega}$$

$$G_4(\omega) = -\frac{FD\,\mathscr{L}\{\tilde{I}_0\}\alpha^2}{D\alpha^2 - k - j\omega}e^{-\alpha L} \tag{3.97}$$

Again, for simplicity, we introduce the "diffusion impedance"-term $Z_{D,I_0}(\omega,k)$, and write $\mathscr{L}\{\tilde{c}_{I_0}\}$ as

$$\mathscr{L}\{\tilde{c}_{I_0}\} = \mathscr{L}\{\tilde{I}_0\} \cdot Z_{D,I_0}(\omega,x) \tag{3.98}$$

where

$$
\begin{aligned}
Z_{D,I_0}(\omega,x) = &-\frac{1}{F\sqrt{D(j\omega+k)}\sinh\left(\sqrt{\frac{j\omega+k}{D}}L\right)} \\
&\cdot\left\{-\frac{FD\alpha^2}{D\alpha^2-k-j\omega}\cosh\left[\sqrt{\frac{j\omega+k}{D}}(x-L)\right]\right. \\
&\left.+\frac{FD\alpha^2}{D\alpha^2-k-j\omega}e^{-\alpha L}\cosh\left(\sqrt{\frac{j\omega+k}{D}}x\right)\right\} \\
&-\frac{\alpha}{D\alpha^2-k-j\omega}e^{-\alpha x}
\end{aligned}
\tag{3.99}
$$

It may be shown that the harmonically concentration $\mathscr{L}\{\tilde{c}\}$ is expressed by the sum of the two terms in Eq. (3.94) and (3.98).

The potential difference $\mathscr{L}\{\tilde{\Phi}_1(0)-\Phi_2(0)\}$ is given by combining the linearized expression of $\mathscr{L}\{\tilde{i}_f\}$ in Eq. (3.40) with Eq. (3.91)

$$\mathscr{L}\{\tilde{\Phi}_1(0)-\Phi_2(0)\} = \mathscr{L}\{\tilde{i}_f\}\frac{1}{B_0} - \frac{A_0}{B_0}\left[\mathscr{L}\{\tilde{c}_{i_f}\}(0)+\mathscr{L}\{\tilde{c}_{I_0}\}(0)\right] \tag{3.100}$$

We insert $\mathscr{L}\{\tilde{V}\}=0$ in the expression for the measured phase and amplitude of the potential given in Eq. (3.69). Our goal is to find an expression for $\mathscr{L}\{\tilde{i}_f\}$ as a function of $\mathscr{L}\{\tilde{I}_0\}$ with the expression for $\mathscr{L}\{\tilde{c}\}$ derived above

$$
\begin{aligned}
0 = &\frac{RT}{c_e(L)}\mathscr{L}\{\tilde{c}\}(L) + F\,\mathscr{L}\{\tilde{\Phi}_1(0)-\Phi_2(0)\} \\
&+\int_0^L \frac{1}{c_e z_+ \nu_+ F(z_+ u_+ - z_- u_-)}\left(\mathscr{L}\{\tilde{i}_f\} - i_e\frac{\mathscr{L}\{\tilde{c}\}}{c_e}\right) \\
&-\frac{D_+ - D_-}{c_e(z_+ u_+ - z_- u_-)}\left(\frac{\partial\mathscr{L}\{\tilde{c}\}}{\partial x} - \frac{\mathscr{L}\{\tilde{c}\}}{c_e}\frac{\partial c_e}{\partial x}\right)dx
\end{aligned}
\tag{3.101}
$$

Combination of Eq. (3.91), (3.100) and (3.101) gives

$$
\begin{aligned}
0 = &\frac{RT}{c_e(L)}\left[\mathscr{L}\{\tilde{c}_{i_f}\}(L)+\mathscr{L}\{\tilde{c}_{I_0}\}(L)\right] + F\left(\mathscr{L}\{\tilde{i}_f\}\frac{1}{B_0} - \frac{A_0}{B_0}\left[\mathscr{L}\{\tilde{c}_{i_f}\}(0)+\mathscr{L}\{\tilde{c}_{I_0}\}(0)\right]\right) \\
&+\int_0^L \frac{1}{c_e z_+ \nu_+ F(z_+ u_+ - z_- u_-)}\left(\mathscr{L}\{\tilde{i}_f\} - \frac{i_e}{c_e}\left[\mathscr{L}\{\tilde{c}_{i_f}\}+\mathscr{L}\{\tilde{c}_{I_0}\}\right]\right) \\
&-\frac{D_+ - D_-}{c_e(z_+ u_+ - z_- u_-)}\left(\left[\frac{\partial\mathscr{L}\{\tilde{c}_{i_f}\}}{\partial x}+\frac{\partial\mathscr{L}\{\tilde{c}_{I_0}\}}{\partial x}\right] - \left[\mathscr{L}\{\tilde{c}_{i_f}\}+\mathscr{L}\{\tilde{c}_{I_0}\}\right]\frac{1}{c_e}\frac{\partial c_e}{\partial x}\right)dx
\end{aligned}
\tag{3.102}
$$

We set all the $\mathscr{L}\{\tilde{i}_f\}$ and $\mathscr{L}\{\tilde{c}_{i_f}\}$ terms on the left hand side of the equation, and all $\mathscr{L}\{\tilde{I}_0\}$ and $\mathscr{L}\{\tilde{c}_{I_0}\}$ terms on the right hand side of the expression. Combination with Eq. (3.94) and (3.98) we get

$$
\begin{aligned}
\mathscr{L}\{\tilde{i}_f\} &\left\{ \frac{RT}{c_e(L)} Z_{D,i_f}(\omega,L) + F\left(\frac{1}{B_0} - \frac{A_0}{B_0} Z_{D,i_f}(\omega,0)\right) \right. \\
&+ \int_0^L \frac{1}{c_e z_+ \nu_+ F(z_+ u_+ - z_- u_-)} \left(1 - \frac{i_e}{c_e} Z_{D,i_f}(\omega,x)\right) \\
&\left. - \frac{D_+ - D_-}{c_e(z_+ u_+ - z_- u_-)} \left(\frac{\partial Z_{D,i_f}(\omega,x)}{\partial x} - \frac{Z_{D,i_f}(\omega,x)}{c_e} \frac{\partial c_e}{\partial x}\right) dx \right\} \\
= \mathscr{L}\{\tilde{I}_0\} &\left\{ -\frac{RT}{c_e(L)} Z_{D,I_0}(\omega,L) + \frac{FA_0}{B_0} Z_{D,I_0}(\omega,0) \right. \\
&+ \int_0^L \frac{1}{c_e z_+ \nu_+ F(z_+ u_+ - z_- u_-)} \left(\frac{i_e}{c_e} Z_{D,I_0}(\omega,x)\right) \\
&\left. + \frac{D_+ - D_-}{c_e(z_+ u_+ - z_- u_-)} \left(\frac{\partial Z_{D,I_0}(\omega,x)}{\partial x} - \frac{Z_{D,I_0}(\omega,x)}{c_e} \frac{\partial c_e}{\partial x}\right) dx \right\}
\end{aligned}
\tag{3.103}
$$

The harmonically oscillating faradaic current is thus given by

$$
\begin{aligned}
\mathscr{L}\{\tilde{i}_f\} = \mathscr{L}\{\tilde{I}_0\} &\left\{ -\frac{RT}{c_e(L)} Z_{D,I_0}(\omega,L) + \frac{FA_0}{B_0} Z_{D,I_0}(\omega,0) \right. \\
&+ \int_0^L \frac{1}{c_e z_+ \nu_+ F(z_+ u_+ - z_- u_-)} \left(\frac{i_e}{c_e} Z_{D,I_0}(\omega,x)\right) \\
&\left. + \frac{D_+ - D_-}{c_e(z_+ u_+ - z_- u_-)} \left(\frac{\partial Z_{D,I_0}(\omega,x)}{\partial x} - \frac{Z_{D,I_0}(\omega,x)}{c_e} \frac{\partial c_e}{\partial x}\right) dx \right\} \Bigg/ \\
&\left\{ \frac{RT}{c_e(L)} Z_{D,i_f}(\omega,L) + F\left(\frac{1}{B_0} - \frac{A_0}{B_0} Z_{D,i_f}(\omega,0)\right) \right. \\
&+ \int_0^L \frac{1}{c_e z_+ \nu_+ F(z_+ u_+ - z_- u_-)} \left(1 - \frac{i_e}{c_e} Z_{D,i_f}(\omega,x)\right) \\
&\left. - \frac{D_+ - D_-}{c_e(z_+ u_+ - z_- u_-)} \left(\frac{\partial Z_{D,i_f}(\omega,x)}{\partial x} - \frac{Z_{D,i_f}(\omega,x)}{c_e} \frac{\partial c_e}{\partial x}\right) dx \right\}
\end{aligned}
\tag{3.104}
$$

The IMPS transfer function in Eq. (3.86) becomes

$$
\begin{aligned}
Z_\phi(j\omega) = \frac{\mathscr{L}\{\tilde{i}_f\}}{\mathscr{L}\{\tilde{I}_0\}} = &\left\{ -\frac{RT}{c_e(L)} Z_{D,I_0}(\omega,L) + \frac{FA_0}{B_0} Z_{D,I_0}(\omega,0) \right. \\
&+ \int_0^L \frac{1}{c_e z_+ \nu_+ F(z_+ u_+ - z_- u_-)} \left(\frac{i_e}{c_e} Z_{D,I_0}(\omega,x)\right) \\
&\left. + \frac{D_+ - D_-}{c_e(z_+ u_+ - z_- u_-)} \left(\frac{\partial Z_{D,I_0}(\omega,x)}{\partial x} - \frac{Z_{D,I_0}(\omega,x)}{c_e} \frac{\partial c_e}{\partial x}\right) dx \right\} \Bigg/ \\
&\left\{ \frac{RT}{c_e(L)} Z_{D,i_f}(\omega,L) + F\left(\frac{1}{B_0} - \frac{A_0}{B_0} Z_{D,i_f}(\omega,0)\right) \right. \\
&+ \int_0^L \frac{1}{c_e z_+ \nu_+ F(z_+ u_+ - z_- u_-)} \left(1 - \frac{i_e}{c_e} Z_{D,i_f}(\omega,x)\right) \\
&\left. - \frac{D_+ - D_-}{c_e(z_+ u_+ - z_- u_-)} \left(\frac{\partial Z_{D,i_f}(\omega,x)}{\partial x} - \frac{Z_{D,i_f}(\omega,x)}{c_e} \frac{\partial c_e}{\partial x}\right) dx \right\}
\end{aligned}
\tag{3.105}
$$

To understand the physical interpretation of the detailed IMPS transfer function described by Eq. (3.105), one may assume a simpler case in which one of the transport numbers are approximately

equal to unity. For our speciation, as described in Section 4.2, we may assume the transport numbers $t_+ = 1$ and $t_- = 0$. The harmonically oscillating concentration is given by inserting these transport numbers into the expression for the harmonically oscillating concentration in Eq. (3.87)

$$
\begin{aligned}
\mathscr{L}\{\tilde{c}\} = & -\frac{\mathscr{L}\{\tilde{\imath}_f\}}{F\sqrt{D(j\omega+k)}\sinh\left(\sqrt{\frac{j\omega+k}{D}}L\right)} \\
& \cdot \left\{ K_3(\omega)\cosh\left[\sqrt{\frac{j\omega+k}{D}}(x-L)\right] \right. \\
& \left. -K_4(\omega)\cosh\left(\sqrt{\frac{j\omega+k}{D}}x\right)\right\} \\
& -\frac{\mathscr{L}\{\tilde{I}_0\}\alpha}{D\alpha^2-k-j\omega}e^{-\alpha x}
\end{aligned}
\tag{3.106}
$$

with

$$
\begin{aligned}
K_3(\omega) &= \frac{1}{z_-\nu_-} - \frac{FD\,\mathscr{L}\{\tilde{I}_0\}\alpha^2}{\mathscr{L}\{\tilde{\imath}_f\}(D\alpha^2-k-j\omega)} \\
K_4(\omega) &= -\frac{FD\,\mathscr{L}\{\tilde{I}_0\}\alpha^2}{\mathscr{L}\{\tilde{\imath}_f\}(D\alpha^2-k-j\omega)}e^{-\alpha L}
\end{aligned}
\tag{3.107}
$$

The steady-state concentration $c_e(x)$ under IMPS conditions is given by the steady-state equivalent of Eq. (3.106) by setting $\omega = 0$ and change all time dependent function to steady-state ones

$$
\begin{aligned}
c_e = & -\frac{i_{f,e}}{F\sqrt{Dk}\sinh\left(\sqrt{\frac{k}{D}}L\right)} \\
& \cdot\left\{ K_{1,e}\cosh\left(\sqrt{\frac{k}{D}}(x-L)\right) - K_{2,e}\cosh\left(\sqrt{\frac{k}{D}}x\right)\right\} - \frac{I_0\alpha}{D\alpha^2-k}e^{-\alpha x}
\end{aligned}
\tag{3.108}
$$

with

$$
\begin{aligned}
K_{3,e} &= \frac{1}{z_-\nu_-} - \frac{FDI_0\alpha^2}{i_{f,e}(D\alpha^2-k)} \\
K_{4,e} &= -\frac{FDI_0\alpha^2}{i_{f,e}(D\alpha^2-k)}e^{-\alpha L}
\end{aligned}
\tag{3.109}
$$

Again, we write the oscillating concentration profile on the form

$$
\mathscr{L}\{\tilde{c}\} = \mathscr{L}\{\tilde{c}_{i_f}\} + \mathscr{L}\{\tilde{c}_{I_0}\}
\tag{3.110}
$$

where we define

$$
\mathscr{L}\{\tilde{c}_{i_f}\} = \mathscr{L}\{\tilde{\imath}_f\}\cdot Z_{D,i_f}(\omega,x) \qquad \mathscr{L}\{\tilde{c}_{I_0}\} = \mathscr{L}\{\tilde{I}_0\}\cdot Z_{D,I_0}(\omega,x)
\tag{3.111}
$$

with

$$Z_{D,i_f}(\omega, x) = -\frac{\cosh\left[\sqrt{\frac{j\omega+k}{D}}(x-L)\right]}{z_- v_- F\sqrt{D(j\omega+k)}\sinh\left(\sqrt{\frac{j\omega+k}{D}}L\right)}$$ 

(3.112)

and

$$
\begin{aligned}
Z_{D,I_0}(\omega, x) = &-\frac{1}{F\sqrt{D(j\omega+k)}\sinh\left(\sqrt{\frac{j\omega+k}{D}}L\right)} \\
&\cdot\left\{-\frac{FD\alpha^2}{D\alpha^2-k-j\omega}\cosh\left[\sqrt{\frac{j\omega+k}{D}}(x-L)\right]\right. \\
&\left.+\frac{FD\alpha^2 e^{-\alpha L}}{D\alpha^2-k-j\omega}\cosh\left(\sqrt{\frac{j\omega+k}{D}}x\right)\right\} \\
&-\frac{\alpha e^{-\alpha x}}{D\alpha^2-k-j\omega}
\end{aligned}
$$

(3.113)

The IMPS transfer function of this simplified system is given by replacing $Z_{D,i_f}(\omega, x)$ and $Z_{D,I_0}(\omega, x)$ in Eq. (3.105) with the ones derived in Eq. (3.112) and (3.113), respectively.

Another simplification to understand the detailed transfer function in Eq. (3.86) is to assume an electrode in which the same species is blocked at both the electrolyte and support interfaces. We assume for this derivation that positive species are blocked at both electrode interfaces. At the electrolyte interface ($x = 0$) we get the species fluxes

$$N_{+x}|_{x=0} = 0 = -z_+ u_+ F v_+ c\frac{\partial\Phi}{\partial x} - D_+ v_+ \frac{\partial c}{\partial x}$$

(3.114)

$$N_{-x}|_{x=0} = -\frac{i_f}{z_- F} = -z_- u_- F v_- c\frac{\partial\Phi}{\partial x} - D_- v_- \frac{\partial c}{\partial x}$$

(3.115)

By eliminating the potential in Eq. (3.114) and (3.115) and doing the Laplace transform we get the boundary condition

$$\frac{\mathscr{L}\{\tilde{i}_f\}}{z_- v_- F} = \frac{D}{1-t_-}\frac{\partial\mathscr{L}\{\tilde{c}\}}{\partial x}\bigg|_{x=0}$$

(3.116)

At the support interface ($x = L$) we get equal species fluxes

$$N_{+x}|_{x=L} = 0 = -z_+ u_+ F v_+ c\frac{\partial\Phi}{\partial x} - D_+ v_+ \frac{\partial c}{\partial x}$$

(3.117)

$$N_{-x}|_{x=L} = -\frac{i_f}{z_- F} = -z_- u_- F v_- c\frac{\partial\Phi}{\partial x} - D_- v_- \frac{\partial c}{\partial x}$$

(3.118)

By eliminating the potential in Eq. (3.117) and (3.118) and doing the Laplace transform we get the boundary condition

$$\frac{\mathscr{L}\{\tilde{i}_f\}}{z_- v_- F} = \frac{D}{1-t_-}\frac{\partial\mathscr{L}\{\tilde{c}\}}{\partial x}\bigg|_{x=L}$$

(3.119)

We solve the frequency dependent diffusion equation in Eq. (3.32) with the boundary conditions

described by Eq. (3.116) and (3.119), which gives

$$
\mathcal{L}\{\tilde{c}\} = -\frac{\mathcal{L}\{\tilde{i}_f\}}{F\sqrt{D(j\omega + k)}\sinh\left(\sqrt{\frac{j\omega+k}{D}}L\right)}
$$

$$
\cdot\left\{K_5(\omega)\cosh\left[\sqrt{\frac{j\omega+k}{D}}(x-L)\right]\right.
$$

$$
\left. -K_6(\omega)\cosh\left(\sqrt{\frac{j\omega+k}{D}}x\right)\right\}
$$

$$
-\frac{\mathcal{L}\{\tilde{I}_0\}\alpha e^{-\alpha x}}{D\alpha^2 - k - j\omega}
$$

(3.120)

with

$$
K_5(\omega) = \frac{1 - t_-}{z_- \nu_-} - \frac{FD\,\mathcal{L}\{\tilde{I}_0\}\alpha^2}{\mathcal{L}\{\tilde{i}_f\}(D\alpha^2 - k - j\omega)}
$$

(3.121)

$$
K_6(\omega) = \frac{1 - t_-}{z_- \nu_-} - \frac{FD\,\mathcal{L}\{\tilde{I}_0\}\alpha^2 e^{-\alpha L}}{\mathcal{L}\{\tilde{i}_f\}(D\alpha^2 - k - j\omega)}
$$

(3.122)

The steady-state concentration is given by setting $\omega = 0$ in Eq. (3.120) and replace all time dependent quantities by steady-state ones

$$
c_e = -\frac{i_{f,e}}{F\sqrt{Dk}\sinh\left(\sqrt{\frac{k}{D}}L\right)}
$$

$$
\cdot\left\{K_{5,e}\cosh\left[\sqrt{\frac{k}{D}}(x-L)\right] - K_{6,e}\cosh\left(\sqrt{\frac{k}{D}}x\right)\right\} - \frac{I_0\alpha e^{-\alpha x}}{D\alpha^2 - k}
$$

(3.123)

with

$$
K_{5,e} = \frac{1 - t_-}{z_- \nu_-} - \frac{FDI_0\alpha^2}{i_{f,e}(D\alpha^2 - k)}
$$

(3.124)

$$
K_{6,e} = \frac{1 - t_-}{z_- \nu_-} - \frac{FDI_0\alpha^2 e^{-\alpha L}}{i_{f,e}(D\alpha^2 - k)}
$$

(3.125)

The contribution from the faradaic current in Eq. (3.126) is described by

$$
\mathcal{L}\{\tilde{c}_{i_f}\} = -\frac{\mathcal{L}\{\tilde{i}_f\}(1 - t_-)}{z_- \nu_- F\sqrt{D(j\omega + k)}\sinh\left(\sqrt{\frac{j\omega+k}{D}}L\right)}
$$

$$
\cdot\left\{\cosh\left[\sqrt{\frac{j\omega+k}{D}}(x-L)\right] - \cosh\left(\sqrt{\frac{j\omega+k}{D}}x\right)\right\}
$$

(3.126)

The contribution from the light intensity in Eq. (3.126) is described by

$$
\mathscr{L}\{\tilde{c}_{I_0}\} = \frac{\mathscr{L}\{\tilde{I}_0\}}{F\sqrt{D(j\omega + k)}\sinh\left(\sqrt{\frac{j\omega+k}{D}}L\right)}
$$

$$
\cdot \left\{ G_5(\omega)\cosh\left[\sqrt{\frac{j\omega + k}{D}}(x - L)\right] \right.
$$

$$
\left. - G_6(\omega)\cosh\left(\sqrt{\frac{j\omega + k}{D}}x\right)\right\} - \frac{\mathscr{L}\{\tilde{I}_0\}\alpha e^{-\alpha x}}{D\alpha^2 - k - j\omega}
$$

(3.127)

with

$$
G_5(\omega) = \frac{FD\alpha^2}{D\alpha^2 - k - j\omega}
$$

(3.128)

$$
G_6(\omega) = \frac{FD\alpha^2 e^{-\alpha L}}{D\alpha^2 - k - j\omega}
$$

(3.129)

Thus, we get the two "diffusion impedance" terms to insert in the IMPS transfer function in Eq. (3.105)

$$
Z_{D,i_f}(\omega, x) = -\frac{1 - t_-}{z_- \nu_- F\sqrt{D(j\omega + k)}\sinh\left(\sqrt{\frac{j\omega+k}{D}}L\right)}
$$

$$
\cdot \left\{\cosh\left[\sqrt{\frac{j\omega + k}{D}}(x - L)\right] - \cosh\left(\sqrt{\frac{j\omega + k}{D}}x\right)\right\}
$$

(3.130)

and

$$
Z_{D,I_0}(\omega, x) = \frac{1}{F\sqrt{D(j\omega + k)}\sinh\left(\sqrt{\frac{j\omega+k}{D}}L\right)}
$$

$$
\cdot \left\{ G_5(\omega)\cosh\left[\sqrt{\frac{j\omega + k}{D}}(x - L)\right] \right.
$$

$$
\left. - G_6(\omega)\cosh\left(\sqrt{\frac{j\omega + k}{D}}x\right)\right\} - \frac{\alpha e^{-\alpha x}}{D\alpha^2 - k - j\omega}
$$

(3.131)

The two latter models will not be investigated further in this study, but it is recommended to study these simplifications and alterations to in general investigate IMPS transfer functions in more detail.

### 3.3.7   Relation between measured potential, faradaic current density, and light intensity

In order to explain the resulting impedance spectra of the photoelectrochemical thin film transfer functions described above, a relation between measured potential, faradaic current density, and light intensity under steady-state conditions is developed.

We assume a mixed conducting thin film electrode, as described in Section 3.3. The steady-state

diffusion equation in Eq. (3.11) has the specific solution Eq. (3.27)

$$
\begin{aligned}
c_e(x) = & -\frac{i_{f,e}}{F\sqrt{Dk}\sinh\left(\sqrt{\frac{k}{D}}L\right)} \\
& \cdot \left\{ K_{1,e}\cosh\left[\sqrt{\frac{k}{D}}(x-L)\right] - K_{2,e}\cosh\left(\sqrt{\frac{k}{D}}x\right) \right\} \\
& -\frac{I_0\alpha e^{-\alpha x}}{D\alpha^2 - k}
\end{aligned}
\tag{3.132}
$$

with

$$
K_{1,e} = \frac{1 - t_-}{z_- v_-} - \frac{FDI_0\alpha^2}{i_{f,e}(D\alpha^2 - k)}
\tag{3.133}
$$

$$
K_{2,e} = \frac{1 - t_+}{z_+ v_+} - \frac{FDI_0\alpha^2 e^{-\alpha L}}{i_{f,e}(D\alpha^2 - k)}
\tag{3.134}
$$

The potential is related to the faradaic current density by Eq. (3.14) in one dimension

$$
F\frac{\partial \Phi_{1,e}}{\partial x} = \frac{i_{f,e}}{z_+ v_+ F c_e(z_+ u_+ - z_- u_-)} - \frac{D_+ - D_-}{c_e(z_+ u_+ - z_- u_-)}\frac{\partial c_e}{\partial x}
\tag{3.135}
$$

The potential as a function of $x$ may be calculated by integrating Eq. (3.135) from an arbitrary $x$-value to $x = L$, where we assume that the potential is fixed at $x = L$

$$
F\Phi_{1,e}(x) = F\Phi_{1,e}(L) - \int_x^L \frac{i_{f,e}}{z_+ v_+ F c_e(z_+ u_+ - z_- u_-)} + \frac{D_+ - D_-}{c_e(z_+ u_+ - z_- u_-)}\frac{\partial c_e}{\partial x}\, dx
\tag{3.136}
$$

At the electrolyte interface ($x = 0$), we assume that the faradaic current density is related to the potential by the kinetic expression in Eq. (3.40)

$$
\begin{aligned}
i_{f,e} &= \left(\frac{\partial i_{f,e}}{\partial x}\right)_{\Phi_{1,e}-\Phi_{2,e},x=0} c_e(0) + \left[\frac{\partial i_{f,e}}{\partial\left(\Phi_{1,e}-\Phi_{2,e}\right)}\right]_{c_e,x=0} \left[\Phi_{1,e}(0) - \Phi_{2,e}(0)\right] \\
&= A_0 c_e(0) + B_0\left[\Phi_{1,e}(0) - \Phi_{2,e}(0)\right]
\end{aligned}
\tag{3.137}
$$

We insert the expression for the potential evaluated at $x = 0$ described by Eq. (3.136)

$$
\begin{aligned}
i_{f,e} = A_0 c_e(0) + B_0 \Big\{ & \Phi_{1,e}(L) - \Phi_{2,e}(0) \\
& -\int_0^L \frac{i_{f,e}}{z_+ v_+ F^2 c_e(z_+ u_+ - z_- u_-)} + \frac{D_+ - D_-}{F c_e(z_+ u_+ - z_- u_-)}\frac{\partial c_e}{\partial x}\, dx \Big\}
\end{aligned}
\tag{3.138}
$$

The potential at the support interface $\Phi_{1,e}(L)$ becomes

$$\begin{aligned}
\Phi_{1,e}(L) = &\frac{i_{f,e} - A_0 c_e(0)}{B_0} + \Phi_{2,e}(0) \\
&+ \int_0^L \frac{i_{f,e}}{z_+ \nu_+ F^2 c_e(z_+ u_+ - z_- u_-)} - \frac{D_+ - D_-}{F c_e(z_+ u_+ - z_- u_-)} \frac{\partial c_e}{\partial x} dx
\end{aligned} \tag{3.139}$$

At the interface to electrode support connecting the electrode, we assume the equilibrium in Eq. (3.45)

$$0 \rightleftharpoons \mathrm{h}^+ + \mathrm{e}^- \tag{3.140}$$

The measured potential is related to the electrochemical potential in a reference electrode as $FV = \mu_e^{\mathrm{ref}} - \mu_e$, which gives the measured potential through the dilute solution limit (Eq.(3.46) and (3.46))

$$FV = \mu_h^0 + \mu_e^{\mathrm{ref}} + RT \ln c_e(L) + F\Phi_{1,e}(L) \tag{3.141}$$

We assume that $\mu_e^{\mathrm{ref}}$ can be measured by a reference electrode so that its value is representative of $\Phi_{2,e}(0)$ plus a constant, that is $\mu_i^{\mathrm{ref}} = \mu_i^0 + z_i F\Phi_i$. Combination of Eq. (3.141) and (3.139) gives the final expression for the measured potential

$$\begin{aligned}
FV = &\mu^0 + RT \ln c_e(L) + \frac{F\left[i_{f,e} - A_0 c_e(0)\right]}{B_0} \\
&+ \int_0^L \frac{i_{f,e}}{z_+ \nu_+ F c_e(z_+ u_+ - z_- u_-)} - \frac{D_+ - D_-}{c_e(z_+ u_+ - z_- u_-)} \frac{\partial c_e}{\partial x} dx
\end{aligned} \tag{3.142}$$

where we have defined $\mu^0 = \mu_h^0 + \mu_e^0$. We see from Eq. (3.142) that the measured potential is a function of the faradaic current density and the light intensity, since the steady-state concentration profile is a function faradaic current density and light intensity. Thus, Eq. (3.142) may be used to investigate the relation between these three parameters, and may assist in explaining the resulting impedance spectra.

## 3.4   IMPS study of a microporous mixed conducting thin film electrode

### 3.4.1   Solving the diffusion equation for a microporous electrode under short circuit conditions

To include micropores in the system, we assume that the sink term in the diffusion equation may be interpreted as the rate for a recombination process of charge transfer between the electrode interface and the electrolyte across the micropore. This is illustrated in Figure 3.7, where we assume a straight pore with depth $L$. The transient line of the current is also given.
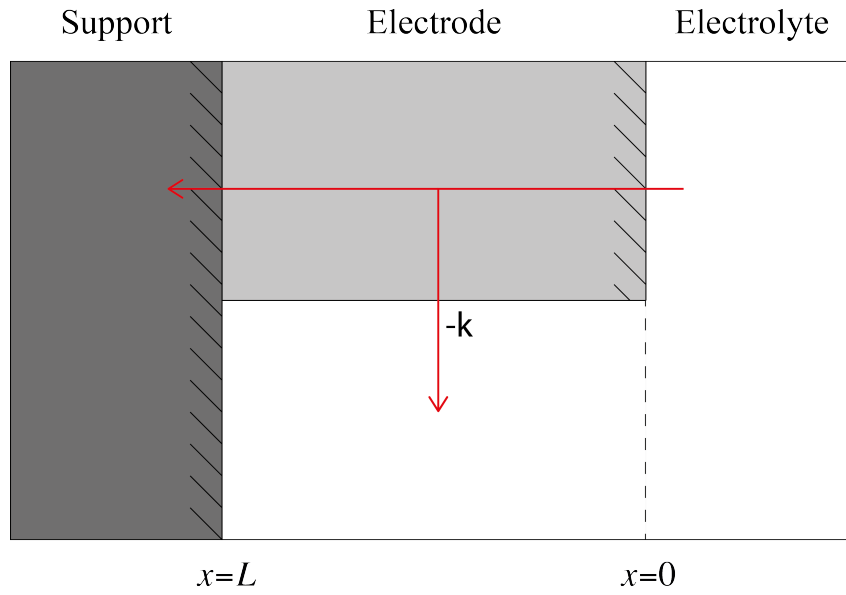
Support    Electrode    Electrolyte



$x=L$    $x=0$

Figure 3.7: Schematic of a micropore in the microporous thin film electrode. The sink term in the diffusion equation is interpreted as a charge transfer process between the electrode material and the electrolyte across the pore wall.

We solve the diffusion equation from Eq. (3.32)

$$s\mathcal{L}\{\tilde{c}\} = D\frac{\partial^2 \mathcal{L}\{\tilde{c}\}}{\partial x^2} - k\mathcal{L}\{\tilde{c}\} + \mathcal{L}\{\tilde{I}_0\}\alpha e^{-\alpha x} \tag{3.143}$$

with boundary conditions under short circuit conditions described by Södergren et. al [11]

$$\frac{\partial \mathcal{L}\{\tilde{c}\}}{\partial x}\bigg|_{x=0} = 0; \qquad \mathcal{L}\{\tilde{c}(x=L)\} = 0 \tag{3.144}$$

Here, we essentially have assumed that the $\mathcal{L}\{\tilde{c}(x=L)\} = 0$, as the concentration at the back support is kept constant caused by the short circuit condition [11]. We also assume that charge carriers reaching the outermost part of the microporous film will be reflected and diffuse back to the film [11] resulting in a negligible current flow at $x = 0$. This gives the solution

$$\mathcal{L}\{\tilde{c}\} = -\frac{\mathcal{L}\{\tilde{I}_0\}}{(D\alpha^2 - k - j\omega)\sqrt{j\omega + k}\cosh\left(\sqrt{\frac{j\omega+k}{D}}L\right)}$$
$$\cdot \left\{\alpha^2\sqrt{D}\sinh\left[\sqrt{\frac{j\omega+k}{D}}(x-L)\right]\right. \tag{3.145}$$
$$\left. -\alpha\sqrt{j\omega+k}e^{-\alpha L}\cosh\left(\sqrt{\frac{j\omega+k}{D}}x\right)\right\} - \frac{\mathcal{L}\{\tilde{I}_0\}\alpha e^{-\alpha x}}{D\alpha^2 - k - j\omega}$$

### 3.4.2   IMPS transfer function for the microporous thin film

For intensity-modulated photocurrent spectroscopy (IMPS) measurements we apply a harmonically perturbed light intensity and measure the current response under short circuit conditions. That is

$$
\begin{aligned}
&\mathcal{L}\{\tilde{i}_f\} \neq 0; \qquad i_{f,e} \neq 0; \quad \mathcal{L}\{\tilde{V}\} = 0 \\
&I_0(x,0) \neq 0; \quad \mathcal{L}\{\tilde{I}_0\} \neq 0
\end{aligned}
\tag{3.146}
$$

The IMPS transfer function is given by

$$
Z_\phi(j\omega) = \frac{\mathcal{L}\{\tilde{i}_f\}}{\mathcal{L}\{\tilde{I}_0\}}
\tag{3.147}
$$

The oscillating measured current density is proportional to the derivative of the oscillating concentration at the back support [11]. By assuming that electrons are blocked at $x = L$ as described in Section 3.3.1, we assume the relation

$$
\frac{\mathcal{L}\{\tilde{i}_f\}}{z_+ \nu_+ F} = \frac{D}{1 - t_+} \frac{\partial \mathcal{L}\{\tilde{c}\}}{\partial x}\bigg|_{x=L}
\tag{3.148}
$$

Thus, the faradaic current is given by

$$
\begin{aligned}
\mathcal{L}\{\tilde{i}_f\} = &-\frac{\mathcal{L}\{\tilde{I}_0\} z_+ \nu_+ F \sqrt{D}}{(D\alpha^2 - k - j\omega)(1 - t_+)\cosh\left(\sqrt{\frac{j\omega + k}{D}} L\right)} \\
&\cdot \left\{\alpha^2 \sqrt{D} - \alpha\sqrt{j\omega + k}\, e^{-\alpha L}\sinh\left(\sqrt{\frac{j\omega + k}{D}} L\right)\right\} + \frac{\mathcal{L}\{\tilde{I}_0\}\alpha^2 e^{-\alpha L}}{D\alpha^2 - k - j\omega}
\end{aligned}
\tag{3.149}
$$

This transfer function can readily be found by the expression for the current density in Eq. (3.149)

$$
\begin{aligned}
Z_\phi(j\omega) = &-\frac{z_+ \nu_+ F \sqrt{D}}{(D\alpha^2 - k - j\omega)(1 - t_+)\cosh\left(\sqrt{\frac{j\omega + k}{D}} L\right)} \\
&\cdot \left\{\alpha^2 \sqrt{D} - \alpha\sqrt{j\omega + k}\, e^{-\alpha L}\sinh\left(\sqrt{\frac{j\omega + k}{D}} L\right)\right\} + \frac{\alpha^2 e^{-\alpha L}}{D\alpha^2 - k - j\omega}
\end{aligned}
\tag{3.150}
$$

# 4 Results

## 4.1 Introduction

Below, we calculate the derived impedance transfer functions in Section 3. In Section 4.2 we introduce the simulation parameters assuming an iridium oxide electrode immersed in a binary electrolyte. In Section 4.3 the impedance spectra for the thin film electrode described in Section 3.3 are calculated. In Section 4.3.1 the numerical approach using Newman's BAND(J) subroutine is investigated briefly. In Section 4.3.2 the faradaic electrochemical impedance spectrum from Eq. (3.53) is studied. The photoelectrochemical impedance spectrum under steady-state illumination from Eq. (3.3.4) is studied in section 4.3.3. In Section 4.3.4, the IMVS transfer function from Eq. (3.84) is studied, and the IMPS transfer function from Eq. (3.105) is studied in Section 4.3.5. Finally, the IMPS transfer function for a microporous thin film electrode from Eq. (3.150) is briefly studied in Section 4.4.

## 4.2 Simulation parameters

We assume Butler-Volmer type kinetics

$$
\begin{aligned}
i_f = i_0 \left\{ \exp\left( \frac{(1-\beta)F(\Phi_1 - \Phi_2 - U)}{RT} \right) \right. \\
\left. - \exp\left( \frac{-\beta F(\Phi_1 - \Phi_2 - U)}{RT} \right) \right\}
\end{aligned}
\tag{4.1}
$$

By assuming $A_0 = A_L = A$ and $B_0 = B_L = B$ in Eq. (3.40) and (3.43), we get directly from Eq. (4.1)

$$
A = \frac{i_0 F}{RT} \frac{\partial U}{\partial c}, \quad B = \frac{i_0 F}{RT}
\tag{4.2}
$$

The diffusion coefficients for each species are calculated by using Nernst-Einstein relation [30]

$$
D_i = \frac{k_B T}{q_i} u_i'
\tag{4.3}
$$

and the diffusion coefficient for the system is given by [30]

$$
D = \frac{z_+ u_+ D_- - z_- u_- D_+}{z_+ u_+ - z_- u_-}
\tag{4.4}
$$

where $k_B$ is the Boltzmann constant, $q_i$ is the charge of the species, $z_i$ is the valence of the species and $u_i$ is the mobility of the species. Here we have used a different version of the Nernst-Einstein relation than the one given in the theory section, in accordance with Sunde et al. [29].

The conductivity of the electrode material is given by [30]

$$\kappa = F^2 \sum_i z_i^2 u_i c_i \qquad (4.5)$$

The transport numbers are given by [30]

$$t_j = \frac{z_j^2 u_j c_j}{\sum_i z_i^2 u_i c_i} \qquad (4.6)$$

The steady-state incident light illumination $I_0$ is assumed to be 0.7 W m$^{-2}$ with a wavelength $\lambda =$ 545 nm, as described by Zanden et al. [26]. This is converted into the proper unit of mol m$^{-2}$ s$^{-1}$ by using the expression for the photon energy $E_{\mathrm{ph}}$

$$E_{\mathrm{ph}} = \frac{hc}{\lambda} \qquad (4.7)$$

where $h = 6.63 \times 10^{-34}$ Js is the planck constant, and $c = 3 \times 10^8$ m s$^{-1}$ is the speed of light. This gives a light intensity of $I_0 = 3 \times 10^{-6}$ mol m$^{-2}$ s$^{-1}$, which is used if not otherwise stated.

The material simulation parameters are given in Table 4.1, where we have assumed an iridium oxide electrode immersed in a binary electrolyte. The values are given by Sunde et al. [29], if not otherwise stated. The calculated values are given in Table 4.2. When appropriate, the modulating faradaic current and modulated illumination is set to unity for simplicity, since these term is cancelled when the impedance is calculated.

From the material properties given in Table 4.1, we get one transport number close to unity and one transport number close to zero, thus mixed conductivity is minimal. To investigate the introduction of mixed conductivity, we define a system with equal transport numbers $t_+ = t_- = 0.5$. Mathematically, this is achieved by setting the mobilities of the charge species equal. We assume a system similar to that defined in Table 4.1, but with mobilities $u'_+ = u'_- = 3.5 \times 10^{-8}$ cm$^2$ (V s)$^{-1}$ to keep the diffusion coefficient equal for the to cases.

## 4.3   Photoelectrochemical thin film electrode

### 4.3.1   Numerical solution of the diffusion equation with Newmans BAND subroutine

In previous work [31], a study of solving the frequency dependent diffusion equation in Eq. (3.32) in order to calculate the electrochemical impedance spectrum for a thin film electrode with mixed conductivity was derived.

In Figure 4.1, the impedance plane plot of electrochemical impedance spectrum in Eq. (3.53) solved both analytically and solved by numerical approximation of the diffusion equation for a thin

Table 4.1: Simulation parameters for the iridium oxide system.

| Parameter | Value | Unit | Reference |
|---|---|---|---|
| $c_0$ | 0.025 | mol cm$^{-3}$ | – |
| $c_e$ | 0.004 | mol cm$^{-3}$ | – |
| $z_+$ | 1 | – | – |
| $z_-$ | -1 | – | – |
| $\nu_+$ | 1 | – | – |
| $\nu_-$ | 1 | – | – |
| $u'_+$ | 0.1 | cm$^2$ (V s)$^{-1}$ | – |
| $u'_-$ | $1.7 \times 10^{-8}$ | cm$^2$ (V s)$^{-1}$ | – |
| $i_0$ | $0.69 \times 10^{-3}$ | A cm$^{-2}$ | – |
| $\partial U / \partial c$ | -20.27 | V cm$^3$ mol$^{-1}$ | – |
| $k$ | $1 \times 10^{-2}$ | s$^{-1}$ | – |
| $L$ | 100 | $\mu$m | – |
| T | 353.15 | K | – |

Table 4.2: Calculated simulation parameters from Table 4.1.

| Parameter | Value | Unit | Reference |
|---|---|---|---|
| $1/B$ | 44.06 | $\Omega$ cm$^2$ | – |
| A | -0.46 | A cm mol$^{-1}$ | – |
| D | $1 \times 10^{-9}$ | cm$^2$ s$^{-1}$ | – |

Table 4.3: Constants and assumed simulation parameters for impedance spectra calculations.

| Parameter | Value | Unit | Reference |
|---|---|---|---|
| $F$ | 96485 | A s mol$^{-1}$ | – |
| $k_B$ | $8.618 \times 10^{-5}$ | eV K$^{-1}$ | – |
| $I_0$ | $3 \times 10^{-6}$ | mol m$^{-2}$ s$^{-1}$ | [26] |
| $\alpha$ | 2500 | cm$^{-1}$ | [24] |
| $\mathscr{L}\{\tilde{i}_f\}$ | 1 | A cm$^{-2}$ | – |
| $\mathscr{L}\{\tilde{I}_0\}$ | 1 | mol m$^{-2}$ s$^{-1}$ | – |

film electrode described by Table 4.1 and 4.2 is given. Calculations are done for a frequency region of $10^{-7} - 10^3$ Hz and an effective rate constant $k = 10^{-2}$ s$^{-1}$. The numerical approximation is calculated for 1000 steps. We observe a small deviance from the analytical solution in the high frequency, as described by Småbråten [31].
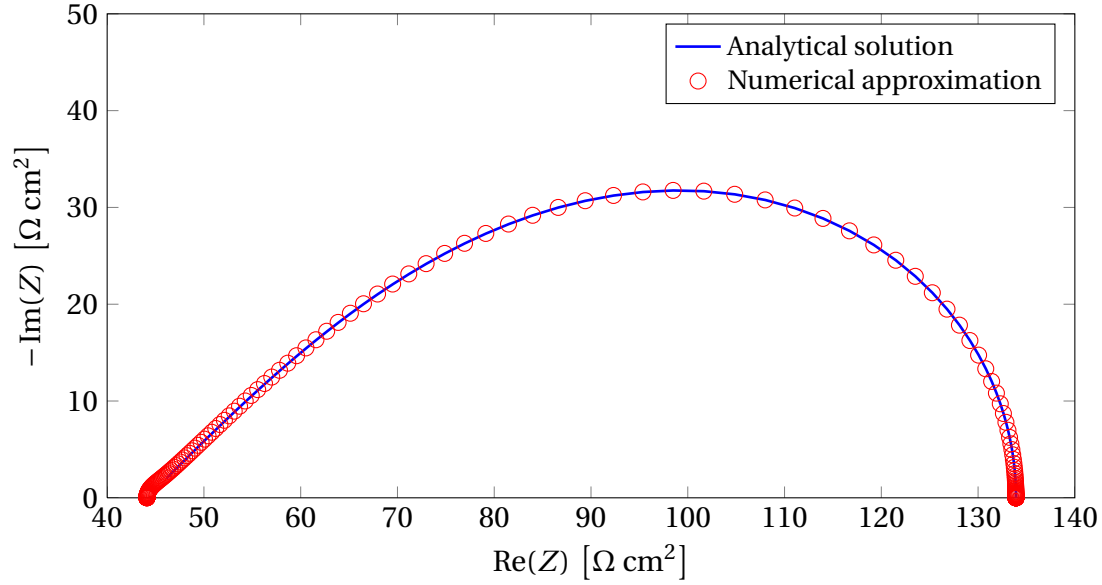


Figure 4.1: Analytical solution and numerical approximation of the electrochemical impedance spectrum in Eq. (3.53) for a thin film electrode. Calculations are done for an effective rate constant $k = 10^{-2}$ s$^{-1}$. The numerical approximation is calculated for 1000 steps.

In previous results [31], the general trend was that the numerical approximation with the BAND routine approaches the analytical solution when reducing the step size $H$. Newmans BAND routine is an approximation to the order $H^2$ [30], and should have an error proportional to $H^2$ for reasonably small values of $H$ [35]. Thus, the numerical approximation is expected to approach the analytical solution linearly with respect to $H^2$. This is investigated in Figure 4.2 for a simple dimensionless differential equation

$$\frac{\partial^2 c(y)}{\partial y^2} - c(y) = 0 \tag{4.8}$$

and boundary conditions

$$c(0) = 0; \qquad c(1) = 1 \tag{4.9}$$

with the specific solution $c(y) = \sinh(y)/\sinh(1)$, solved at $y = 0.5$. We do not observe the linear trend with respect to $H^2$. However the numerical approximation still approaches the analytical solution with decreasing step size, as expected. A similar trend is observed for the frequency dependent diffusion equation in Eq. (3.32).
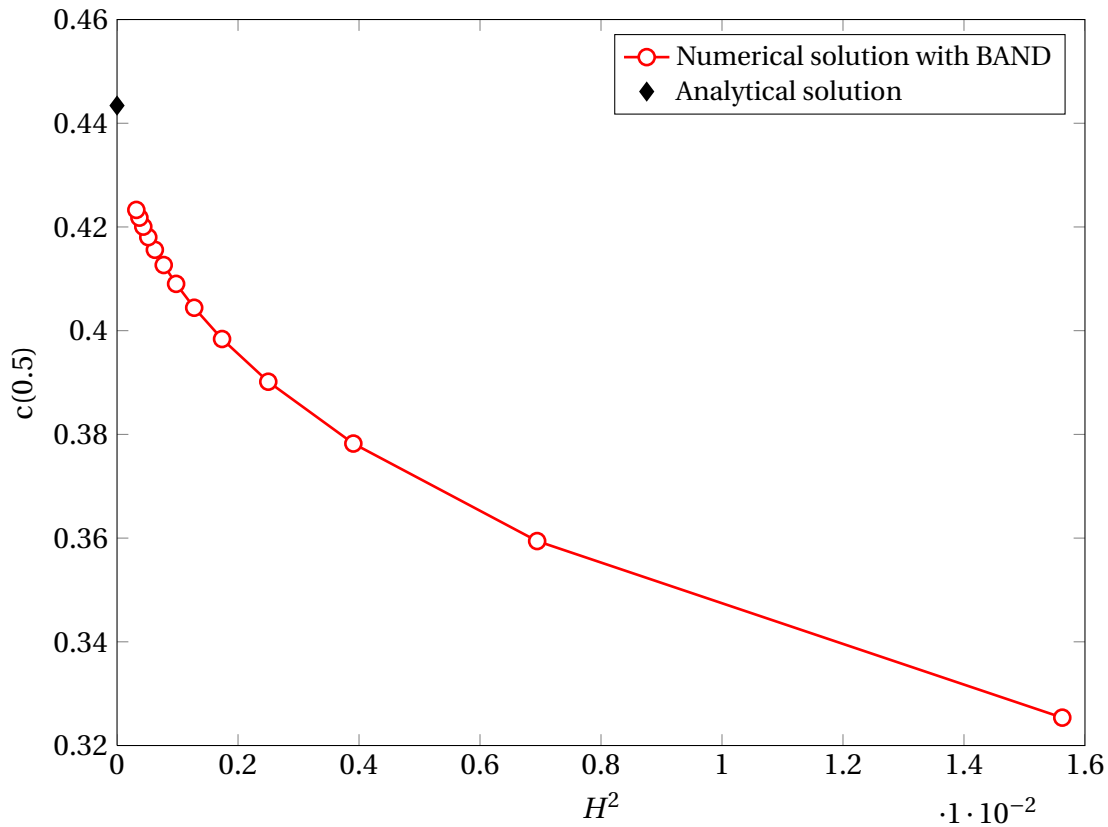
Figure 4.2: Plot of the numerical approach for Newmans BAND routine with respect to the square of the step size $H^2$ for the differential Eq. (4.8) with boundary conditions (4.9). Solved at $y = 0.5$.

### 4.3.2   Electrochemical impedance (EIS)
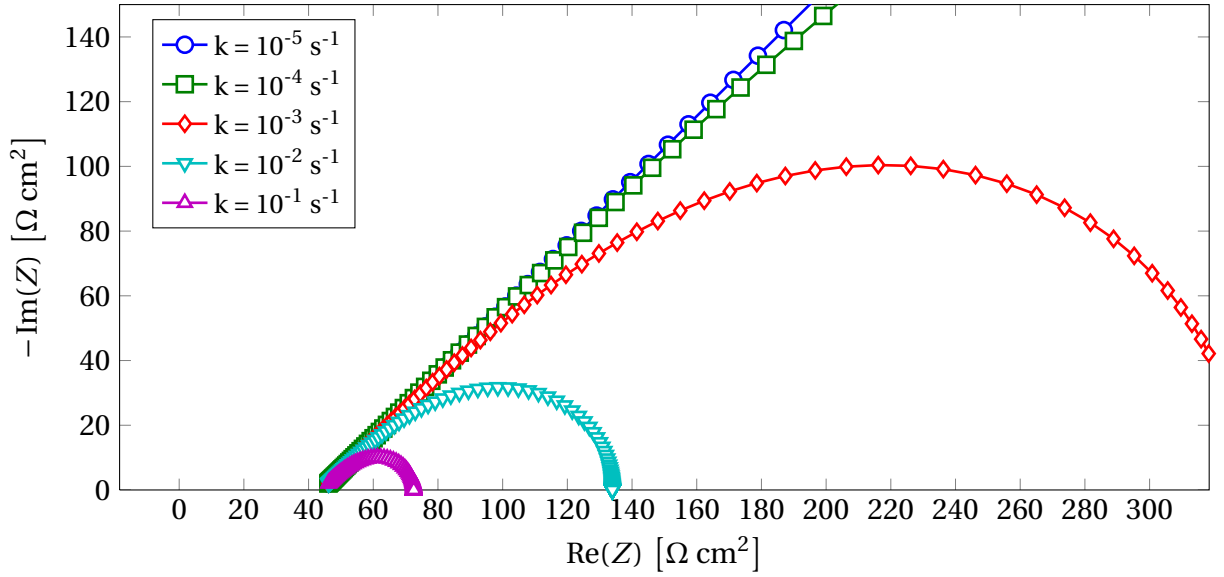
Figure 4.3 shows the impedance plane plot for the rate constant dependency of the electrochemical impedance spectrum in Eq. (3.53) for an electrode described in Section 4.2. In the high frequency region, a straight line with an angle of 45° is observed in the impedance plane plot, which corresponds to a diffusion limiting system described by the diffusion coefficient $D$. A dome is observed in the low frequency region, which indicates a rate limiting process. The impedance plane plot is zoomed in on the impedance spectrum for the largest $k$-value to visualize the change in the value of the impedance at different rate constants. By reducing the rate constant $k$, the impedance increases in absolute value of the real and imaginary parts. The trend in the impedance spectra, however, are similar, where the rate constant "bends" the impedance plane plot towards zero imaginary part in the low frequency region. The electrochemical impedance for the thin film electrode described by Eq. (3.53) is expected to show this reflective-like behavior, as found in previous work [31] The real part value of the low frequency intersect reduces with increasing rate constant. This indicates that the in the low frequency region, the measured impedance is approximately given by the sum og ohmic resistance in the electrode and electrolyte system.

The maximum in the imaginary part is located at a frequency equal to the chosen effective rate

Figure 4.3: Impedance plane plot of the rate constant dependency of the electrochemical impedance in Eq. (3.53) for an electrode described in Section 4.2. Calculations are done for a frequency region of $10^{-7}$–$10^3$ Hz, and for rate constants varying between $k = 10^{-5}$-1 s$^{-1}$

constant value $k$, as shown in the bode plot in Figure 4.4 of the imaginary part of the impedance as a function of angular frequency. Thus, the dome occurring in the impedance plane plot in Figure 4.3 should correspond to the recombination process described by the rate constant $k$, as expected [31].
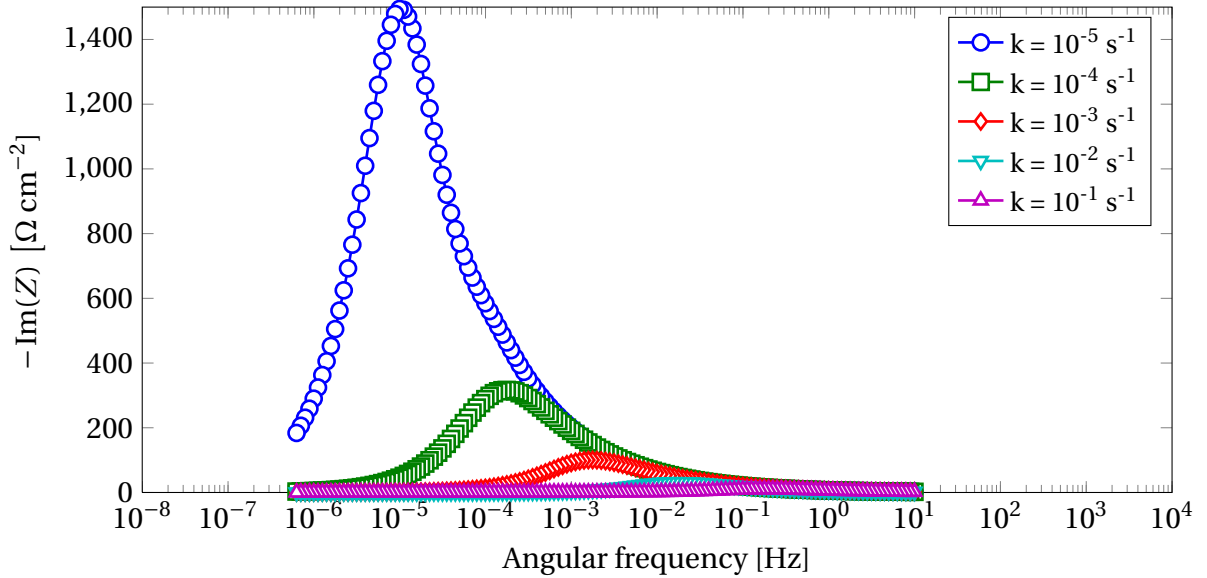


Figure 4.4: Bode plot of the imaginary part as a function of angular frequency, of the rate constant dependency of the electrochemical impedance in Eq. (3.53) for an electrode described in Section 4.2

### 4.3.3   Photoelectrochemical impedance (EIS)

Figure 4.5 shows the impedance plane plot of light intensity dependency for the photoelectrochemical impedance spectrum in in Eq. (3.70) for an electrode described in Section 4.2.  Calculations are

done for an effective rate constant $k = 10^{-2}$ s$^{-1}$, for a frequency region $10^{-7}$-$10^3$ Hz, for light intensities between $10^{-6}$ and 1 mol cm$^{-2}$ s$^{-1}$, and an applied steady-state current $i_{f,e} = 1$ A cm$^{-2}$.

The impedance is reduced by increasing the light intensity, since the increase in photogenerated charge carriers effectively reduces the current resistance in the system by increasing the flow of charge carriers. We observe a dome in the positive imaginary part of the impedance spectrum in the low frequency region for low light intensities. This shift in imaginary part indicates that the signal and response oscillates in opposite directions, and should correspond to a rate limiting back charge transfer process flowing in the opposite direction as the applied current. It is assumed that this process correspond to the electrode kinetics at the solution interface.
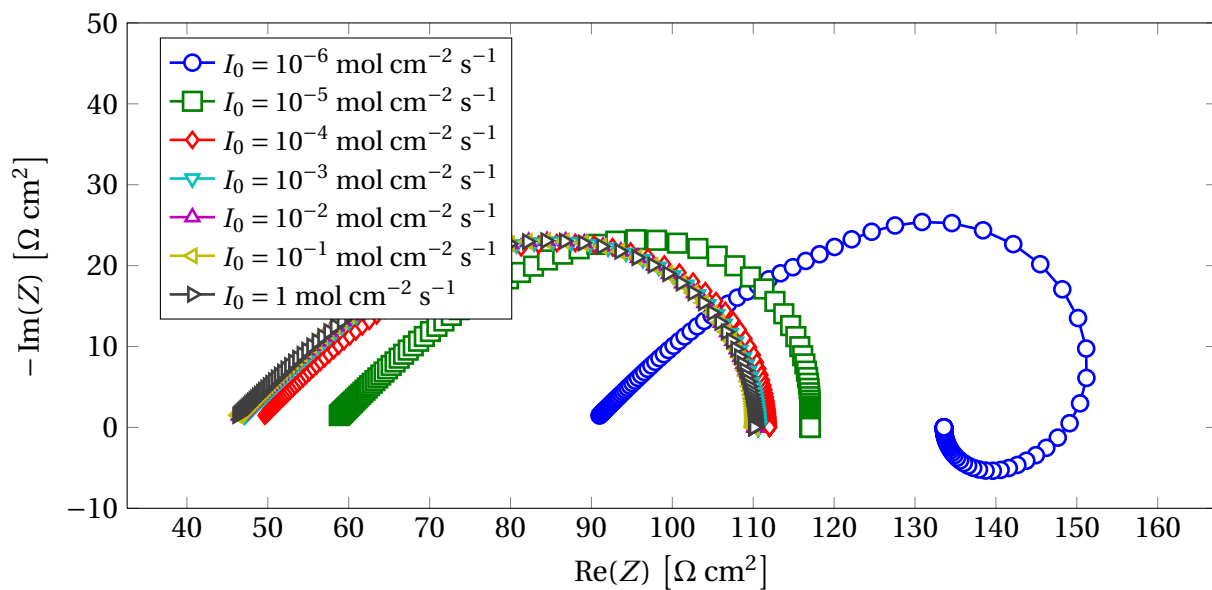


Figure 4.5: Impedance plane plot of the light intensity dependency for the impedance plane plot for the photoelectrochemical impedance in Eq. (3.70) for an electrode described in Section 4.2. Calculations are done for an effective rate constant $k = 10^{-2}$ s$^{-1}$, incident light intensities in the range of $I_0 = 10^{-6} - 1$ mol cm$^{-2}$ s$^{-1}$, a frequency region of $10^{-7}$–$10^3$ Hz, and an applied steady-state current $i_{f,e} = 1$ A cm$^{-2}$

The bode plot of the imaginary part of the photoelectrochemical impedance as a function of angular frequency is given in Figure 4.6. Here, we observe one maximum and one minimum for low light intensities, thus two distinct charge transfer processes are observed. The maximum should correspond to the recombination process described by the effective rate constant $k$, and the minimum should correspond to the rate of the electrode kinetics at the solution interface.

In Figure 4.7 the impedance plane plot of same system as described in Figure 4.5 is plotted for a lower applied steady-state faradaic current $i_{f,e} = 10^{-3}$ A cm$^{-2}$, to show the dependency of current density. The decrease in impedance with increasing light intensity is more prominent for lower current densities, which indicates that the electrode is more sensitive to light for low current density. The shift in sign of the phase is also more prominent by reducing the faradaic current density, which
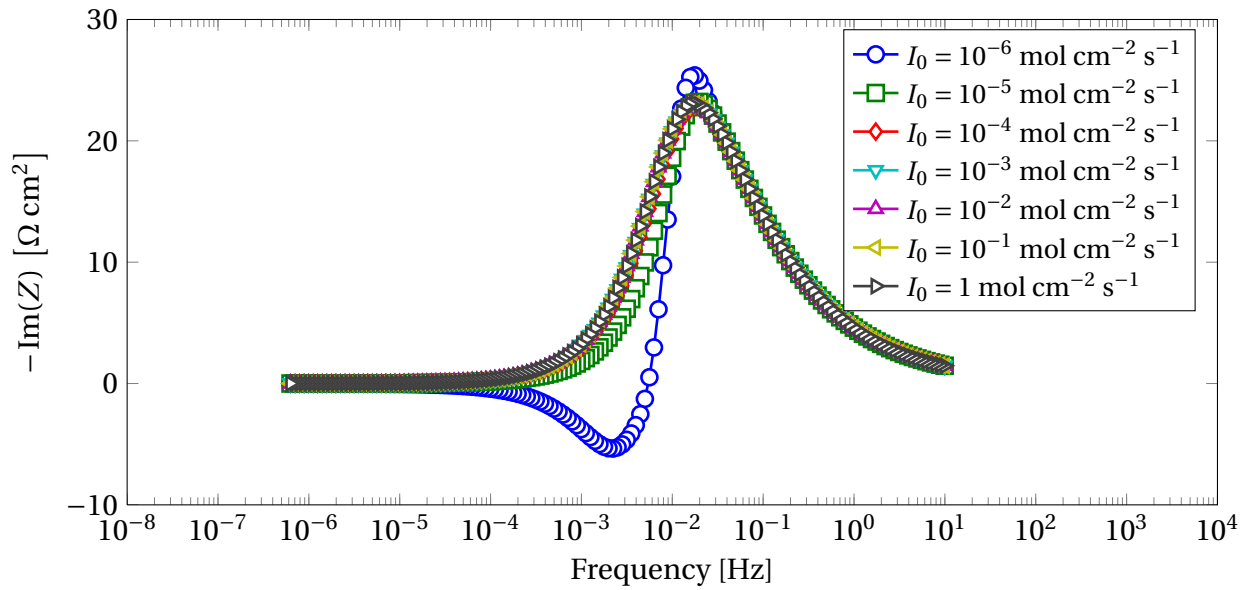
Figure 4.6: Corresponding bode plot of the imaginary part of the photoelectrochemical impedance as a function of angular frequency for the impedance plane plot in Figure 4.5.

indicates that the back charge transfer process corresponding to this dome increases with decreasing applied faradaic current density.
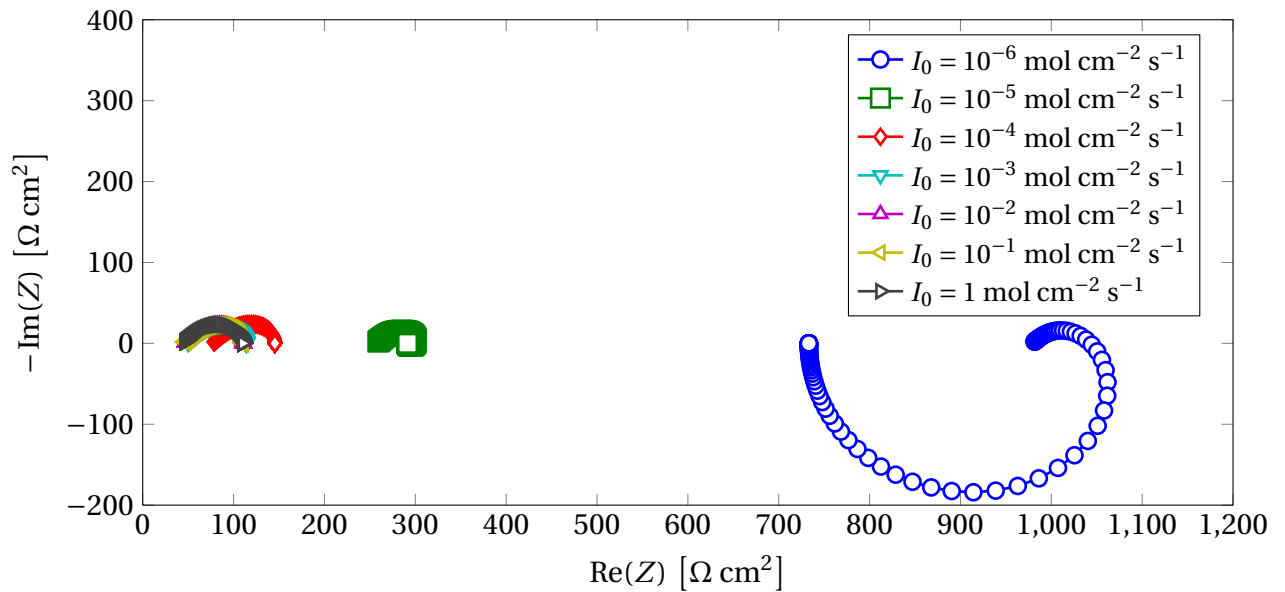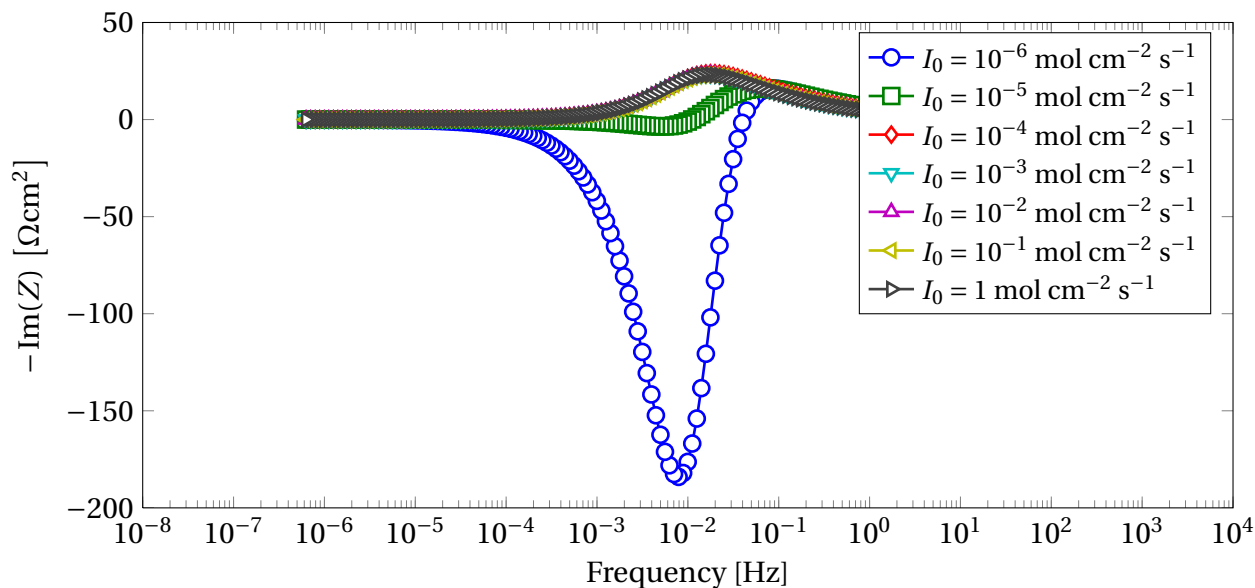


Figure 4.7: Impedance plane plot of the light intensity dependency for the same system described in Figure 4.5, but with a lower applied steady-state current $i_{f,e} = 10^{-3}$ A cm$^{-2}$

The corresponding bode plot of the imaginary part of the impedance plane plot in Figure 4.7 is given in Figure 4.8. Here, we observe to distinct charge transfer processes for higher light intensities. This indicates that by reducing the applied faradaic current density, the back charge transfer process occurs at higher light intensities. The back charge transfer process may thus be eliminated for a chosen light intensity by increasing the applied current density.

Figure 4.8: Corresponding bode plot of the imaginary part of the photoelectrochemical impedance as a function of angular frequency for the impedance plane plot in Figure 4.5.

Figure 4.9 shows calculations for the same system described in Figure 4.5, but with a lower effective rate constant of $k = 10^{-3}$ s$^{-1}$. No apparent light intensity of the photoelectrochemical impedance is observed, as shown in the impedance plane plot in Figure 4.9a. Only one dome is observed, and from the bode plot in Figure 4.9b, this dome should correspond to the recombination process described by the effective rate constant $k$. We expect that when the recombination rate constant $k$ is lower than the back charge transfer process rate, only one dome in the photoelectrochemical impedance spectrum is observed. In Figure 4.10 calculations for the same system as presented in Figure 4.5, but with equal transport, numbers is given. For low light intensities, a "snail house" effect with four domes is observed. This indicates that four charge transfer limiting processes may occur in the system with different rates. Possible processes may be recombination of charge carriers defined by the effective rate constant $k$, charge transfer at the solution interface defined by the electrode kinetics, charge transfer at the support interface defined by the electrode kinetics, and charge transfer at the counter electrode. The magnitude of the impedance has also increased, and may be caused by the reduced mobility of positive species.

The same calculations for an applied faradaic current density $i_{f,e} = 10^{-3}$ A cm$^{-2}$ is given in Figure 4.11, where a similar "snail house" effect is observed. The magnitude of the impedance has also increased with decreasing applied current density.

In Figure 4.12 calculations for the same system as presented in Figure 4.9a, but with equal transport numbers, is given. We see a similar trend as previous results, however, the system shows a larger light intensity dependency. Also, the magnitude of the impedance is reduced.

In Figure 4.13 we reduce the applied faradaic current density to $i_{f,e} = 10^{-3}$ A cm$^{-2}$. Now, we ob-
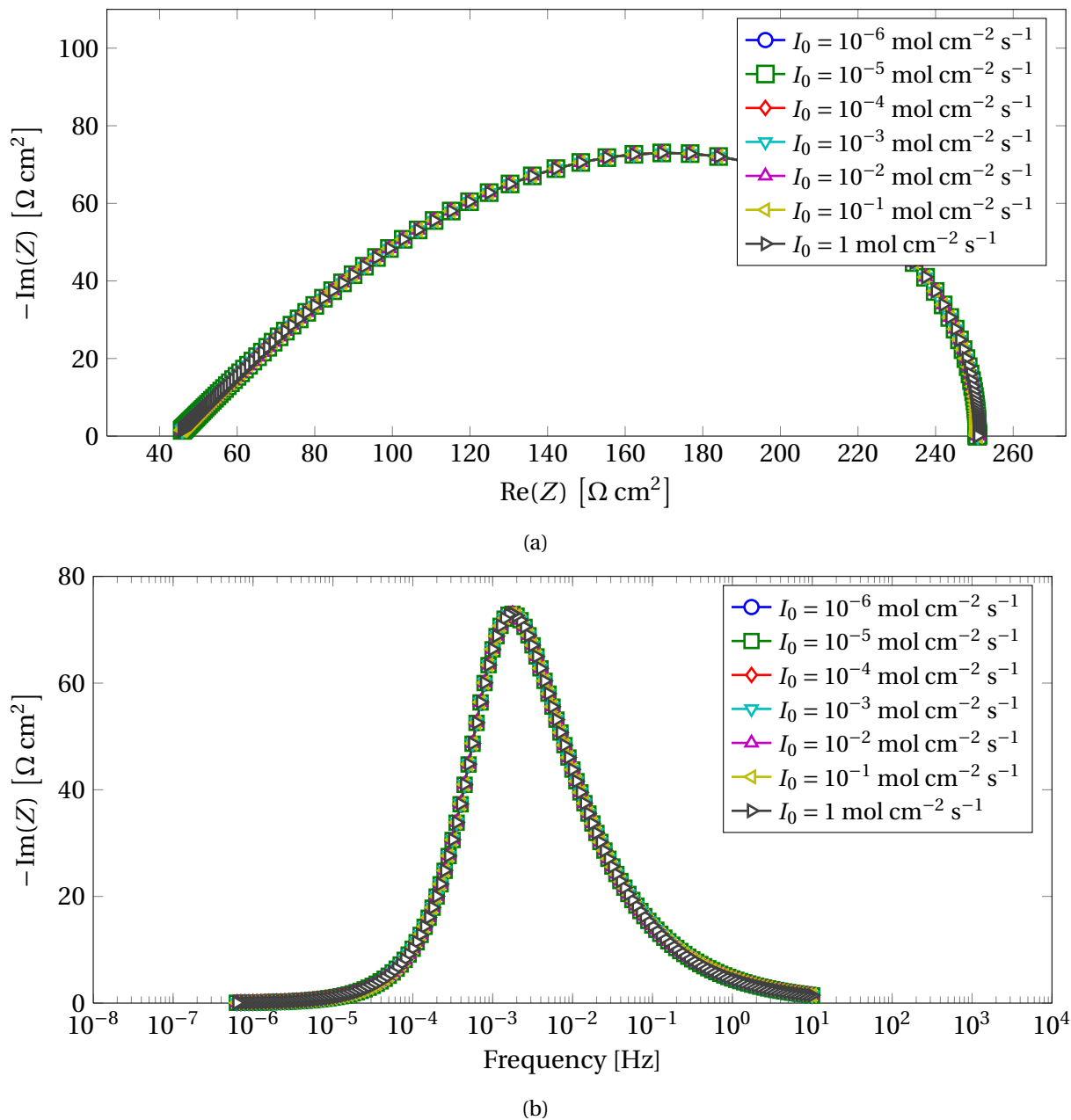
(a)



(b)

Figure 4.9: aLight intensity dependency of the impedance plane plot of the photoelectrochemical impedance in Eq. (3.70) for an electrode described in Section 4.2. Calculations are done for an effective rate constant $k = 10^{-3}$ s$^{-1}$, incident light intensities in the range of $I_0 = 10^{-6} - 1$ mol cm$^{-2}$ s$^{-1}$, a frequency region of $10^{-7}$–$10^3$ Hz, and an applied steady-state current $i_{f,e} = 1$ A cm$^{-2}$. b Corresponding bode plot.
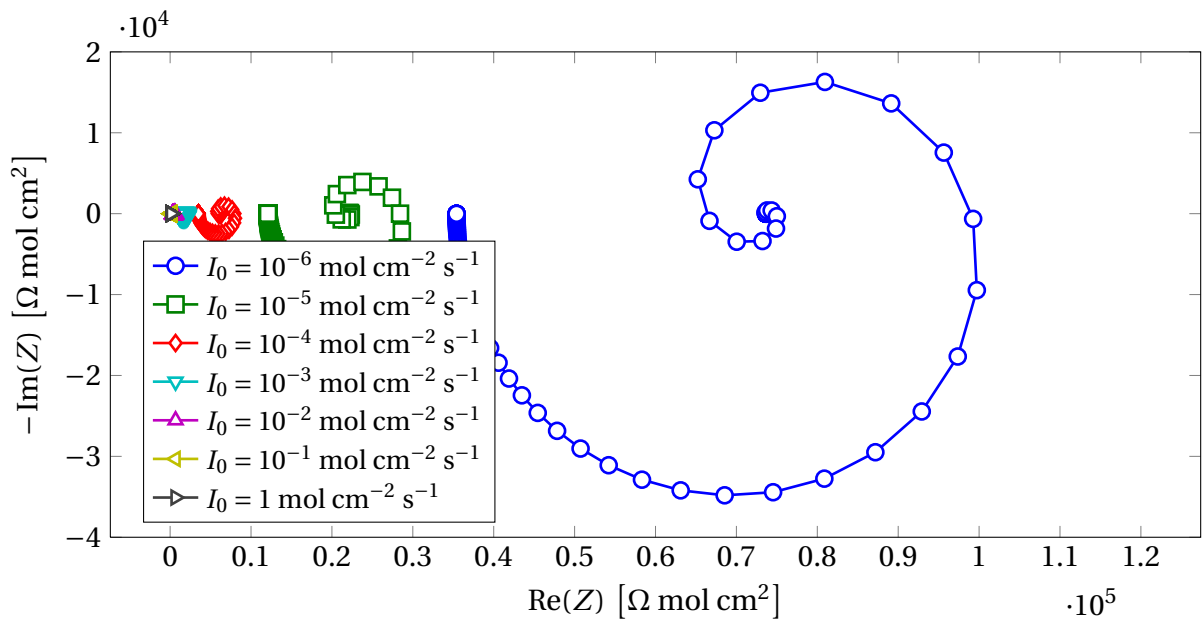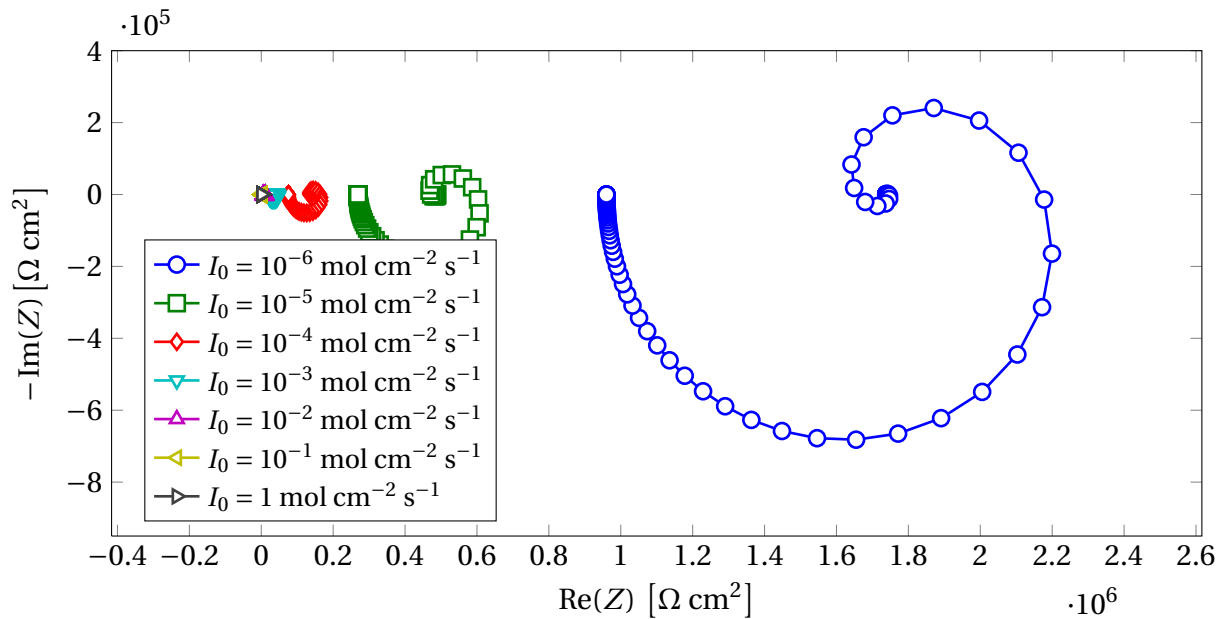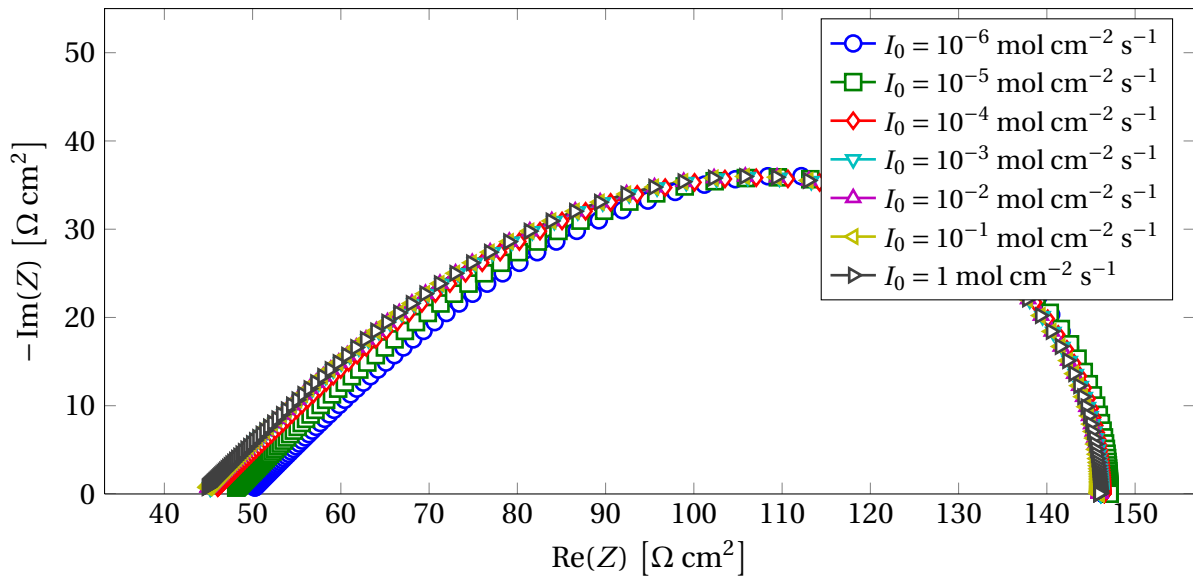
Figure 4.10: Impedance plane plot of the light intensity dependency for the impedance plane plot for the photoelectrochemical impedance in Eq. (3.70) for an electrode described in Section 4.2 with equal transport numbers. Calculations are done for an effective rate constant $k = 10^{-2}$ s$^{-1}$, incident light intensities in the range of $I_0 = 10^{-6} - 1$ mol cm$^{-2}$ s$^{-1}$, a frequency region of $10^{-7}$–$10^3$ Hz, and an applied steady-state current $i_{f,e} = 1$ A cm$^{-2}$
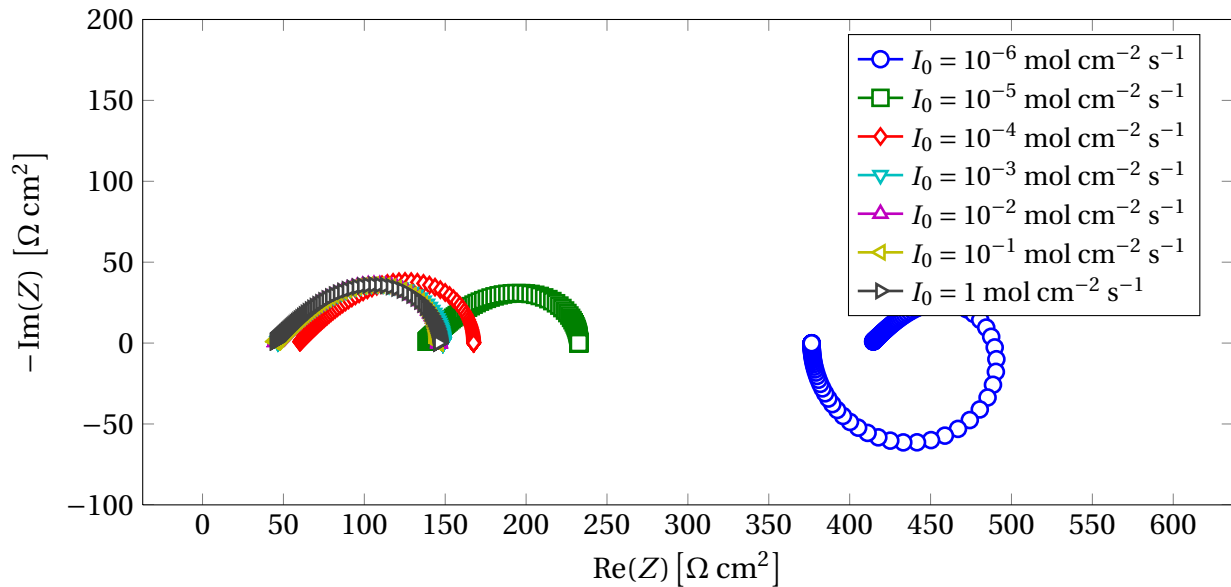


Figure 4.11: Impedance plane plot of the light intensity dependency for the same system described in Figure 4.10, but with a lower applied steady-state current $i_{f,e} = 10^{-3}$ A cm$^{-2}$

Figure 4.12: Impedance plane plot of the light intensity dependency for the impedance plane plot for the photoelectrochemical impedance in Eq. (3.70) for an electrode described in Section 4.2 with equal transport numbers. Calculations are done for an effective rate constant $k = 10^{-3}$ s$^{-1}$, incident light intensities in the range of $I_0 = 10^{-6} - 1$ mol cm$^{-2}$ s$^{-1}$, a frequency region of $10^{-7}$–$10^3$ Hz, and an applied steady-state current $i_{f,e} = 1$ A cm$^{-2}$

serve two distinct domes in the impedance plane plot, where the high frequency dome is assumed to be corresponding to the recombination process described by the effective rate constant $k$. The low frequency dome is assumed to be corresponding to the back charge transfer at the solution interface described by the electrode kinetics, as in Figure 4.5.

### 4.3.4   Intensity-modulated photovoltage spectroscopy (IMVS)

The intensity-modulated photovoltage spectroscopy (IMVS) impedance spectrum from Eq. (3.84) for a photoelectrochemical thin film electrode described in Section 4.2 is given in Figures 4.14 to 4.19 for rate constants varying between $k = 10^{-5}$ and 1 s$^{-1}$.

In Figure 4.14 the IMVS response is given for a photoelectrochemical system described in Section 4.2 with an effective rate constant $k = 1$ s$^{-1}$. One dome in the impedance plane plot in Figure 4.14a is observed, and from the bode plot in Figure 4.14b this dome corresponds to the recombination process described by the effective rate constant $k$ since the maximum occurs at a value equal to the chosen $k$. The IMVS response is found to reduce with increasing light intensity.

Figure 4.15a gives the IMVS response for the same system as in Figure 4.14a, but with a lower effective rate constant $k = 10^{-1}$ s$^{-1}$. Again, one dome in the impedance plane plot in Figure 4.15a is observed, and from the bode plot in Figure 4.15b this dome should correspond to the recombination process defined by $k$. The impedance is reducing with increasing light intensity, but the effect is less apparent as for $k = 1$ s$^{-1}$. We also observe an increase in the magnitude of the impedance by reducing

Figure 4.13: Impedance plane plot of the light intensity dependency for the same system described in Figure 4.12, but with a lower applied steady-state current $i_{f,e} = 10^{-3}$ A cm$^{-2}$

the rate constant.

In Figure 4.16, the rate constant is reduced to $k = 10^{-2}$ s$^{-1}$. The dome in the impedance plane plot in Figure 4.16a should correspond to the recombination process described by $k$, as shown in the bode plot in Figure 4.16b. Only a small light intensity dependency is found in the low frequency region. The dome shape is slightly distorted in the high frequency region, indicating a mixed limiting process of charge transfer and diffusion.

By further reduction of the rate constant, as shown in Figure 4.17 and 4.18 for $k = 10^{-3}$ s$^{-1}$ and $k = 10^{-4}$ s$^{-1}$, respectively, no light intensity dependency is shown. The domes in the impedance plane plots in Figure 4.17a and 4.18a again correspond to the recombination process, as shown in the bode plots in Figure 4.17b and 4.18b, respectively. Also, the distortion of the dome is more apparent by lowering the rate constant, and for $k = 10^{-4}$ a clear straight line corresponding to a diffusion limiting process is observed.

In Figure 4.19, the rate constant is reduced to $k = 10^{-5}$ s$^{-1}$. Here, we observe an impedance plane plot similar to a reflective-like behavior. The photopotential change is thus clearly diffusion limited in the high frequency region and charge transfer limited caused by the recombination process described by $k$ when the rate constant is sufficiently low. In Figure 4.20a the IMVS impedance plane plot for an effective rate constant $k = 1$ s$^{-1}$ and equal transport numbers is given. We observe no significant change compared to Figure 4.14a for transport numbers close to zero and unity. The same is observed for lower rate constants, here shown for $k = 10^{-5}$ s$^{-1}$ in Figure 4.20b. This is to be expected, as the IMVS transfer function is independent of the transport number, in accordance with the expression for the modulating concentration profile under open circuit conditions in Eq. (3.74).
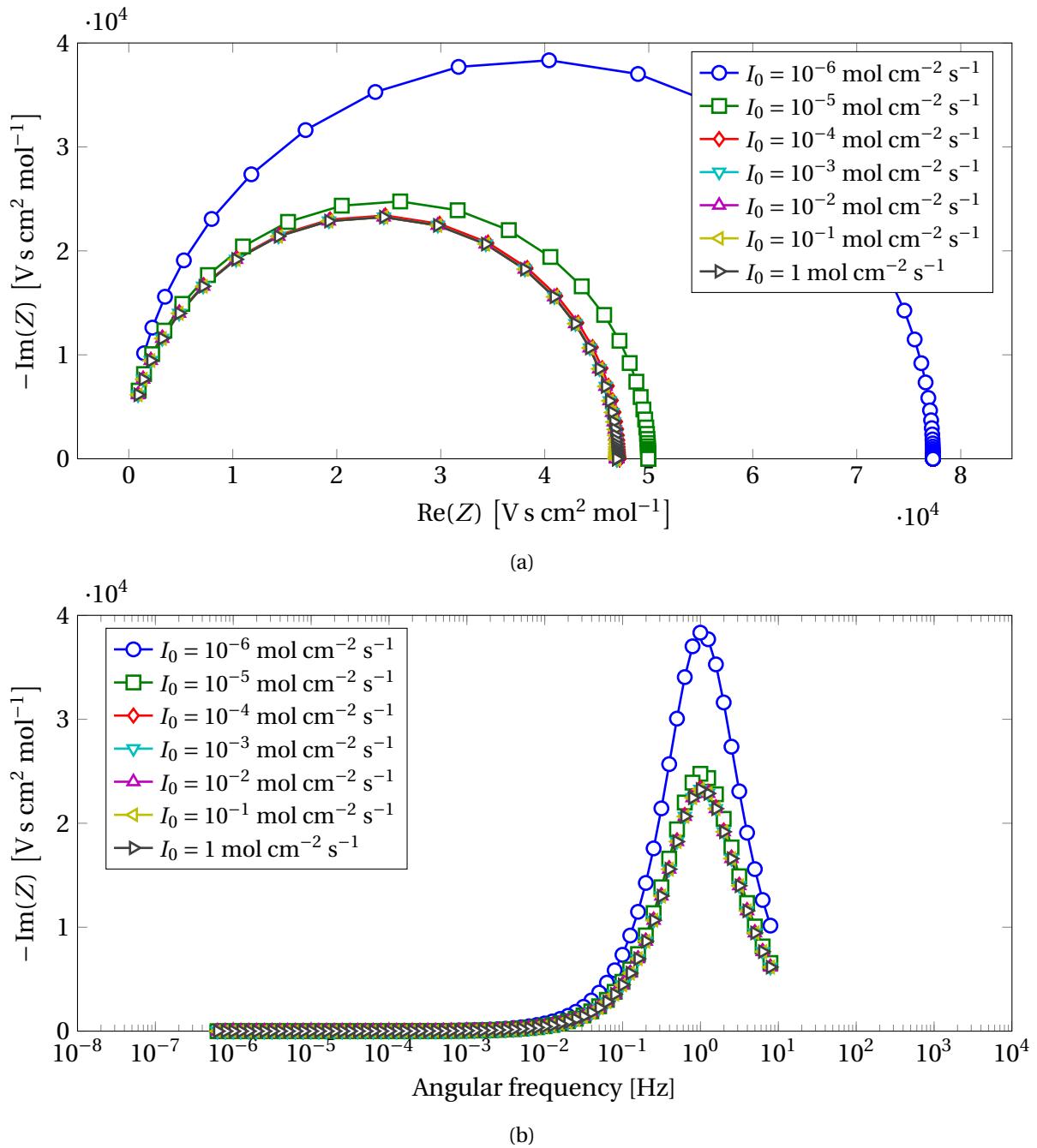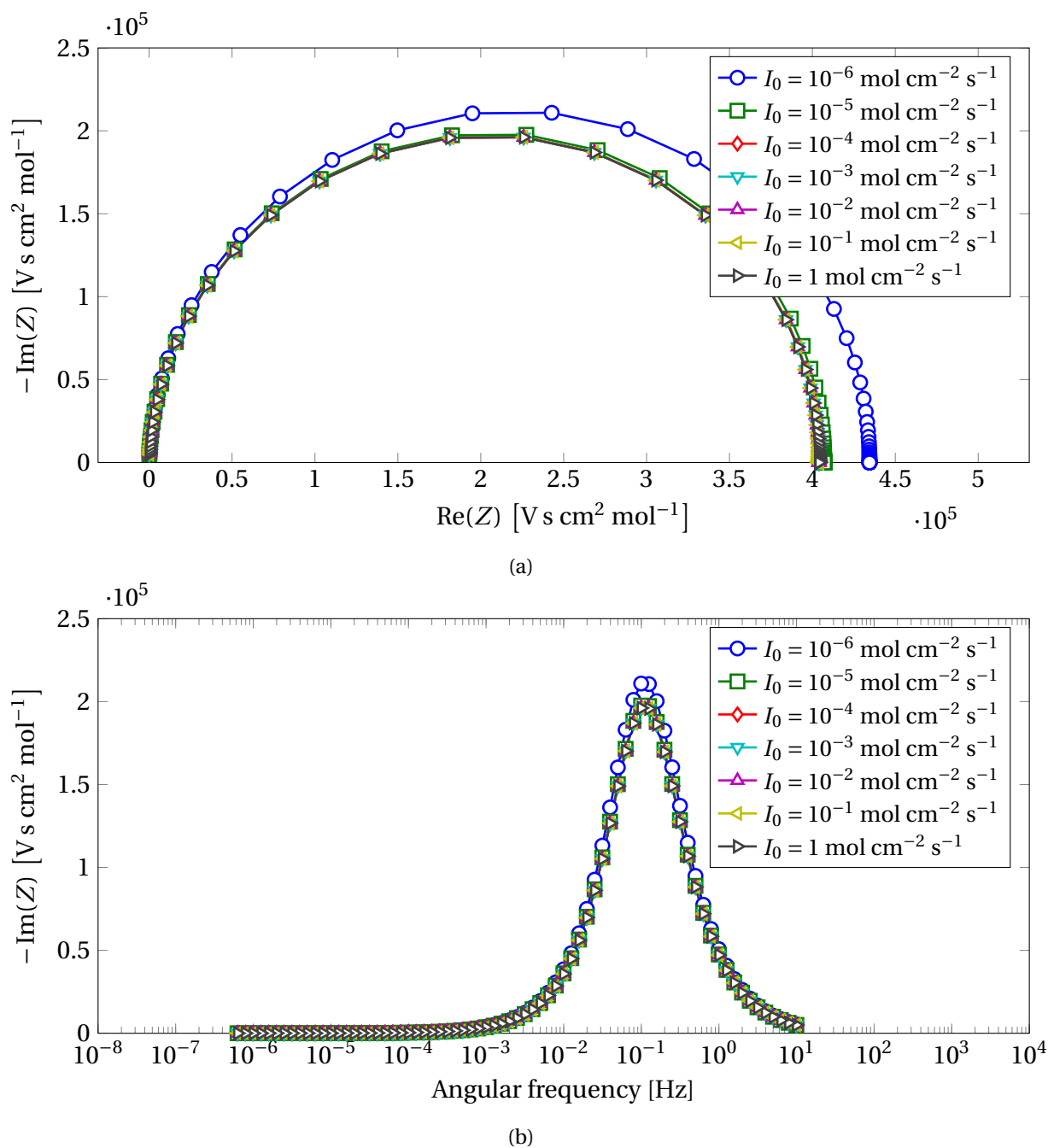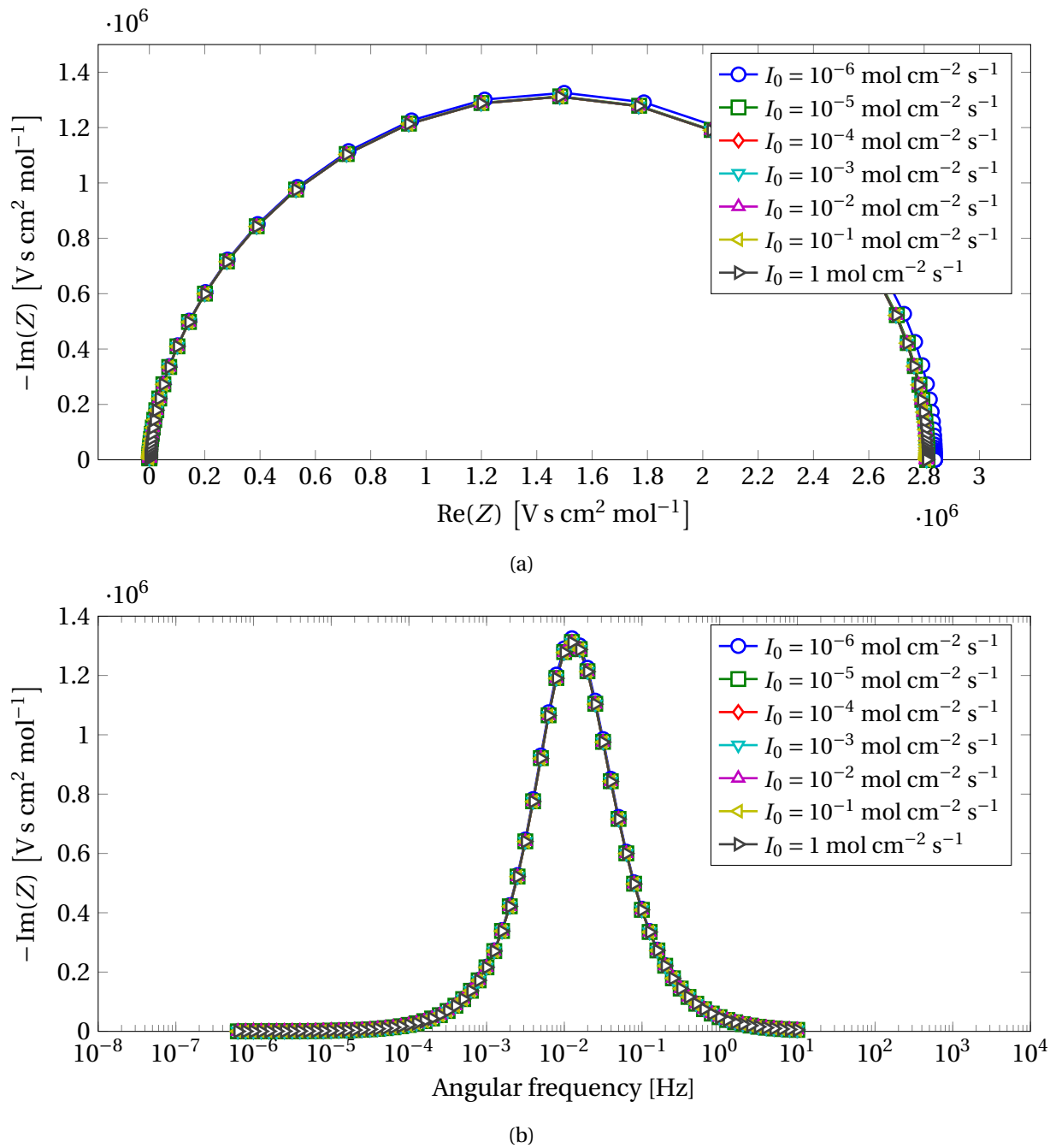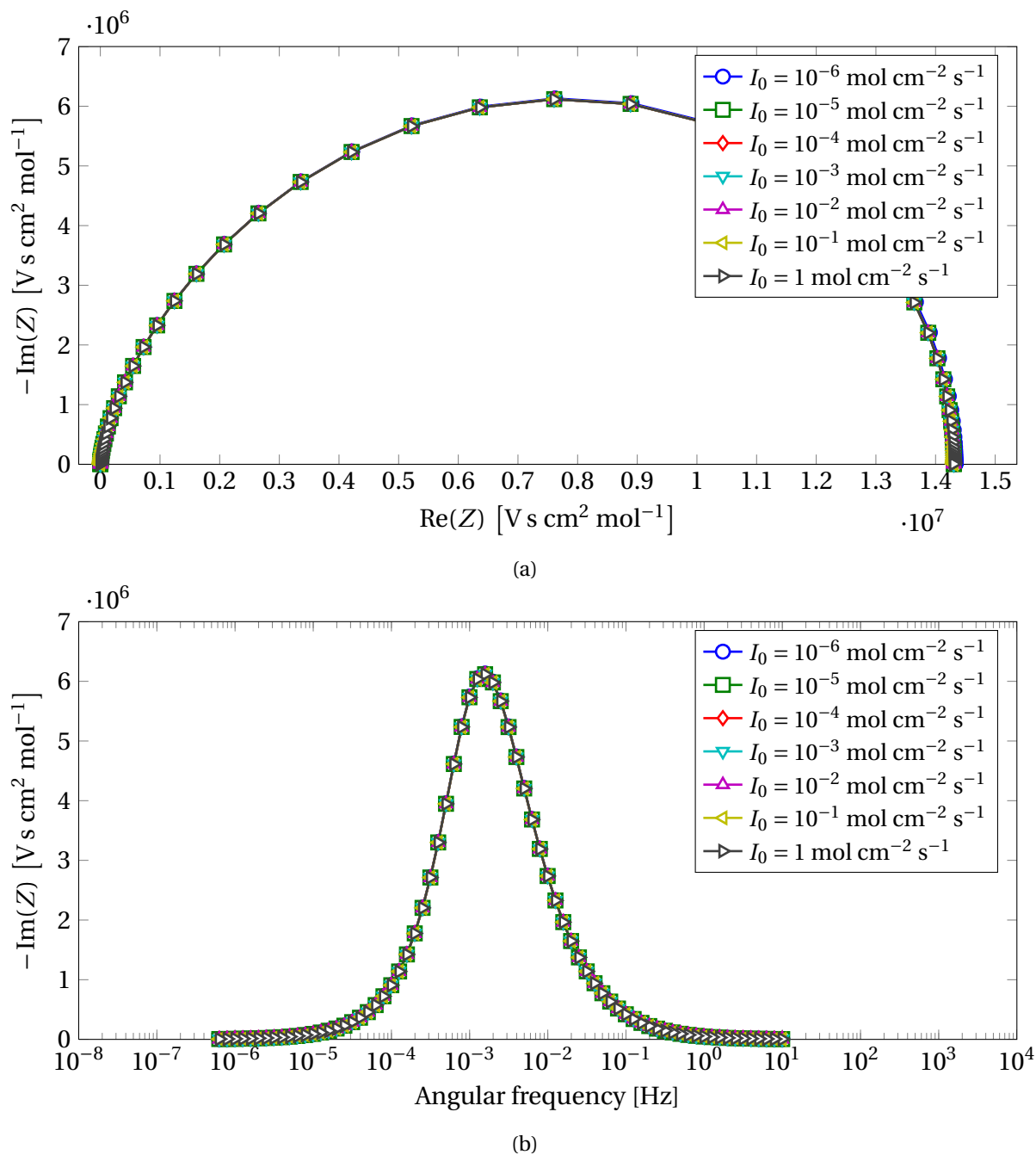
(a)



(b)

Figure 4.14: a Impedance plane plot for the IMVS spectrum from Eq. (3.84) for a photoelectrochemical system described in Section 4.2. Calculations are done for an effective rate constant $k = 1$ s$^{-1}$ and a frequency region $10^{-7}$–$10^3$ Hz. b Corresponding bode plot of the imaginary part of the impedance as a function of angular frequency.
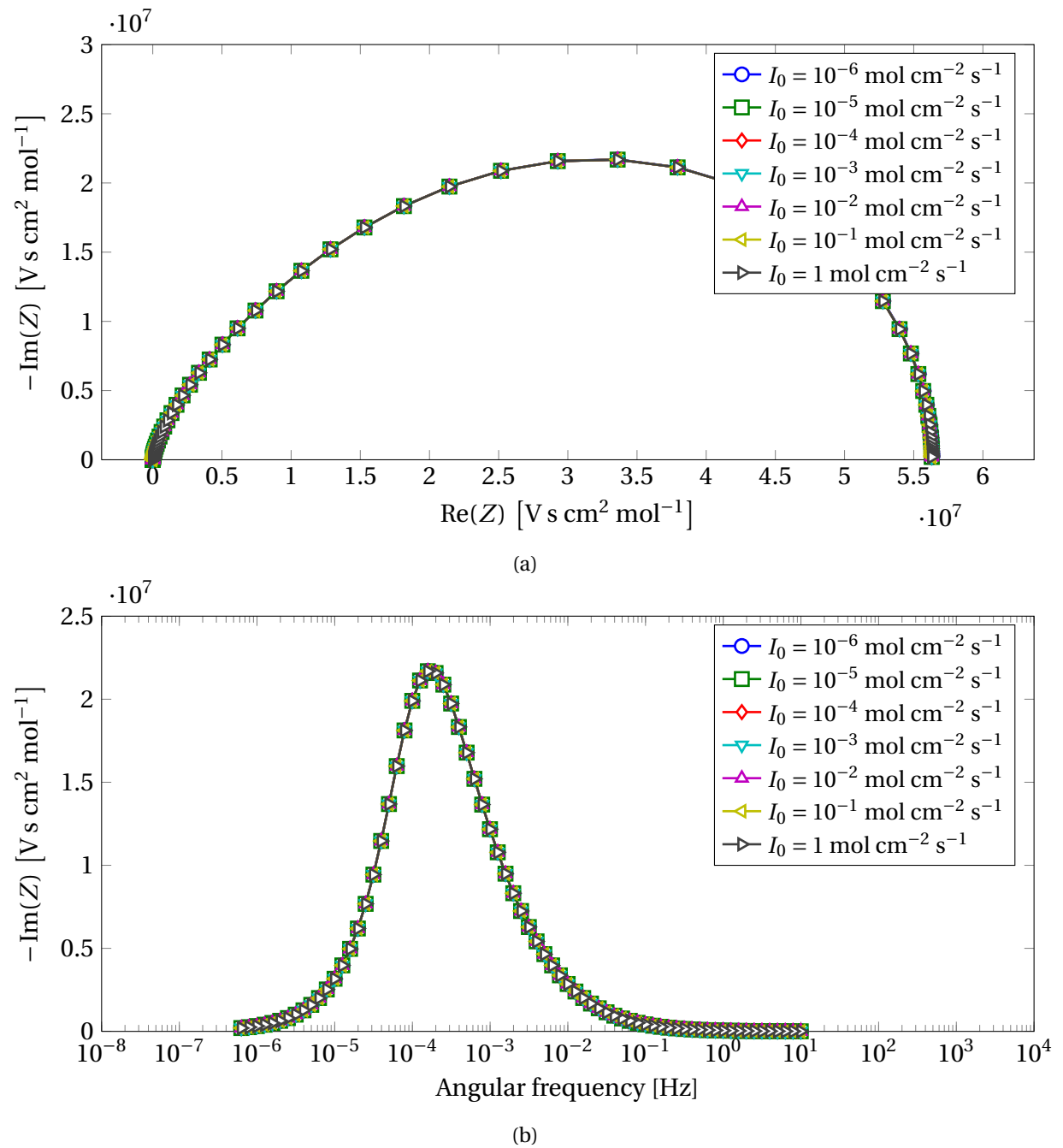
(a)



(b)

Figure 4.15: a Impedance plane plot for the IMVS spectrum from Eq. (3.84) for a photoelectrochemical system described in Section 4.2. Calculations are done for an effective rate constant $k = 10^{-1}$ s$^{-1}$ and a frequency region $10^{-7}$–$10^{3}$ Hz. b Corresponding bode plot of the imaginary part of the impedance as a function of angular frequency.

(a)



(b)

Figure 4.16: a Impedance plane plot for the IMVS spectrum from Eq. (3.84) for a photoelectrochemical system described in Section 4.2. Calculations are done for an effective rate constant $k = 10^{-2}$ s$^{-1}$ and a frequency region $10^{-7}$–$10^3$ Hz. b Corresponding bode plot of the imaginary part of the impedance as a function of angular frequency.

(a)



(b)

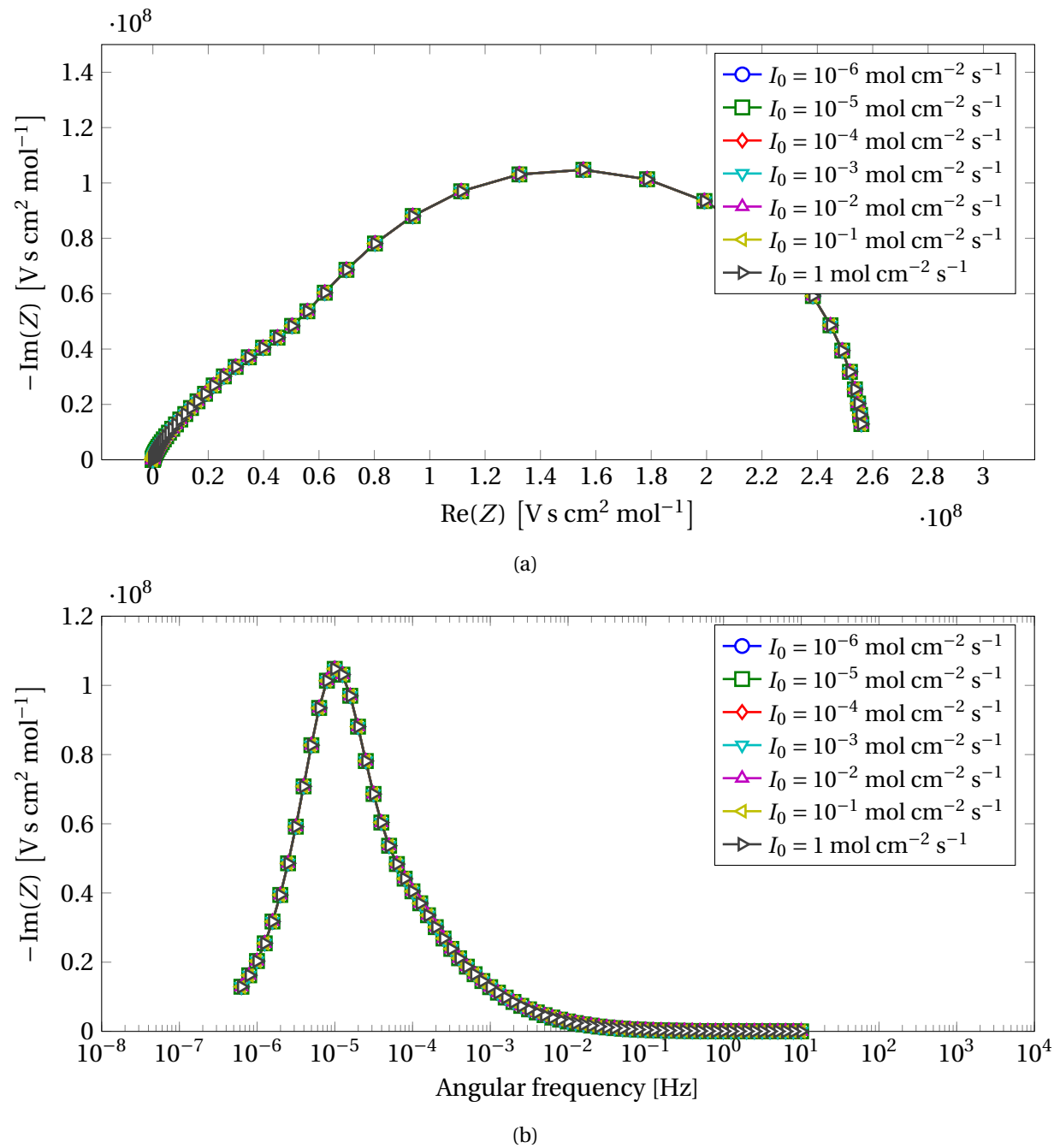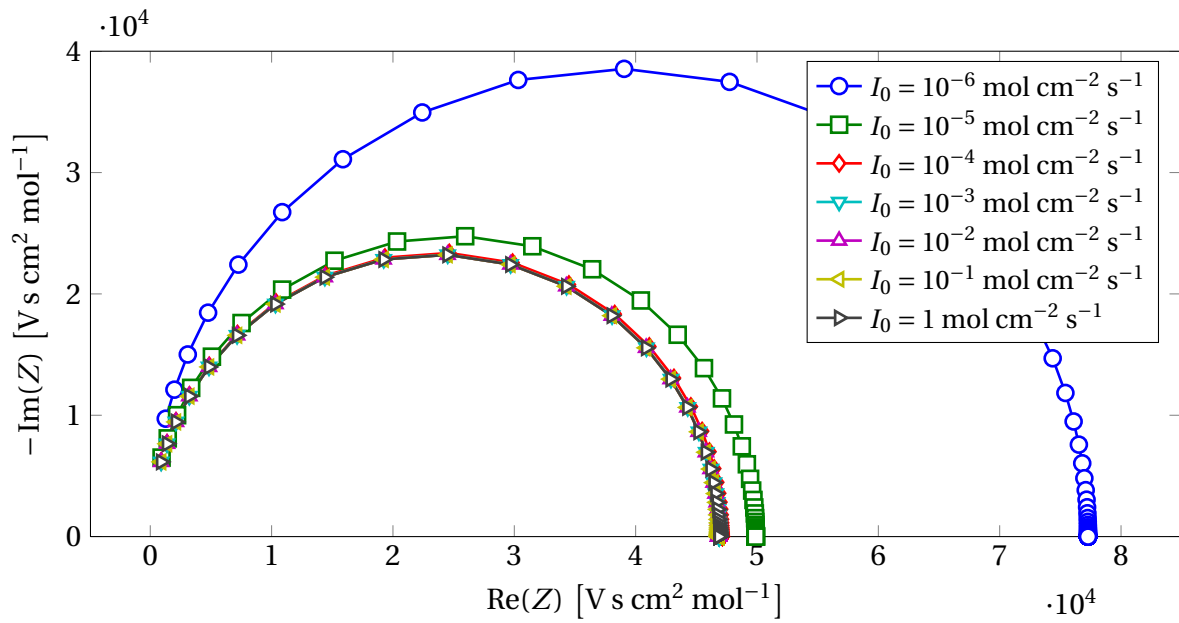Figure 4.17: a Impedance plane plot for the IMVS spectrum from Eq. (3.84) for a photoelectrochemical system described in Section 4.2. Calculations are done for an effective rate constant $k = 10^{-3}$ s$^{-1}$ and a frequency region $10^{-7}$–$10^3$ Hz. b Corresponding bode plot of the imaginary part of the impedance as a function of angular frequency.

(a)



(b)

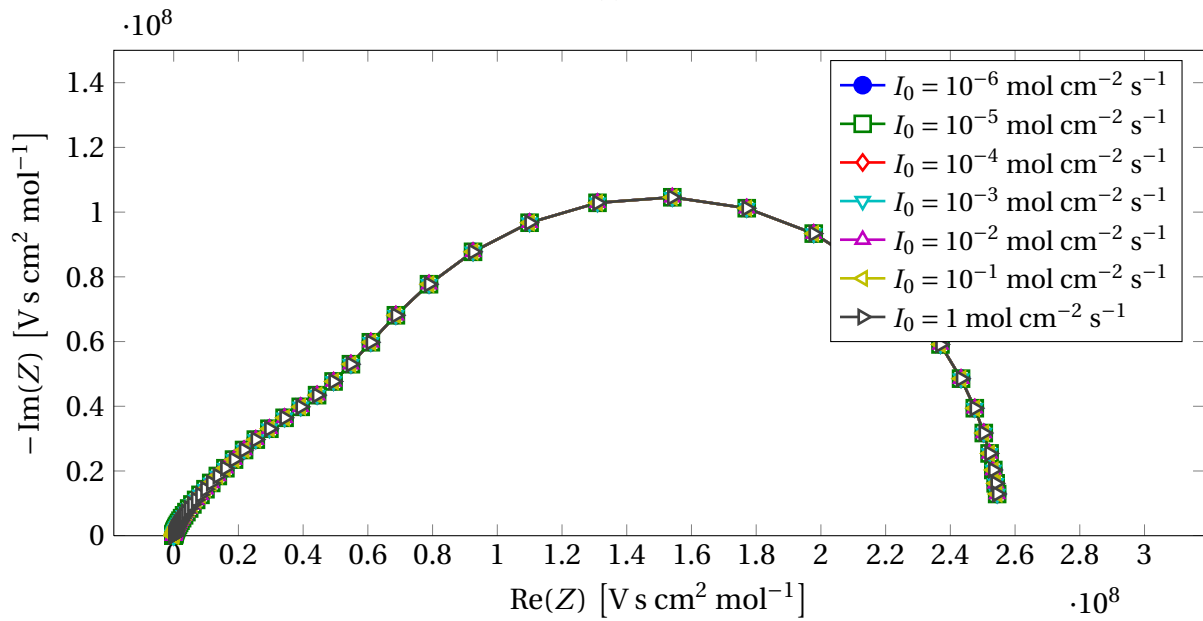Figure 4.18: a Impedance plane plot for the IMVS spectrum from Eq. (3.84) for a photoelectrochemical system described in Section 4.2. Calculations are done for an effective rate constant $k = 10^{-4}$ s$^{-1}$ and a frequency region $10^{-7}$–$10^{3}$ Hz. b Corresponding bode plot of the imaginary part of the impedance as a function of angular frequency.

(a)



(b)

Figure 4.19: a Impedance plane plot for the IMVS spectrum from Eq. (3.84) for a photoelectrochemical system described in Section 4.2. Calculations are done for an effective rate constant $k = 10^{-5}$ s$^{-1}$ and a frequency region $10^{-7}$–$10^3$ Hz. b Corresponding bode plot of the imaginary part of the impedance as a function of angular frequency.

(a)



(b)

Figure 4.20: Impedance plane plot for the IMVS spectrum from Eq. (3.84) for a photoelectrochemical system described in Section 4.2 with equal transport numbers. Calculations are done for a frequency region $10^{-7}$–$10^3$ Hz and an effective rate constant of a $k = 1$ s$^{-1}$, and b $k = 10^{-5}$ s$^{-1}$.

### 4.3.5   Intensity-modulated photocurrent spectroscopy (IMPS)

The the light intensity of the IMPS response for an electrode described in Section 4.2 with an effective rate constant $k = 10^{-1}$ s$^{-1}$ and an applied steady-state current $i_{f,e} = 1$ A cm$^{-2}$ is given in Figure 4.21. Two domes are observed in the impedance plane plot in Figure 4.21a, which indicates to distinct charge transfer processes limiting the system at different frequencies. From the bode plot of the imaginary part of the impedance as a function of the angular frequency, the high frequency dome should correspond to the recombination process described by the effective rate constant $k$. The low frequency dome is assumed to correspond to the charge transfer kinetics at the solution interface. We see that both processes is located in the first quadrant, and the current caused by both processes are oscillating in the same direction as the light intensity modulation.

In figure 4.22 the IMPS response for the same system described in Figure 4.21 is given for an applied faradaic current density $i_{f,e} = 10^{-3}$ A cm$^{-2}$. Here only one dome in the impedance plane plot in Figure 4.22a is observed in the first quadrant for low light intensities, and from the bode plot in Figure 4.21b this should correspond to the recombination process described by the effective rate constant $k$. For high light intensities, we observe a shift in the IMPS response from the first quadrant to the third quadrant. This indicates that the system is limited by a charge limiting process oscillating in the opposite direction as the light intensity. It is assumed to be caused by a back charge transfer process at the solution interface. This back charge transfer process is assumed to have near similar rate constant as the recombination process, to accommodate for the competition between charge generation by the light intensity and recombination in order to keep the potential constant. The rate increases with increasing light intensity, indicating that the back charge transfer process rate increases with increasing light intensity. A distortion in the dome shape is observed in the high frequency region, indicating a diffusion limiting process described by the diffusion coefficient $D$.

In Figure 4.23 the IMPS response for an electrode described in Section 4.2 is calculated with an effective rate constant $k = 10^{-2}$ s$^{-1}$ and an applied steady-state current $i_{f,e} = 1$ A cm$^{-2}$. From the impedance plane plot in Figure 4.23a we observe one dome in the first quadrant for high light intensities. This should correspond to the recombination process described by the effective rate constant $k$, as shown in the bode plot in Figure 4.23b. By increasing the light intensity we observe a shift in quadrant from first to third quadrant, similar to that observed for $k = 10^{-1}$. However, the shift occurs at lower light intensities, which indicates that the recombination process accommodates for the light generation to a less degree in order to keep the potential constant. Thus, a back charge transfer process is assumed to be occurring at higher light intensities to maintain a constant potential.

By decreasing the applied steady-state current to $10^{-3}$ A cm$^{-2}$ as shown in Figure 4.24, the IMPS response is located in the third quadrant in the impedance plane plot given in Figure 4.24a. This is
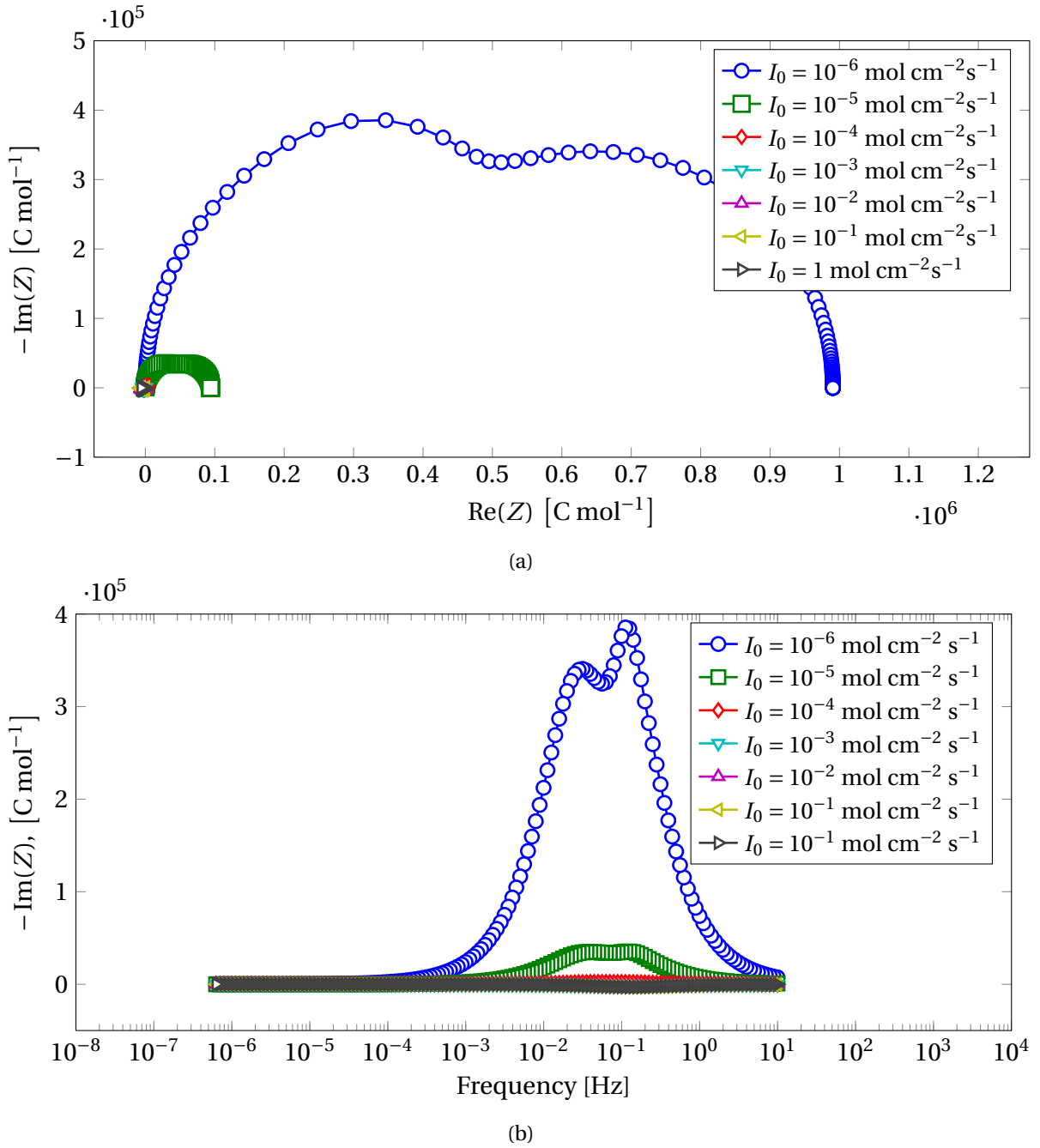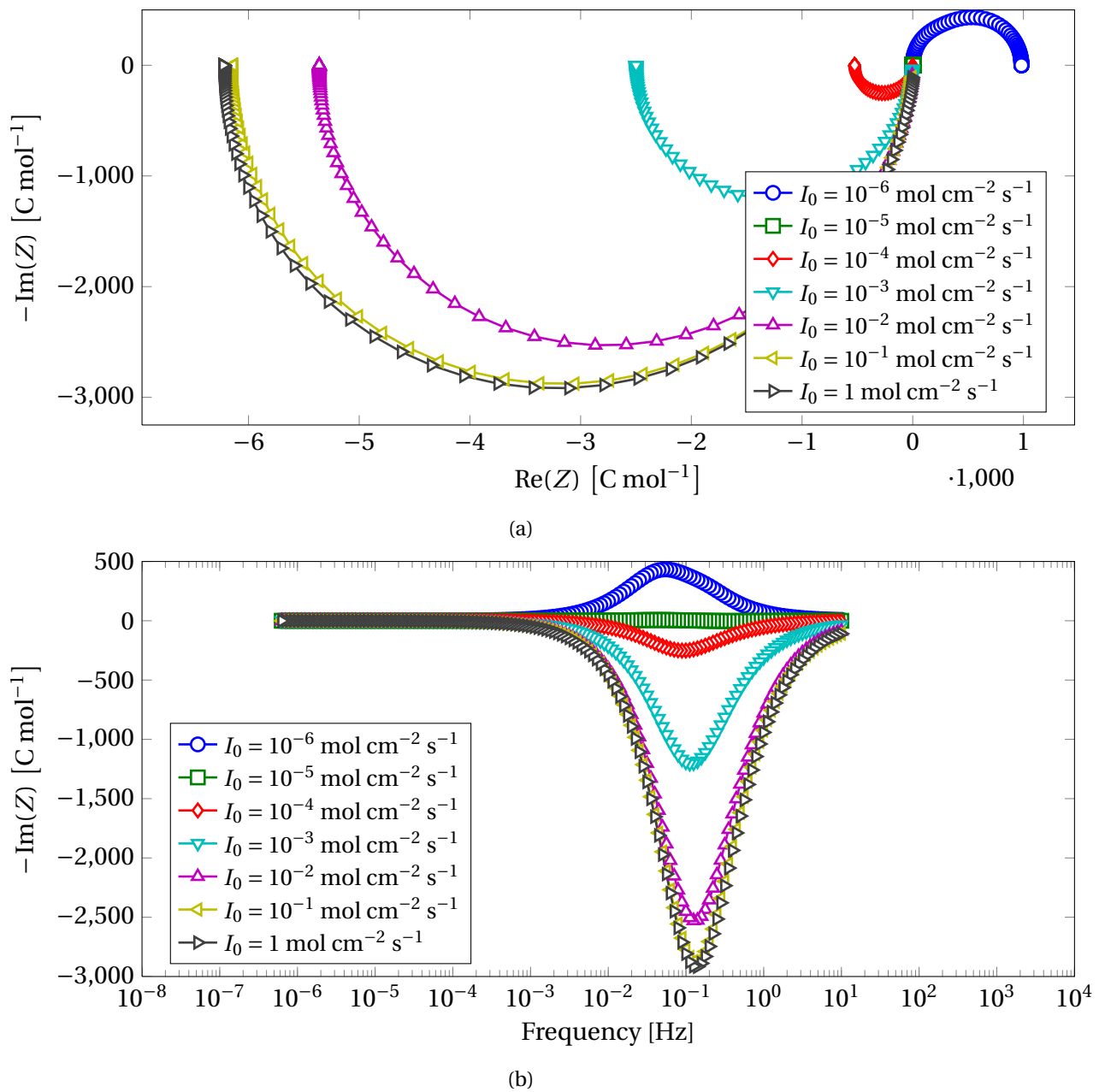
(a)



(b)

Figure 4.21: **a** Light intensity dependency of the impedance plane plot of the IMPS spectrum in Eq. (3.105) for an electrode described in Section 4.2. Calculations are done for an effective rate constant $k = 10^{-1}$ s$^{-1}$, an absorption coefficient $\alpha = 2500$ cm$^{-1}$, incident light intensities in the range of $I_0 = 10^{-6} - 1$ mol cm$^{-2}$ s$^{-1}$, a frequency region of $10^{-7}$–$10^3$ Hz, and an applied steady-state current $i_{f,e} = 1$ A cm$^{-2}$. **b** Corresponding bode plot of the imaginary part of the impedance as a function of angular frequency.
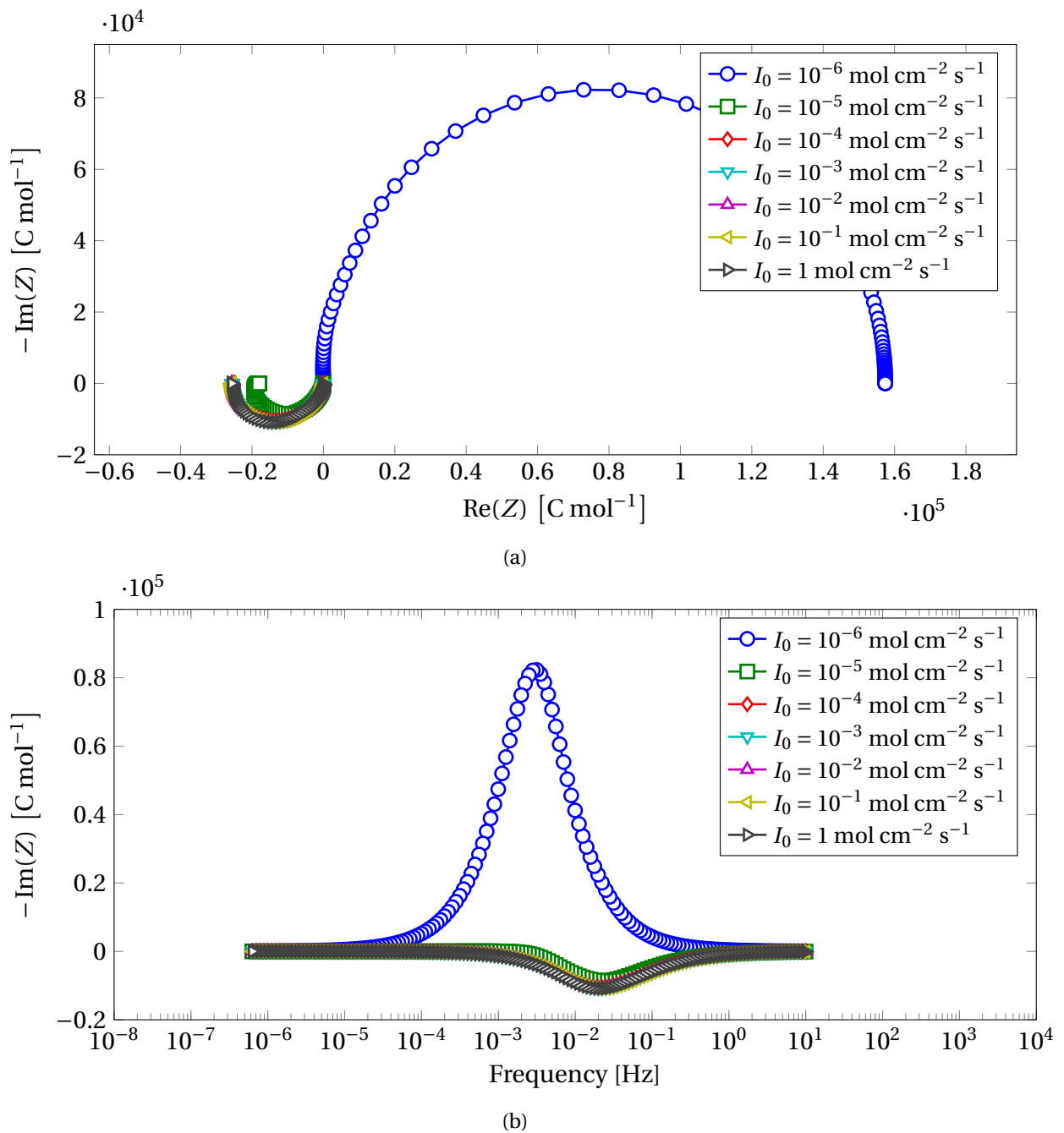
(a)



(b)

Figure 4.22: a Light intensity dependency of the impedance plane plot of the IMPS spectrum in Eq. (3.105) for an electrode described in Section 4.2. Calculations are done for an effective rate constant $k = 10^{-1}$ s$^{-1}$, an absorption coefficient $\alpha = 2500$ cm$^{-1}$, incident light intensities in the range of $I_0 = 10^{-6} - 1$ mol cm$^{-2}$ s$^{-1}$, a frequency region of $10^{-7}$–$10^3$ Hz, and an applied steady-state current $i_{f,e} = 10^{-3}$ A cm$^{-2}$. b Corresponding bode plot of the imaginary part of the impedance as a function of angular frequency.

(a)



(b)

Figure 4.23: a Light intensity dependency of the impedance plane plot of the IMPS spectrum in Eq. (3.105) for an electrode described in Section 4.2. Calculations are done for an effective rate constant $k = 10^{-2}$ s$^{-1}$, an absorption coefficient $\alpha = 2500$ cm$^{-1}$, incident light intensities in the range of $I_0 = 10^{-6} - 1$ mol cm$^{-2}$ s$^{-1}$, a frequency region of $10^{-7}$–$10^3$ Hz, and an applied steady-state current $i_{f,e} = 1$ A cm$^{-2}$. b Corresponding bode plot of the imaginary part of the impedance as a function of angular frequency.

expected from the results for $k = 10^{-1}$ in Figure 4.21 and 4.22, where the reduction of the faradaic current results in a change in the quadrant. The bode plot in Figure 4.24b indicates, as predicted from earlier results, that the dome corresponds to a charge transfer process corresponding to the back charge transfer process. Again, a slight increase in the rate as a function of light intensity is observed.

In Figure 4.25, the IMPS response for the same system as above is plotted for an effective rate constant $k = 10^{-3}$ s$^{-1}$, and $i_{f,e} = 1$ A cm$^{-2}$ in Figure 4.25a and $i_{f,e} = 10^{-3}$ A cm$^{-2}$ in Figure 4.25b. The impedance spectrum occurs in the third quadrant for all light intensities in the impedance plane plots. No apparent light intensity and faradaic current density dependency of the IMPS response is observed.

The corresponding bode plots of the imaginary part of the impedance as a function of angular frequency for Figure 4.25 is given in Figure 4.26. From this plot, we see that the charge transfer limiting process has a rate constant of approximately $10^{-2}$ s$^{-1}$. We assume that this rate corresponds the electrode kinetics at the solution interface.

From these results, we observe that the rate of the assumed back charge transfer process in general increases with increasing light intensity and decreases with decreasing applied steady-state current. In Figure 4.27a the impedance plane plot for a system defined in Section 4.2 with an effective rate constant $k = 10^{-1}$ s$^{-1}$, an applied faradaic current density $i_{f,e} = 1$ A cm$^{-2}$, and equal transport numbers are given. Compared to Figure 4.21a, only one dome is occurring. This dome corresponds to the charge recombination process described by the effective rate constant $k$, as seen from the bode plot in Figure 4.27b. The same shift in quadrant by increasing the light intensity is observed. We also observe a reduction in the magnitude of the impedance by changing the transport number to equal values.

By reducing the applied faradaic current density to $i_{f,e} = 10^{-3}$ A cm$^{-2}$, the impedance plane plot in Figure 4.28 shows one dome in the third quadrant for all light intensities with a rate equal to the charge recombination rate $k$.

In Figure 4.29, the impedance plane plot for $k = 10^{-2}$ and $i_{f,e} = 1$ A cm$^{-2}$ is calculated for equal transport numbers. Compared to the calculations done for one transport number equal to unity in Figure 4.23a, the shift towards the third quadrant is occurring to a larger degree for low light intensities when the transport numbers are set equal.

The by reducing the applied faradaic current density or rate constant further when assuming equal transport numbers, similar trends as for one transport number equal to unity as described above is observed. In general, the magnitude of IMPS impedance reduces when setting the transport numbers equal by the means described above.
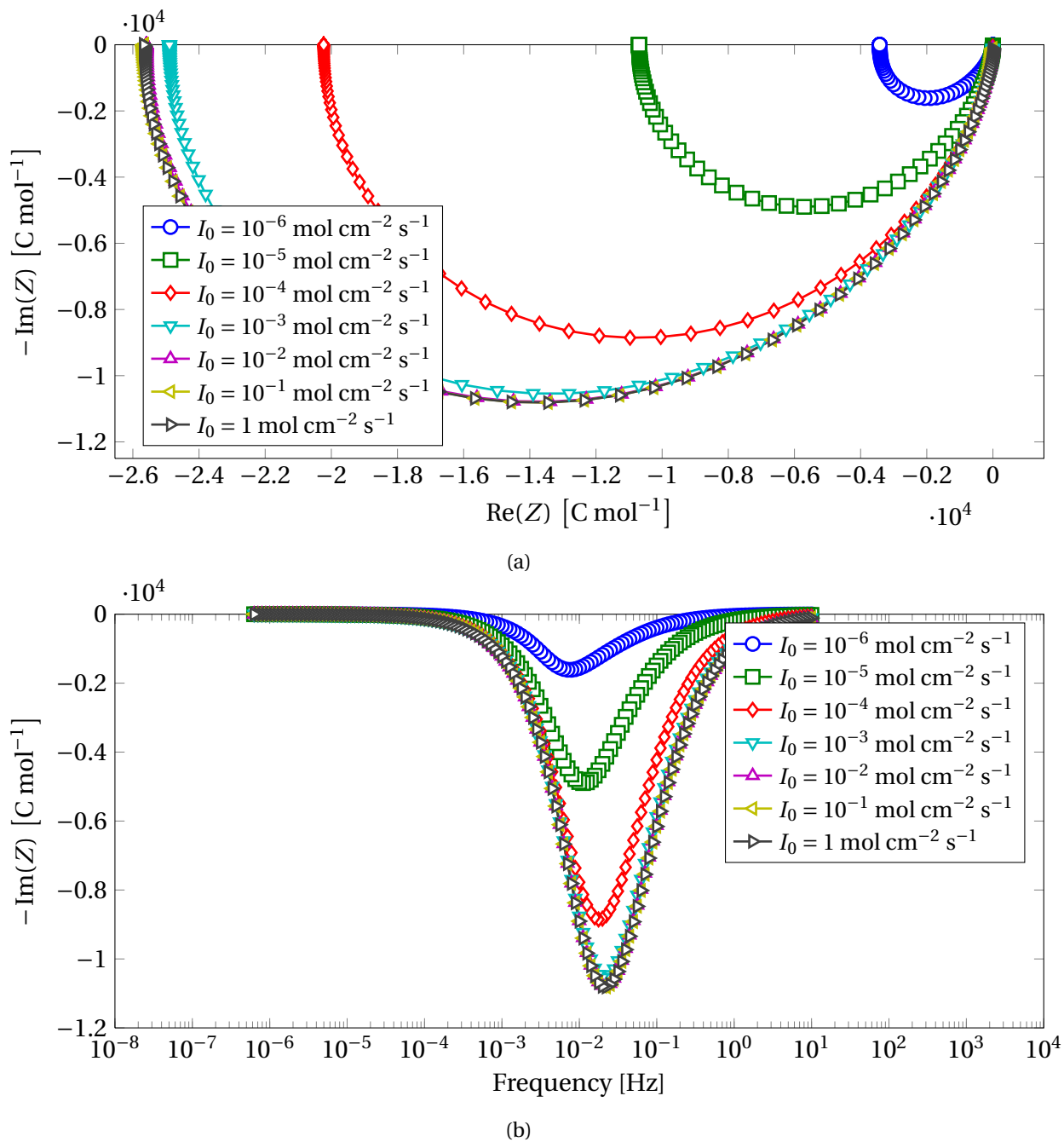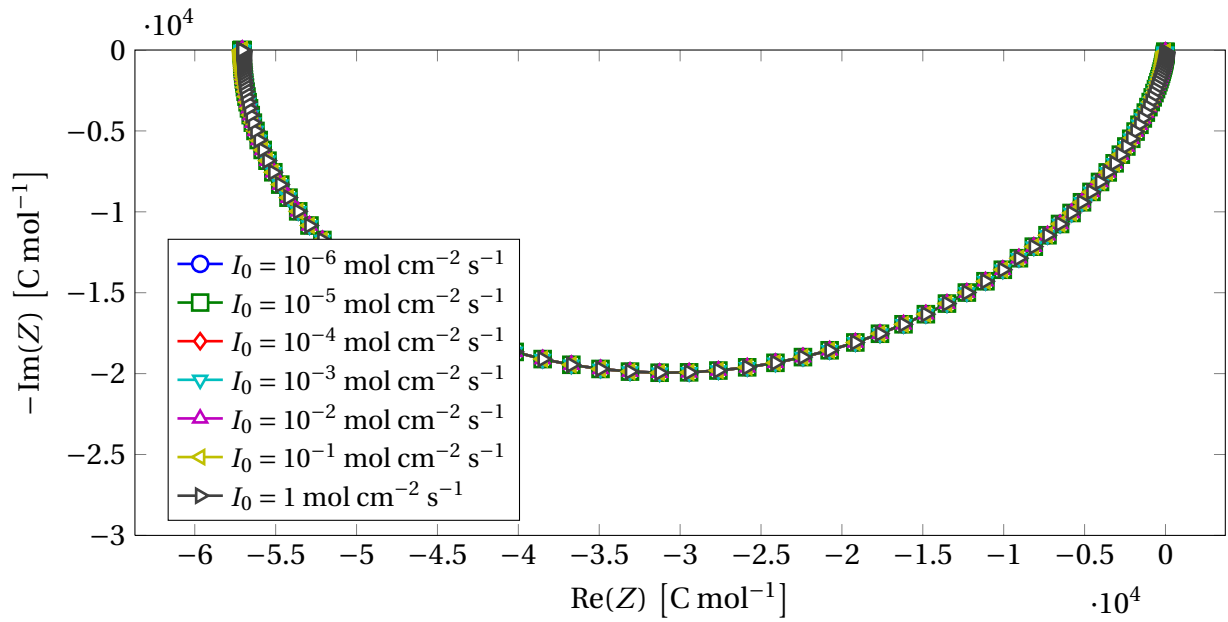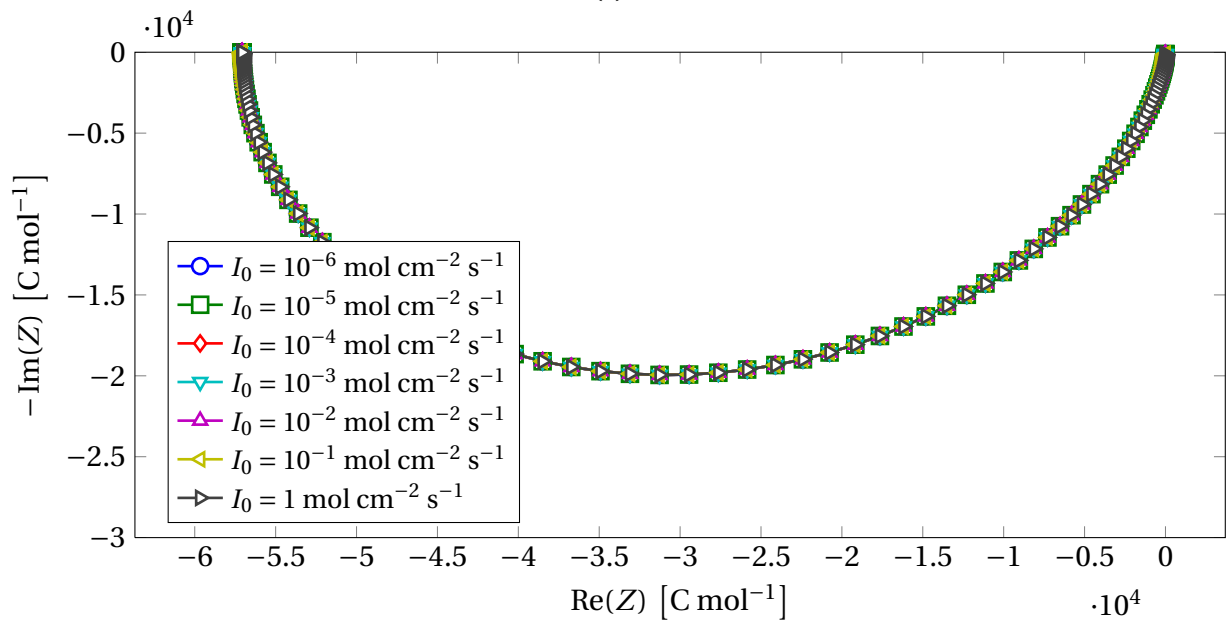
(a)



(b)

Figure 4.24: a Light intensity dependency of the impedance plane plot of the IMPS spectrum in Eq. (3.105) for an electrode described in Section 4.2. Calculations are done for an effective rate constant $k = 10^{-2}$ s$^{-1}$, an absorption coefficient $\alpha = 2500$ cm$^{-1}$, incident light intensities in the range of $I_0 = 10^{-6} - 1$ mol cm$^{-2}$ s$^{-1}$, a frequency region of $10^{-7}-10^3$ Hz, and an applied steady-state current $i_{f,e} = 10^{-3}$ A cm$^{-2}$. b Corresponding bode plot of the imaginary part of the impedance as a function of angular frequency.

(a)



(b)

Figure 4.25: Light intensity dependency of the impedance plane plot of the IMPS spectrum in Eq. (3.105) for an electrode described in Section 4.2. Calculations are done for an effective rate constant $k = 10^{-3}$ s$^{-1}$, an absorption coefficient $\alpha = 2500$ cm$^{-1}$, incident light intensities in the range of $I_0 = 10^{-6} - 1$ mol cm$^{-2}$ s$^{-1}$, a frequency region of $10^{-7} - 10^3$ Hz, and an applied steady-state current a $i_{f,e} = 1$ A cm$^{-2}$ and b $i_{f,e} = 10^{-3}$ A cm$^{-2}$.
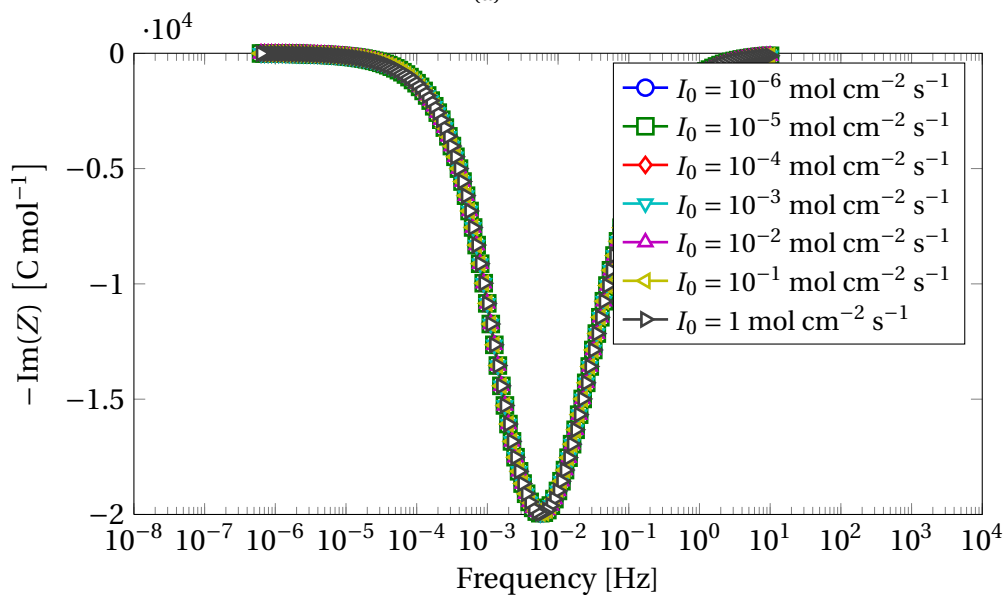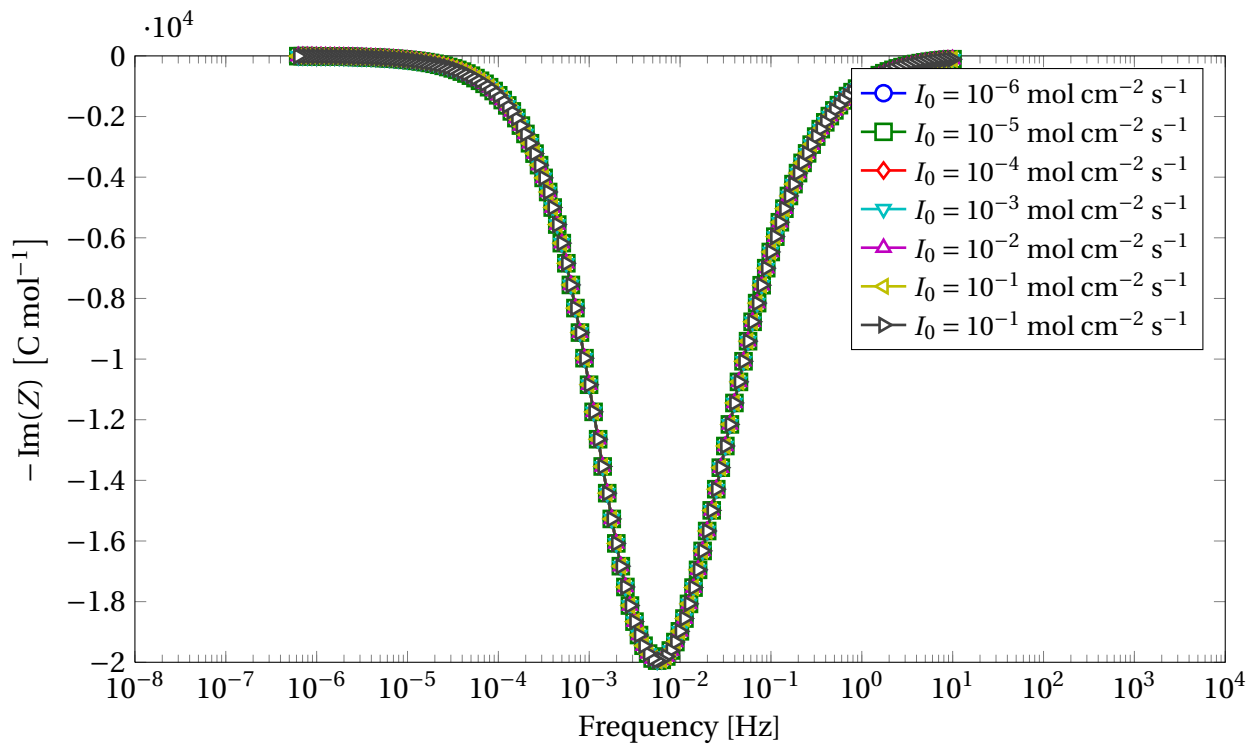
(a)



(b)

Figure 4.26: Light intensity dependency of the bode plot of the IMPS spectrum in Eq. (3.105) for an electrode described in Section 4.2. Calculations are done for an effective rate constant $k = 10^{-3}$ s$^{-1}$, an absorption coefficient $\alpha = 2500$ cm$^{-1}$, incident light intensities in the range of $I_0 = 10^{-6} - 1$ mol cm$^{-2}$ s$^{-1}$, a frequency region of $10^{-7}$–$10^3$ Hz, and an applied steady-state current a $i_{f,e} = 1$ A cm$^{-2}$ and b $i_{f,e} = 10^{-3}$ A cm$^{-2}$.
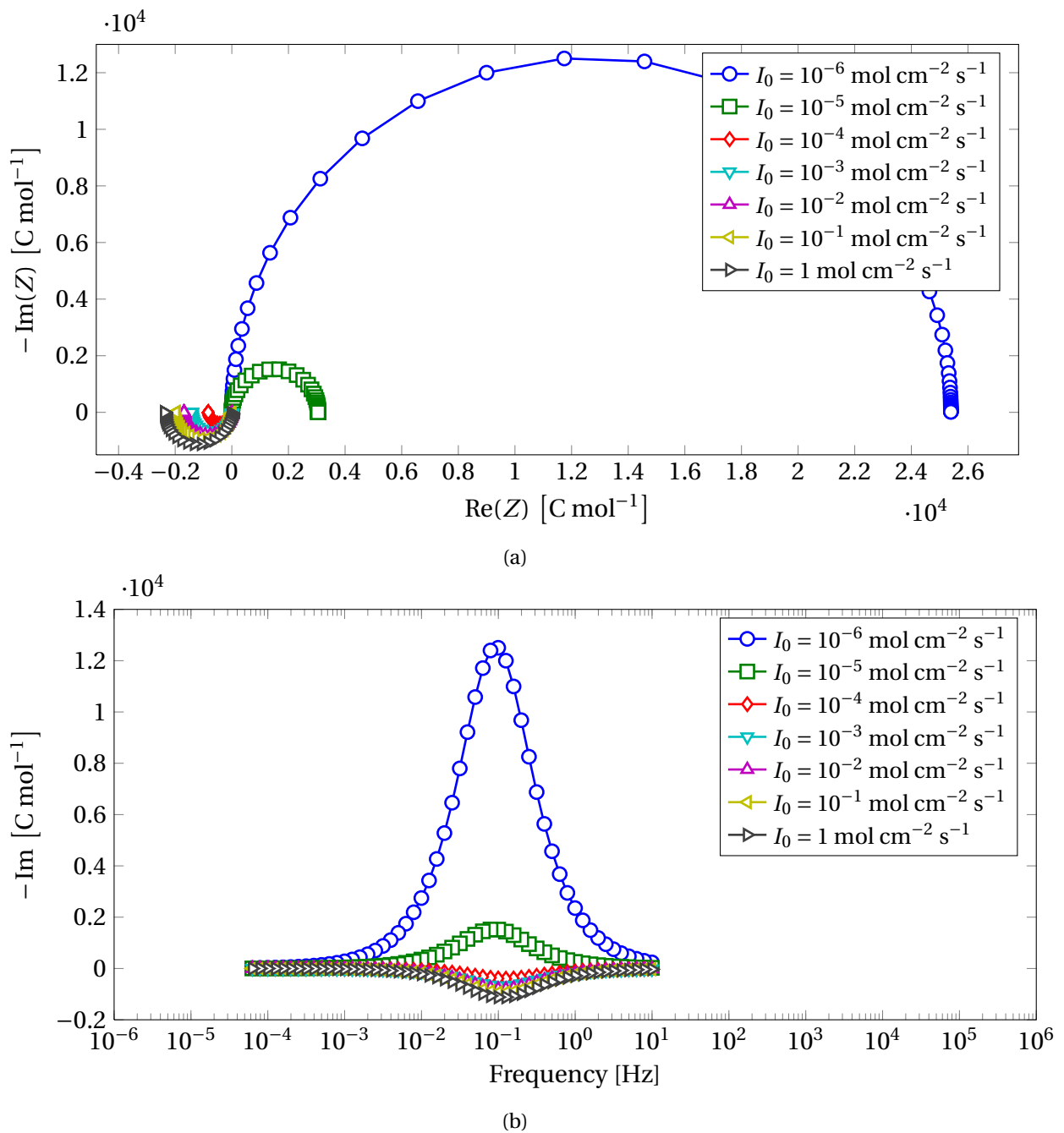
(a)



(b)

Figure 4.27: a Light intensity dependency of the impedance plane plot of the IMPS spectrum in Eq. (3.105) for an electrode described in Section 4.2 with equal transport numbers. Calculations are done for an effective rate constant $k = 10^{-1}$ s$^{-1}$, an absorption coefficient $\alpha = 2500$ cm$^{-1}$, incident light intensities in the range of $I_0 = 10^{-6} - 1$ mol cm$^{-2}$ s$^{-1}$, a frequency region of $10^{-7}$–$10^3$ Hz, and an applied steady-state current $i_{f,e} = 1$ A cm$^{-2}$. b Corresponding bode plot of the imaginary part of the impedance as a function of angular frequency.

Figure 4.28: Impedance plane plot of the IMPS spectrum in Eq. (3.105) for an electrode described in Section 4.2 with equal transport numbers, $k = 10^{-1}$ s$^{-1}$, and $i_{f,e} = 10^{-3}$ A cm$^{-2}$.
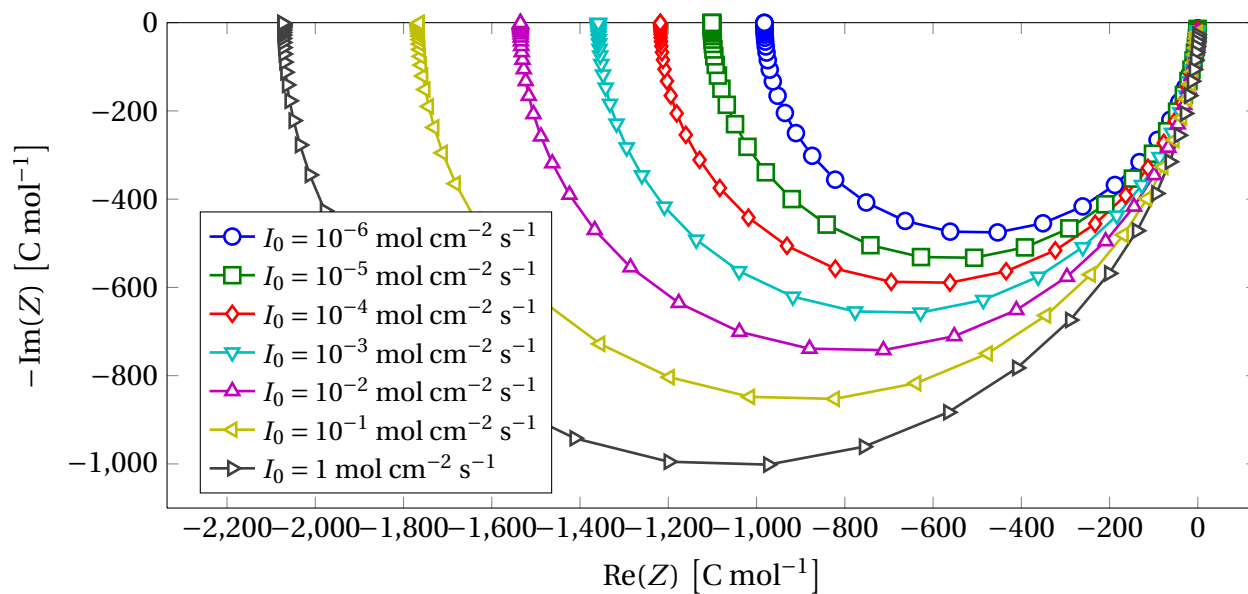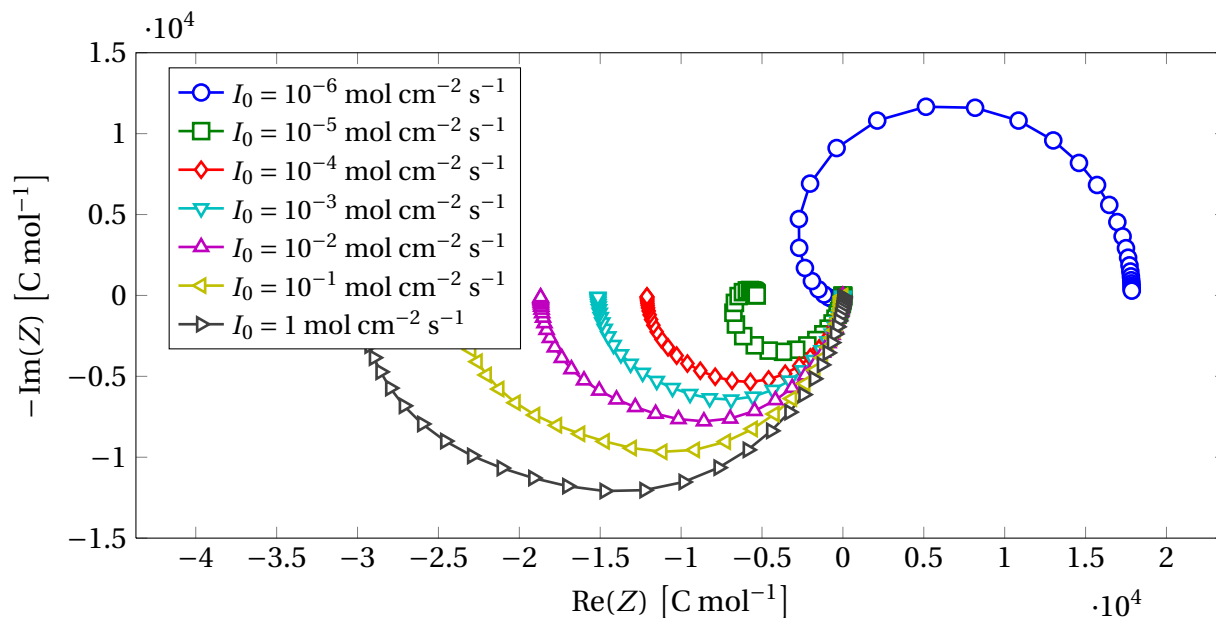


Figure 4.29: Impedance plane plot of the IMPS spectrum in Eq. (3.105) for an electrode described in Section 4.2 with equal transport numbers, $k = 10^{-2}$ s$^{-1}$, and $i_{f,e} = 1$ A cm$^{-2}$.

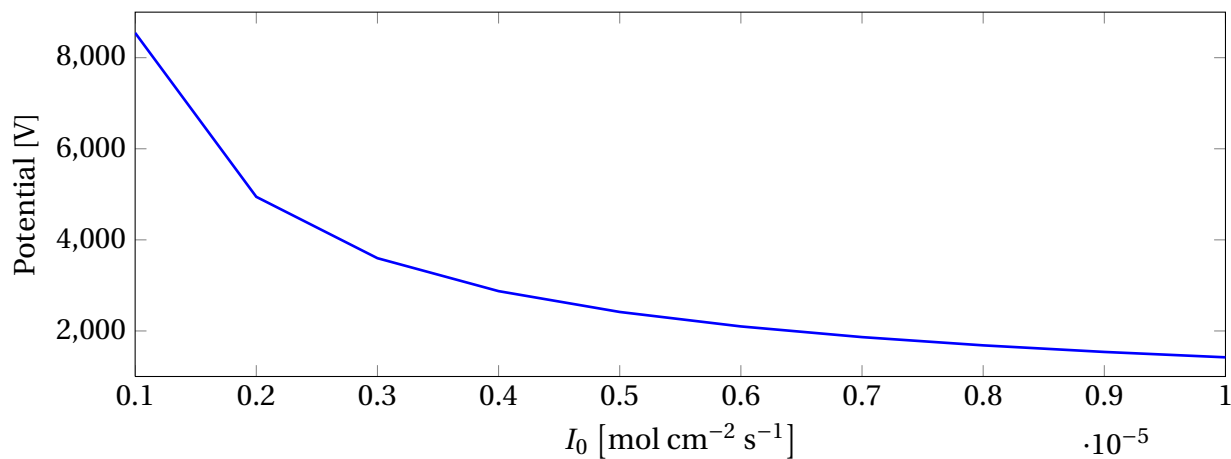### 4.3.6   Steady-state potential as a function of light intensity under constant faradaic current density

The potential in Eq. (3.142) with a constant faradaic current density $i_{f,e}$ as a function of light intensity for three rate constants $k = 10^{-1}$, $k = 10^{-2}$, and $k = 10^{-3}$ s$^{-1}$ are given in Figure 4.30 for light intensities between $10^{-6}$ and $10^{-5}$ mol cm$^{-2}$ s$^{-1}$. We have assumed $\mu^0 = 0$ for simplicity. For $k = 10^{-1}$ s$^{-1}$ we observe a decrease in the measured potential with increasing light intensity, as shown in Figure 4.30a. For $k = 10^{-2}$ s$^{-1}$ we observe a decrease of the measured electrochemical potential with increasing the light intensity for low values of $I_0$, reaching a minimum value around $4 \times 10^{-5}$ mol cm$^{-2}$ s$^{-1}$. However, by further increasing the light intensity, the measured potential increases with increasing light intensity. This is shown in Figure 4.30b. For $k = 10^{-3}$ s$^{-1}$ we observe an increase in the measured potential with increasing light intensity, as shown in Figure 4.30c. From these results, we observe that for the electrode system the potential as a function of constant faradaic current density initially decreases with increasing light intensity until a minimum is reached at a threshold value of $I_0$. At this point, the potential increases with increasing light intensity. The threshold value of $I_0$ decreases with decreasing $k$-value, as shown in Figure 4.30 where the minimum of $I_0$ for $k = 10^{-1}$ s$^{-1}$ is located for higher $I_0$ values than the chosen light intensity range, the minimum of $I_0$ for $k = 10^{-2}$ s$^{-1}$ is located within the chosen light intensity region, and the minimum of $I_0$ for $k = 10^{-3}$ s$^{-1}$ is located for lower $I_0$ values than the chosen light intensity range.

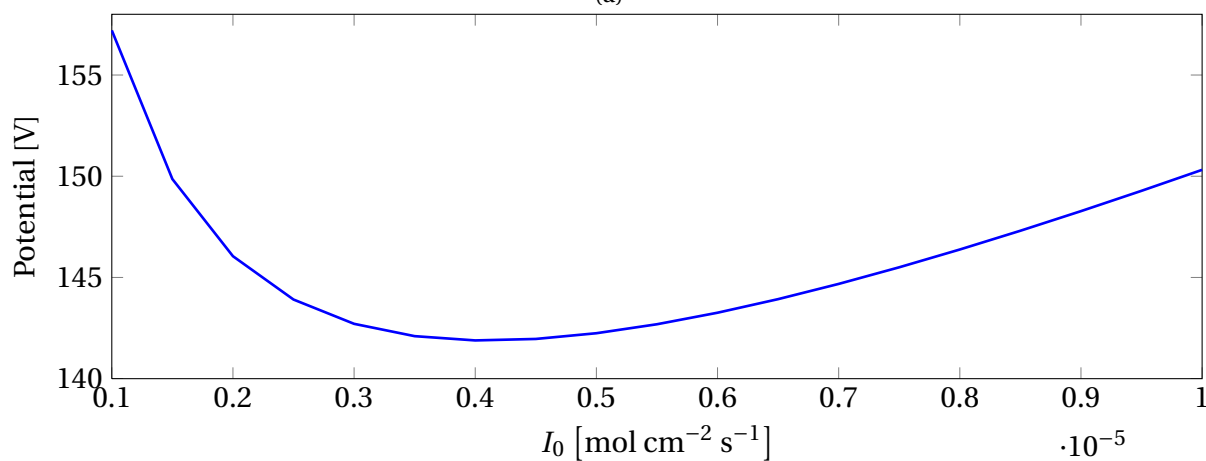### 4.4   Microporous thin film electrode

In Figure 4.31 the rate constant dependency of the IMPS transfer function for a microporous electrode described in Section 4.2 is given for rate constants between $k = 10^{-2}$ and $k = 1$ s$^{-1}$.

The impedance plane plots in Figure 4.31a show a dome shape corresponding to a charge transfer limiting process in the low frequency region, and a straight line corresponding to a diffusion limiting process in the high frequency region. From the bode plots in Figure 4.31b the dome occurring in the impedance spectrum correspond to the recombination rate described by the effective rate constant $k$. The shape of the impedance plane plot is similar to a reflective-like behavior impedance spectrum.

In Figure 4.32 the IMPS response is calculated for the same system described above with an effective rate constant $k = 10^{-3}$ s$^{-1}$. We observe a "snail house" behavior in the impedance plane plot in Figure 4.32a with three distinct rate constants as shown in the bode plot in Figure 4.32b. This indicates that the system is either described by three charge transfer limiting processes occurring at different frequencies, or most likely that the model is breaking down numerically. A more detailed study of this model is required, and will not be investigated further in this study.

(a)



(b)
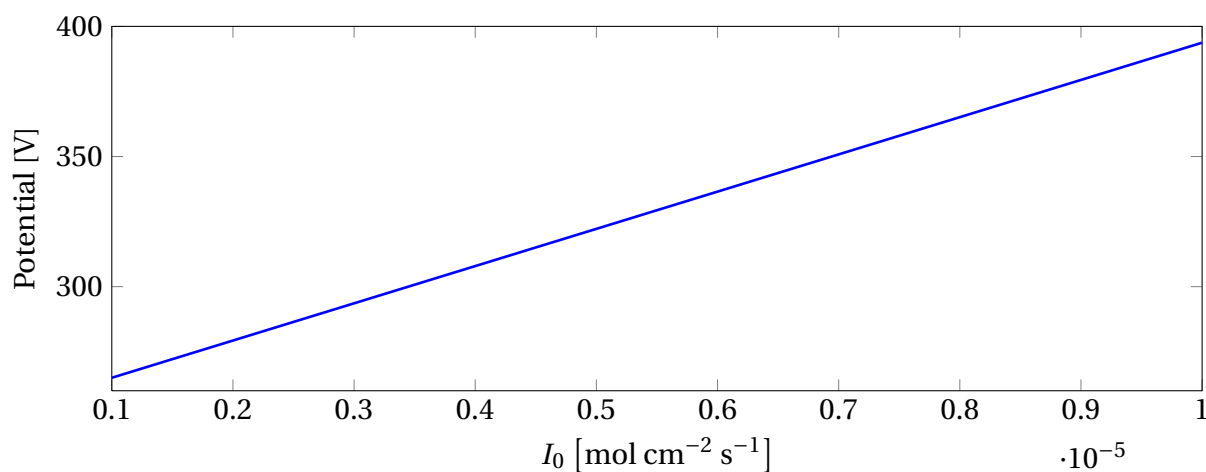


(c)

Figure 4.30: Measured electrochemical potential as a function of light intensity for a rate constant a $k = 10^{-1}$ s$^{-1}$, b $k = 10^{-2}$ s$^{-1}$, and c $k = 10^{-3}$ s$^{-1}$. Calculated for a constant faradaic current density $i_{f,e} = 1$ A cm$^{-2}$, $\alpha = 2500$ cm$^{-1}$, and for light intensities in the range of $10^{-6}$ to $10^{-5}$ mol cm$^{-2}$ s$^{-1}$.

(a)



(b)

Figure 4.31: a Impedance plane plot of the rate constant dependency for the IMPS spectrum from Eq. (3.150) for a microporous thin film electrode described in Section 4.2. b Corresponding bode plot of the imaginary part of the impedance spectra as a function of angular frequency. Calculations are done for a frequency region of $10^{-5}$–$10^{6}$ Hz.

(a)



(b)
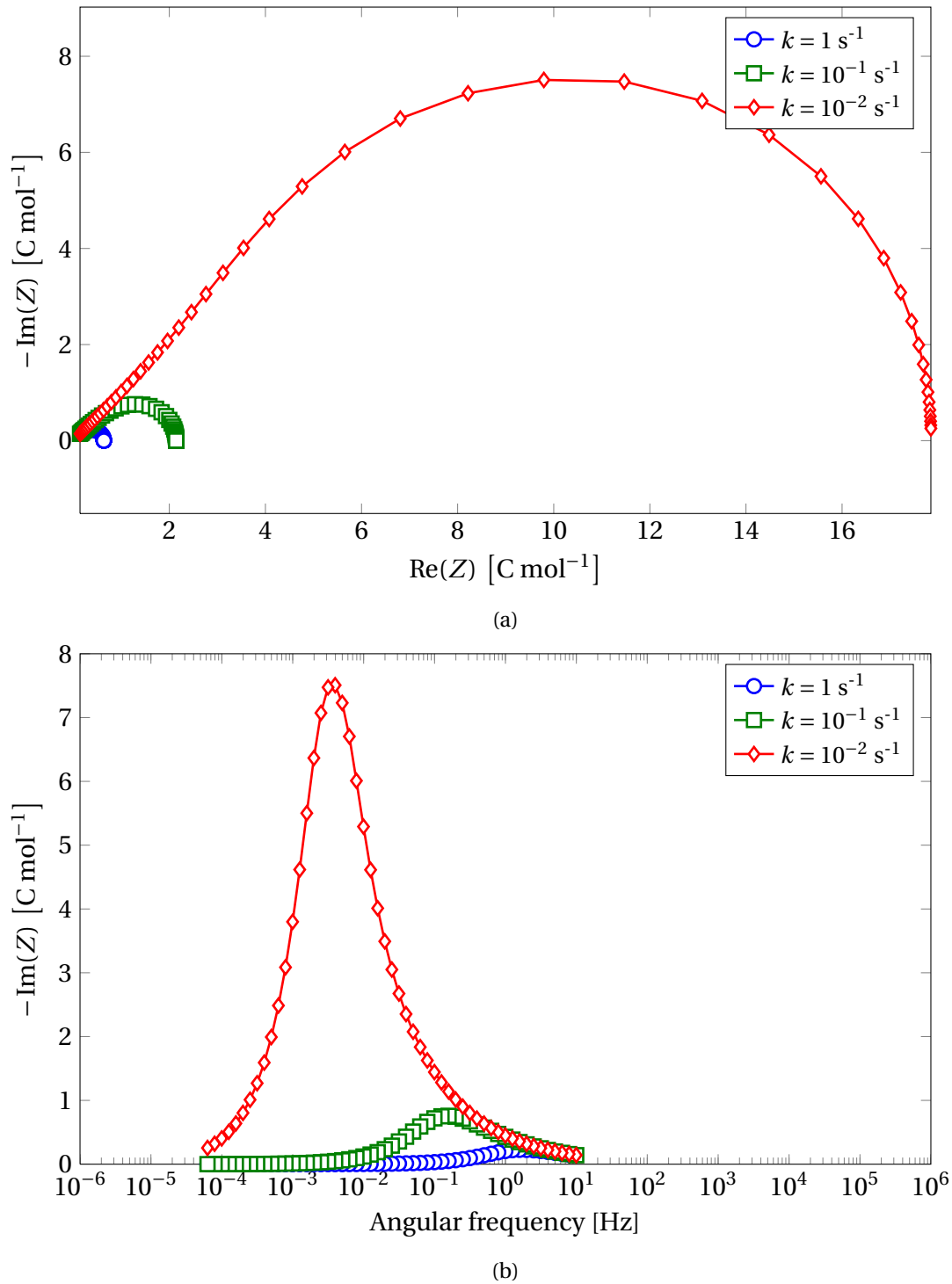
Figure 4.32: a Impedance plane plot for the IMPS spectrum from Eq. (3.150) for a microporous thin film electrode described in Section 4.2 with an effective rate constant $k = 10^{-3}$ s$^{-1}$. b Corresponding bode plot of the imaginary part of the impedance spectra as a function of angular frequency. Calculations are done for a frequency region of $10^{-5}$–$10^{6}$ Hz.
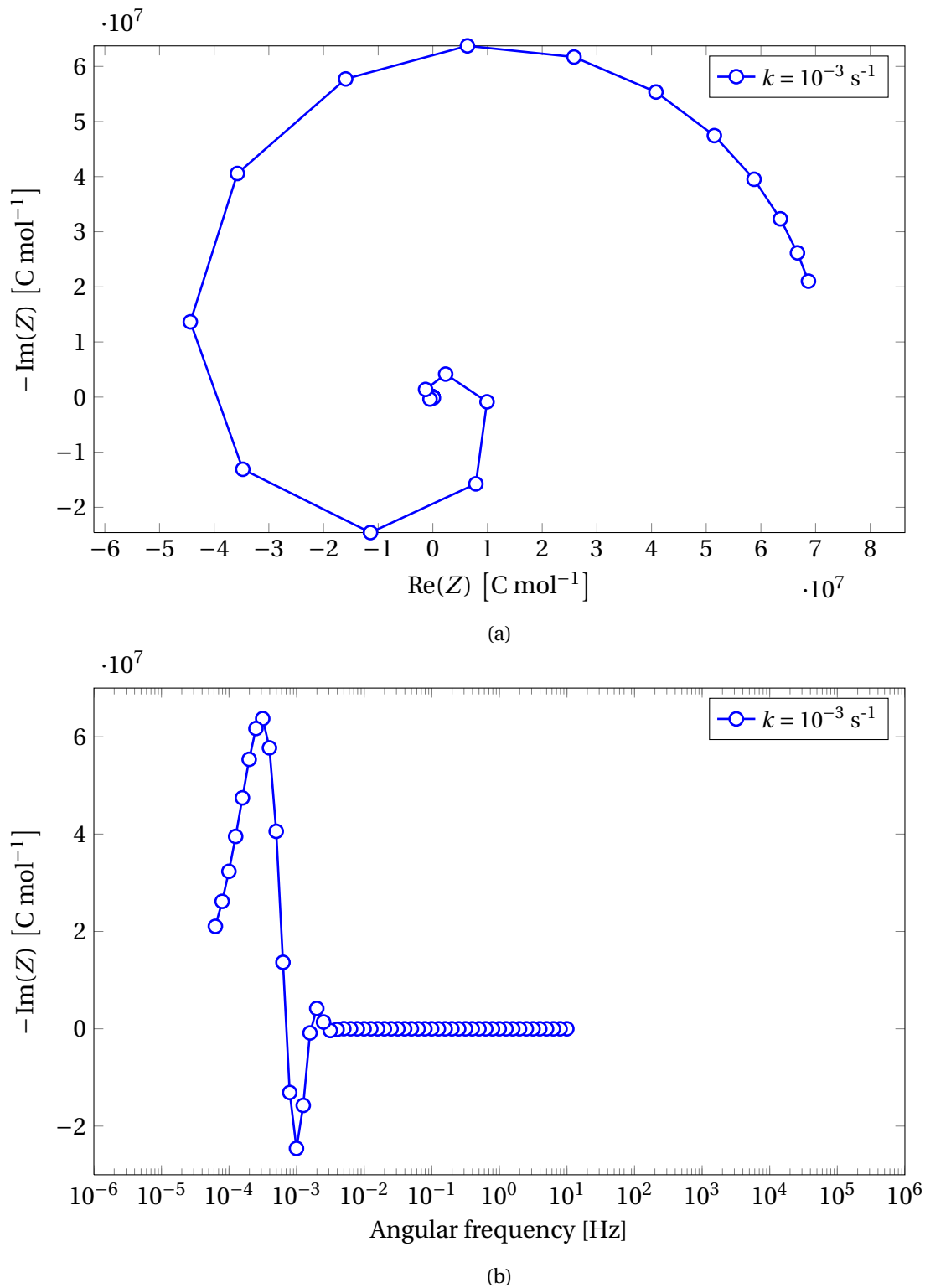
# 5 Discussion

## 5.1 Introduction

In Section 5.2 the limitations of the derived model and transfer functions are discussed. In Section 5.3 applications of the derived model are investigated. In Section 5.4 the convergence of the numerical approach by Newman's BAND(J) subroutine is investigated in more detail. The mathematical description of the resulting impedance spectra is explained in Section 5.5 by the steady-state relation between the measured potential, light intensity and faradaic current density. Finally, a physical interpretation of the impedance spectra by rate constant analysis is performed in Section 5.6.

## 5.2 Limitations of the modeled impedance transfer functions

A clear limitation in the derived model is that under zero illumination and steady-state current, the steady-state concentration expressed by Eq. (3.27) equals to zero. This is however not the case, as a constant equilibrium concentration $c_{e,0}$ is observed. In previous results [31], a correction for this was proposed by including an additive term in the derived steady-state concentration term on the form

$$c_e(x)_{\text{corrected}} = c_e(x) + c_{e,0} \tag{5.1}$$

However, a simple addition of such a term does not take the physical aspects of the system into consideration, just the mathematical treatment of including the equilibrium concentration under zero illumination and steady-state current. Also, the addition of this term does not fulfill the steady-state diffusion equation in Eq. (3.11). One possible solution to this problem is to include the equilibrium concentration in a similar way described by Sódergren et al. [11] and Cao et. al [21], in which the steady-state diffusion equation may be written

$$0 = D \frac{\partial^2 c_e}{\partial x^2} - k(c_e - c_{e0}) + I_0 \alpha e^{-\alpha x} \tag{5.2}$$

The corrected steady-state on the form described in Eq. (5.1) should fulfill this diffusion equation. However, a more detailed study of this inclusion is recommended. This correction may readily be included in the derived expression in this study, but may also change the trend in the resulting impedance spectra. However, the physical interpretation discussed below should still be valid, and may assist in explaining any changes in the impedance spectra when including the equilibrium concentration. Also, the resulting trends in the impedance spectra in this study should occur for sufficiently low steady-state concentrations in the corrected model.

The calculated impedance spectra for IMPS in this study show a change in quadrant that is not

reported elsewhere. This could be caused by the introduction of mixed conductivity, or the disregarding of the equilibrium concentration as described above. The physical interpretation of the IMPS transfer function discussed below should, however, still hold.

## 5.3   Applications of the modeled impedance transfer functions

From the results in Section 4, the introduction of mixed conductivity may alter the calculated impedance spectra depending on the measure technique. The calculated photoelectrochemical impedance spectra and as IMPS spectra both showed strong dependency of the degree of mixed conductivity. The IMVS transfer function, however, is rather insensitive to the introduction of mixed conductivity.

From the derived expression for the modulating concentration profile in Eq. (3.35), there was found two contributions to the oscillation; the oscillating faradaic current density $\mathscr{L}\{\tilde{i}_f\}$ and the oscillating light intensity $\mathscr{L}\{\tilde{I}_0\}$. Thus, how these are affected by the degree of mixed conductivity may thus explain of the impedance spectra for mixed conducting electrodes differ from pure electrical conducting electrodes. To obtain charge neutrality, the current in and out of the electrode must at all times remain equal. From the defined boundary conditions at the electrode interfaces (from Eq. (3.33) at $x = 0$ and (3.34) at $x = L$), the chosen transport number should describe the slope of the concentration profile at the interface. When one transport number is set close to unity, a steep profile is observed where $t_i \approx 0$, and a flat profile is observed where $t_i \approx 1$. For equal transport numbers, a symmetrical concentration profile is observed. In the speciation for this study, a steep profile is observed close to $x = 0$ and a flat profile is observed for $x = L$ when assuming nearly pure electrical conducting properties. By modulating the current density, the concentration close to the solution interface will modulate while the concentration at the support is nearly constant, when assuming nearly pure electrical conducting properties. Thus, the solution interface will be of most importance for this system. When the transport numbers are set equal, the concentration close to both the solution interface and support interface modulate. Thus, both interfaces are important for mixed conducting systems.

For reasonably large adsorption coefficients, the light intensity will only affect the concentration profile close to the surface at which the electrode is illuminated (here assumed at the solution interface). Thus, by modulating the light, the solution interface is of most importance.

To illustrate this, the steady-state concentration profile for a near pure electrical conducting electrode illuminated with light intensities $I_0 = 10^6$ and $I_0 = 10^{-5}$ mol cm$^{-2}$ s$^{-1}$ for $k = 10^{-2}$ s$^{-1}$ is given in Figure 5.1a, and for $t_+ = t_- = 0.5$ in Figure 5.1b. Here, we clearly see that illumination at the electrolyte interface affects the concentration profile close to the surface only. By setting $t_+ \approx= 1$ as in Figure 5.1a, oscillation of the faradaic current should only affect the concentration close to $x = 0$. By setting $t_+ = t_- = 0.5$ as in Figure 5.1b, oscillation of the faradaic current affects both interfaces.
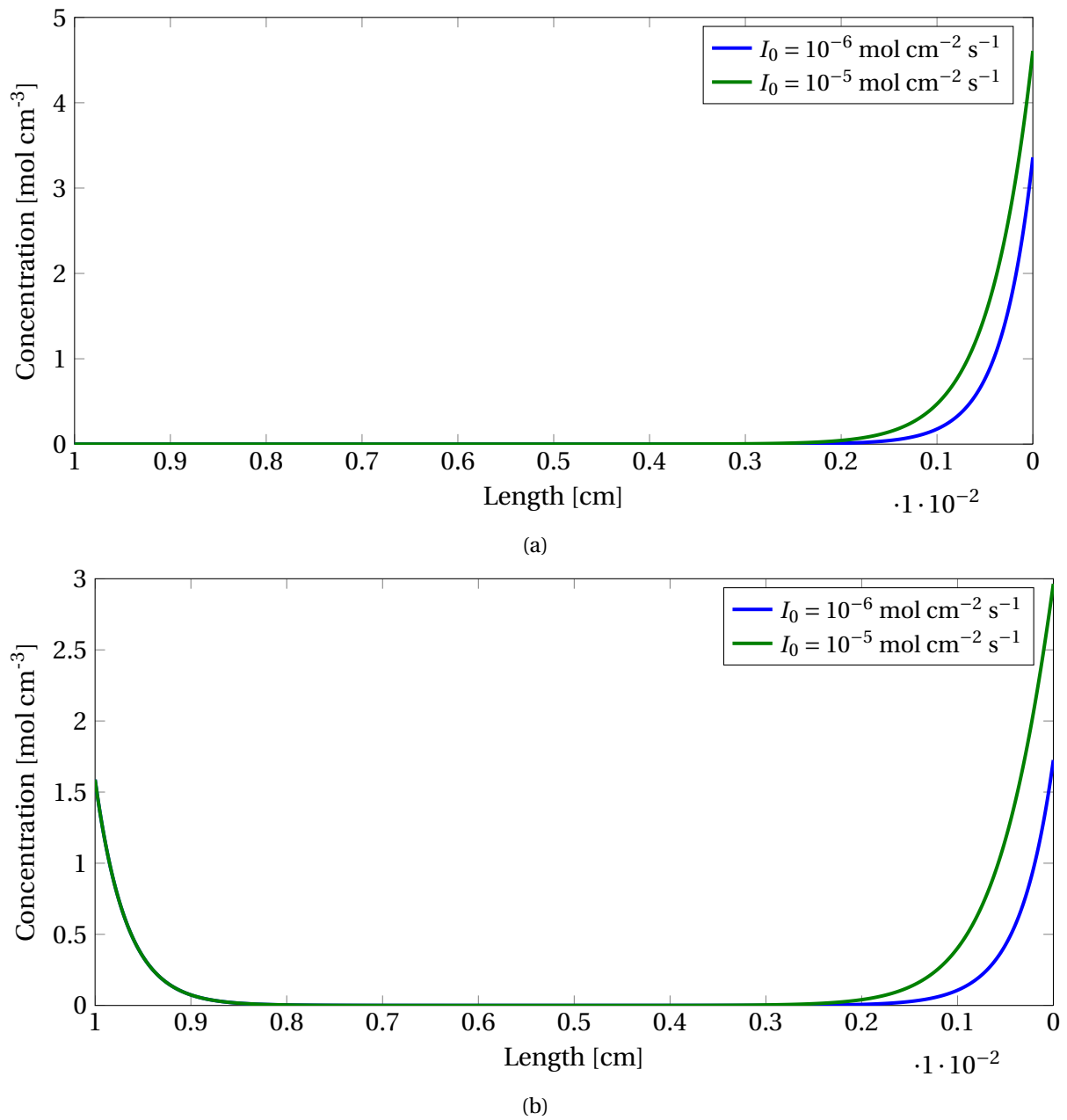
Figure 5.1: a Steady-state concentration profile assuming $t_+ \approx 1$. b Steady-state concentration profile assuming $t_+ = t_- = 0.5$.

Since the photoelectrochemical impedance spectrum is defined as the modulated potential as a function of modulated current, the electrode with mixed conductivity should may be changed so both interfaces contribute. Similarly, for the IMPS spectra, the modulating current as a function of of light intensity will also be altered, where the solution interface is of most importance. IMVS measurements, however, is conducted at open circuit conditions. That is, the current density is zero. Thus, only the light modulation is affecting the charge transfer flow, and the IMVS spectra should be equal for mixed conducting and pure electrical conducting electrodes.

From the results above, we clearly see that the charge recombination rate across the bulk electrode may be extracted from the resulting impedance spectra. The most straight forward method to determine the rate constant is to investigate the electrode by IMVS measurements, as it has been showed that the impedance spectra from IMVS measurements has one characteristic maximum in the imaginary part of impedance located at a frequency equal to the rate constant $k$. $k$ may also be extracted from the other methods, but can be quite ambiguous, however, as these methods show several processes with rate constants close to $k$ and may be difficult to distinct.

IMPS-measurements may be used to measure the electrode kinetics at the solution interface for sufficiently low recombination rates and applied current density, as one characteristic minimum in the imaginary part of the impedance plane plot is assumed to be occurring at a frequency equal to the back charge transfer rate at the solution interface. This may be obtained both for pure electrical conducting and mixed conducting systems.

The diffusion coefficients $D_i$ for species $i$ may be found by photoelectrochemical impedance measurements. It was shown that the photoelectrochemical impedance spectrum showed straight line corresponding to a diffusion limiting process in the high frequency region. If the mobilities and charge numbers of the species are known, the diffusion coefficient may be found from Eq. (3.6). If the diffusion coefficient is known, the mobilities may be found. The electrode kinetics at the solution interface when assuming a mixed conducting electrode may be extracted from photoelectrochemical impedance measurements , as it was assumed that for intermediate recombination rates a characteristic rate constant corresponding to the electrode kinetics at the support was observed.

## 5.4   Numerical modeling by Newman's BAND(J) subroutine

From the step size analysis of Newman's BAND(J) subroutine it was found that the subroutine does not show the expected linear trend of convergence with the square of the step size. The error in the numerical approximation of a function $f(x)$ is a sum of the second and higher order derivatives of the function on the form [35] $H^2 f^{(2)}(x) + H^4 f^{(4)} + H^6 f^{(6)}(x) + \ldots$, where $f^{(n)}$ is the $n$-th order derivative. Richardson [35] suggests that for sufficiently low step sizes, the second order derivative is the main

contributor to the error, and thus the numerical approximation should show a linear trend with $H^2$. However, if the higher order derivatives are large, these will still contribute to a certain extend and the error may not show $H^2$-dependency. This may be further investigated by a higher-order Richardson's iteration method [35].

## 5.5   Mathematical treatment of the thin film transfer functions by steady-state analysis

### 5.5.1   Mathematical treatment of the IMPS transfer function

IMPS measurements are done under short circuit conditions, that is, the measured electrochemical potential is kept constant. From Figure 4.30, we clearly see that by keeping the faradaic current density constant when changing the light intensity, the potential changes. Thus, by changing the light intensity $I_0$ in Eq. (3.142), the steady-state faradaic current density $i_{f,e}$ must change accordingly to maintain a constant potential. The change of $i_{f,e}$ as a function of $I_0$ by keeping the potential constant for $k = 10^{-2}$ s$^{-1}$ is given in Figure 5.2a, and the resulting measured potential is given in Figure 5.2b. For these calculations, $I_0$ is kept constant for each calculation, and $i_{f,e}$ is changed with with a certain factor from the original value in the appropriate direction. For low values of $I_0$ we observe an increase in $i_{f,e}$, which reaches a maximum around $I_0 = 4 \times 10^{-5}$, in accordance with the Figure 4.30. A further increase $I_0$ leads to a decrease in $i_{f,e}$.

The plot of the faradaic current density as a function of light intensity, such as the one in Figure 5.2a, should explain mathematically the resulting impedance spectrum. The IMPS transfer function gives the fraction between the faradaic current density perturbation $\mathscr{L}\{\tilde{i}_f\}$ and light intensity perturbation $\mathscr{L}\{\tilde{I}_0\}$ at different frequencies when we assume the oscillating faradaic current density and light intensity on the form $i_f = i_f(x,0) + \tilde{i}_f(x,t)$ and $I_0 = I_0(x,0) + \tilde{I}_0(x,t)$, respectively. Since these perturbations are small changes in faradaic current density and light intensity, that is, $\partial i_f$ and $\partial I_0$ respectively, the IMPS transfer function is expected to be directly linked to the sign of the derivative of faradaic current density with respect to light intensity $\partial i_f / \partial I_0$.

For the calculations represented in Figure 5.2, we see that in order to maintain a constant measured electrochemical potential, the current goes from increasing values to decreasing values between $I_0 = 1 \times 10^{-6}$ to $I_0 = 10^{-5}$ mol cm$^{-2}$ s$^{-1}$. At the point in which $\partial i_f / \partial I_0$ changes from positive to negative sign, we investigate if the calculated IMPS response goes from $\mathrm{Re}(Z) > 0$, $-\mathrm{Im}(Z) > 0$ to $\mathrm{Re}(Z) < 0$, $-\mathrm{Im}(Z) < 0$ when keeping the steady-state faradaic current density constant. The calculated IMPS response by keeping $i_{f,e}$ constant and equal to $i_{f,e} = 1$ A cm$^{-2}$ for the same $I_0$ range as described above is given in Figure 5.3. We observe that the IMPS response changes quadrant in the same range of $I_0$ values as that of the change in sign of $\partial i_f / \partial I_0$. Thus, the quadrant in which the IMPS transfer function occurs is directly linked to the sign of $\partial i_f / \partial I_0$, as expected.

(a)



(b)

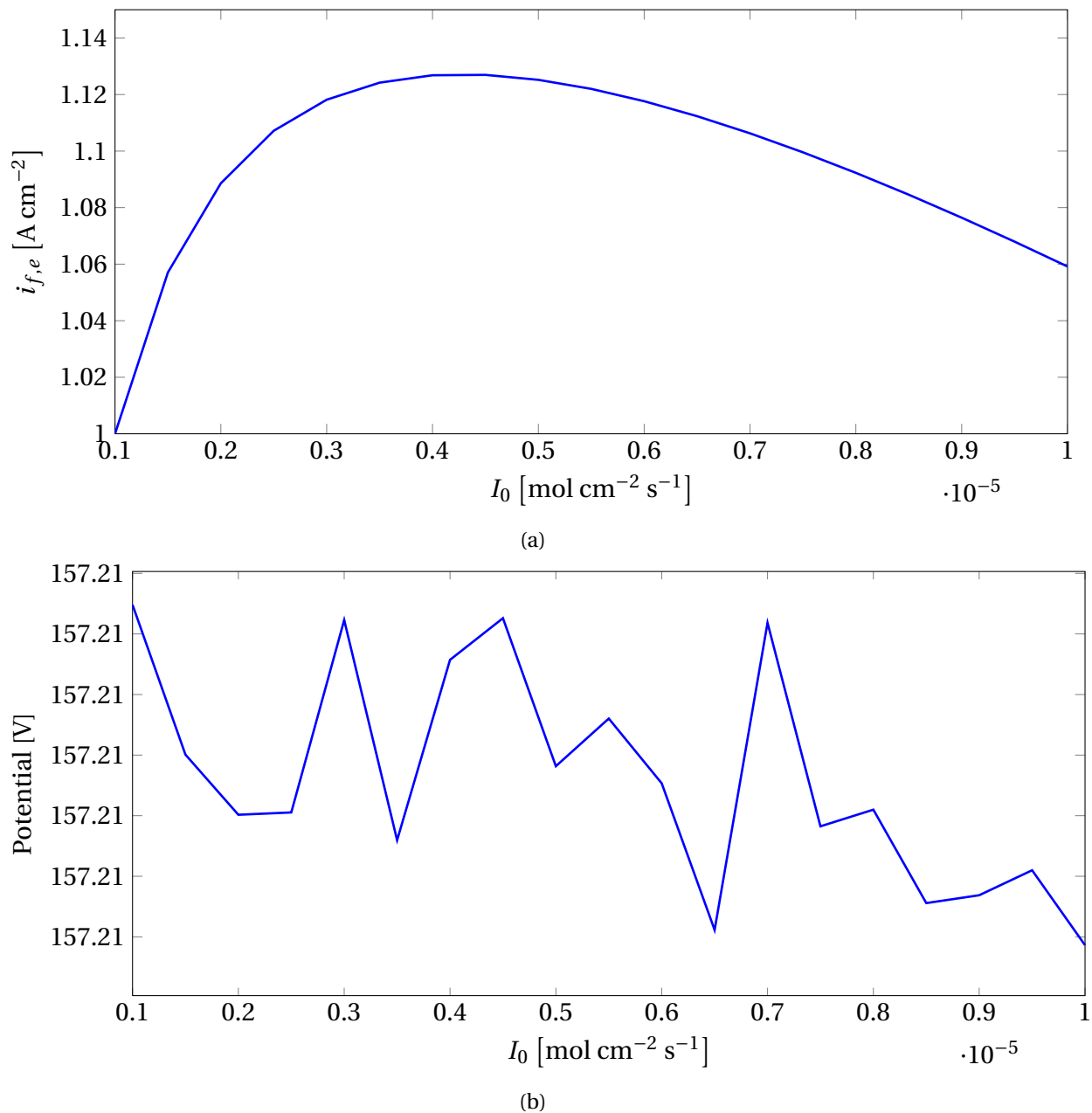Figure 5.2: a Change in faradaic current density $i_{f,e}$ as a function of $I_0$ under short circuit conditions, that is, keeping the measured electrochemical potential $V$ constant. b Resulting potential as a function of $I_0$ and the new calculated $i_{f,e}$. Calculations done for $I0$ in the range of $10^{-6}$ to $10^{-5}$ mol cm$^{-2}$ s$^{-1}$, $k = 10^{-2}$ s$^{-1}$, and $\alpha = 2500$ cm$^{-1}$.
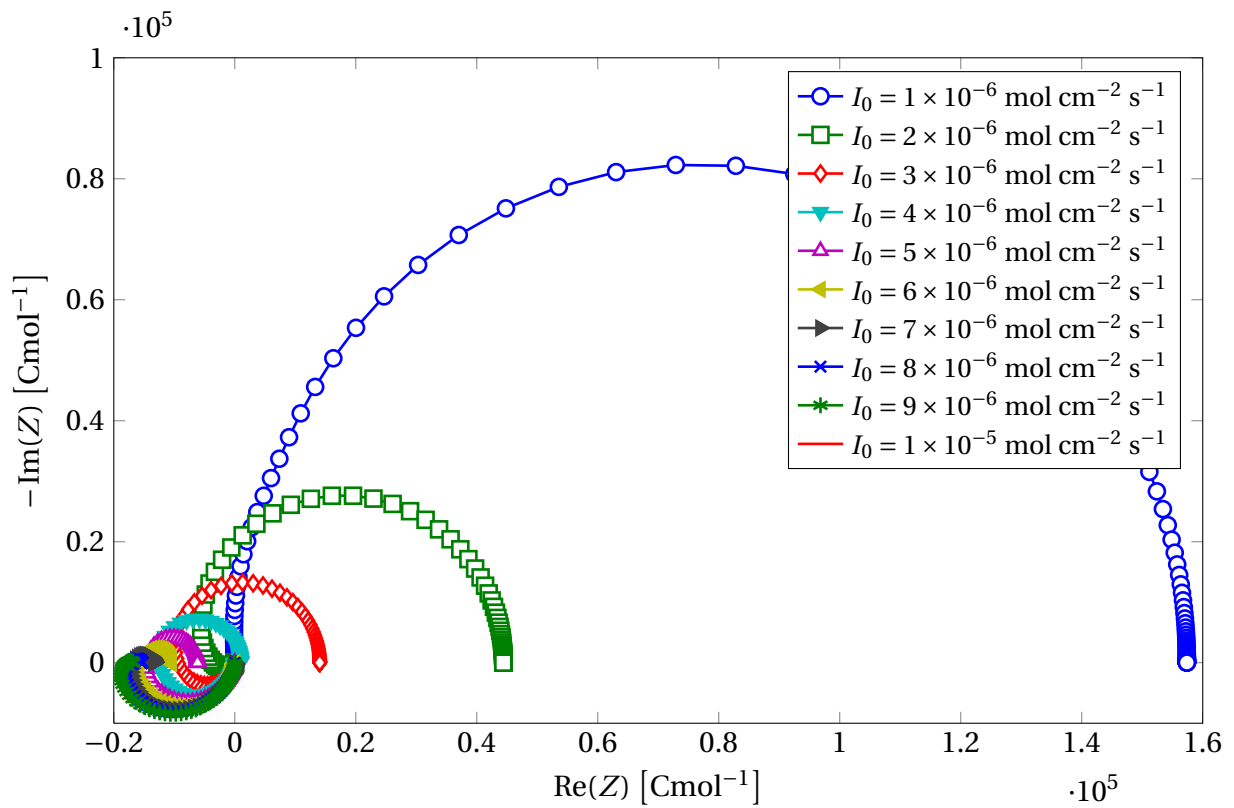
Figure 5.3: IMPS response by keeping $i_{f,e}$ constant and equal to $i_{f,e} = 1\,\mathrm{A\,cm^{-2}}$ for $I_0$ values of $10^{-6}$ to $10^{-5}$ mol cm$^{-2}$ s$^{-1}$. A change in the quadrant is observed in the same $I_0$ region as the change in $i_{f,e}$ trend with increasing $I_0$ by keeping the electrochemical potential constant. $k = 10^{-2}$ s$^{-1}$, $\alpha = 2500$ cm$^{-1}$.

The current as a function of light intensity under constant potential for a large $k$-value of $k = 10^{-1}$ s$^{-1}$ and a low $k$-value of $k = 10^{-3}$ s$^{-1}$ is given in Figure 5.4a and 5.4c, respectively, for the same light intensity region chosen for $k = 10^{-2}$ as described above. Here, we observe an increase in the faradaic current density with increasing light intensity for a high rate constant, and a decrease in the faradaic current density with increasing light intensity for a low rate constant. We have also included the IMPS impedance plane plots for $k = 10^{-1}$ s$^{-1}$ in Figure 5.4b and for $k = 10^{-3}$ s$^{-1}$ in Figure 5.4d. For a large $k$-value we observe $\mathrm{Re}(Z) > 0$ and $-\mathrm{Im}(Z) > 0$ for all $I_0$-values, and for a low $k$-value we observe $\mathrm{Re}(Z) < 0$ and $-\mathrm{Im}(Z) < 0$ for all $I_0$-values, as expected.

### 5.5.2   Mathematical treatment of the IMVS transfer function

For the IMVS spectra in Section 4.3.4, we observed all spectra in the first quadrant. From these results we expect the measured potential to increase with increasing light intensity, that is, the derivative $\partial V / \partial I_0$ to be greater than zero. This is expected, since the IMVS transfer function gives the fraction between the measured potential perturbation $\mathscr{L}\{\tilde{V}\}$ and the light intensity perturbation $\mathscr{L}\{\tilde{I}_0\}$ when we assume the oscillating potential and light intensity on the form $V = V(x,0) + \tilde{V}(x,t)$ and $I_0 = I_0(x,0) + \tilde{I}_0(x,t)$. Since these perturbations are small changes in potential and light intensity, that is, $\partial V$ and $\partial I_0$ respectively, hence the IMVS transfer function is expected to be directly linked to the sign of the derivative of measured potential with respect to light intensity $\partial V / \partial I_0$.

In Figure 5.5, the measured potential under open circuit conditions $i_{f,e} = 0$ is plotted as a function of light intensity for rate constants between $k = 10^{-3}$ and $k = 10^{-1}$ s$^{-1}$. From these results, we observe a positive gradient $\partial V / \partial I_0$ for all rate constants. Thus, the IMVS transfer function is expected to occur in the first quadrant.

### 5.5.3   Mathematical treatment of the photoelectrochemical impedance response

From the resulting photoelectrochemical impedance spectra in Section 4, we observed a dome shape in the positive imaginary plane for the impedance plane plot. This should correspond to a charge transfer limiting process in which the current oscillates in the opposite direction as the potential. In this study we assume this to be a back charge transfer between the electrode and electrolyte, as described in more detail in Section 5.6. This dome is found to be more apparent by reducing the applied faradaic current density. A similar mathematical treatment as described above could be done for this transfer function be keeping the light intensity constant and investigate how the current density and potential changes accordingly. This should give similar results as described above.
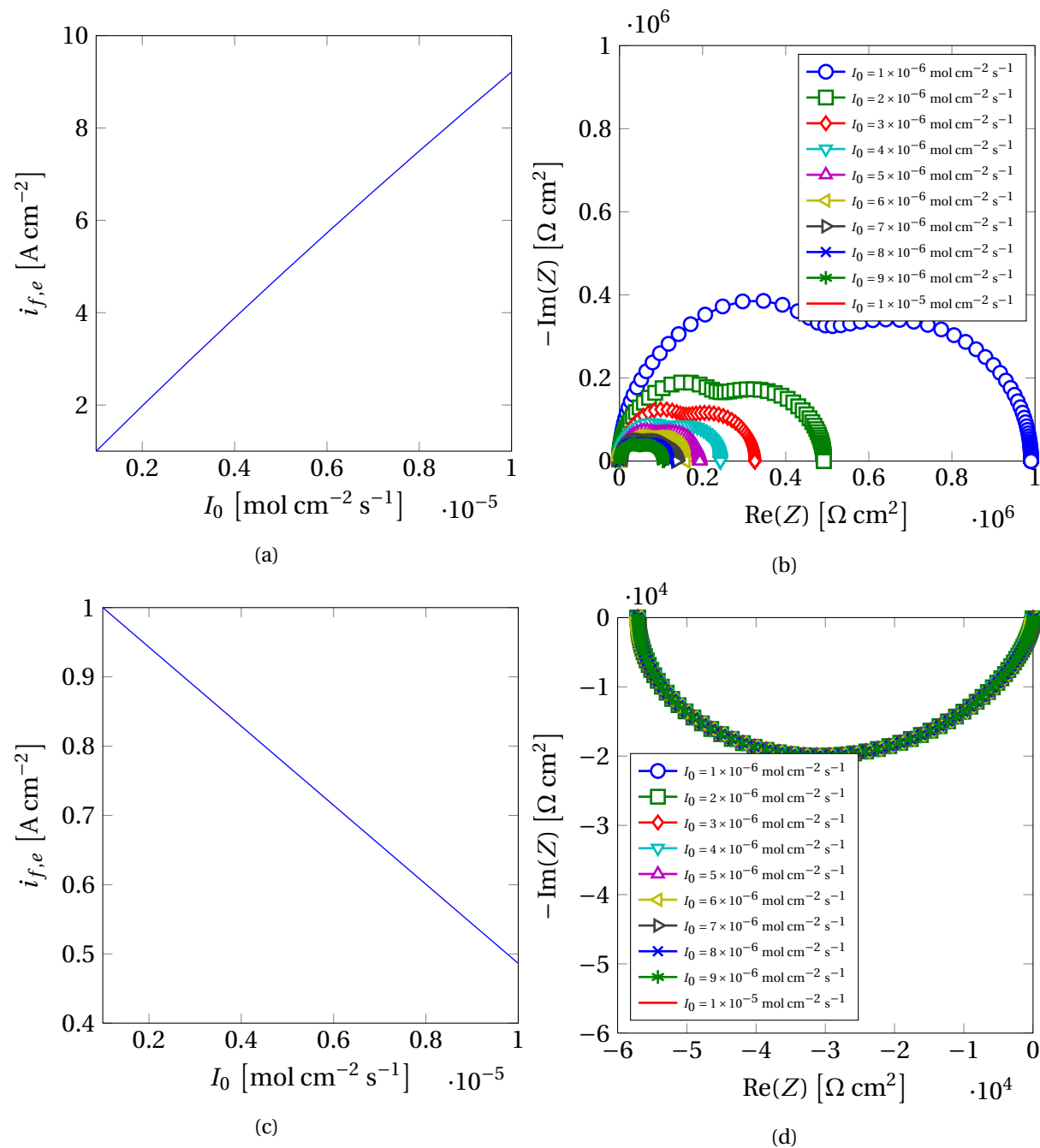
Figure 5.4: a An observed increase in faradaic current density with increasing light intensity and b resulting IMPS spectrum for $k = 10^{-1}$ s$^{-1}$. c An observed decrease in faradaic current density with increasing light intensity and d resulting IMPS spectrum for $k = 10^{-3}$ s$^{-1}$.
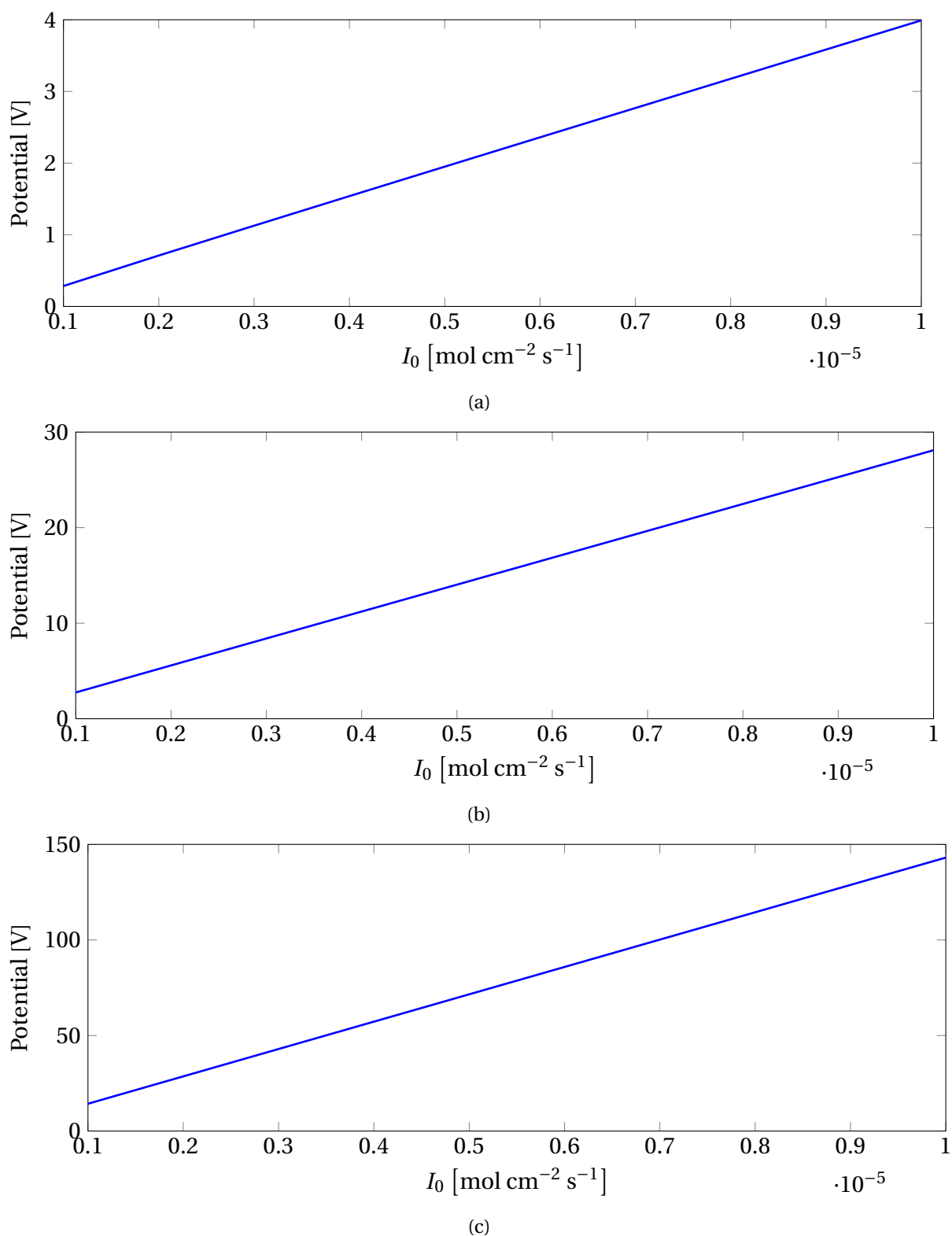
(a)



(b)



(c)

Figure 5.5: Measured electrochemical potential as a function of light intensity at open circuit conditions $i_{f,e} = 0$ for a rate constant a $k = 10^{-1}$ s$^{-1}$, b $k = 10^{-2}$ s$^{-1}$, and c $k = 10^{-3}$ s$^{-1}$. Calculated for $\alpha = 2500$ cm$^{-1}$, and for light intensities in the range of $10^{-6}$ to $10^{-5}$ mol cm$^{-2}$ s$^{-1}$.

## 5.6  Physical interpretation of the thin film transfer functions by rate constant analysis

In this study, we focus on four processes regarding flow of charge carriers in the electrode system; diffusion of charge carriers across the electrode caused by concentration gradients under illumination and an applied current, generation of charge carriers under illumination, charge transfer across the interfaces, and recombination of charge carriers to neutral species in the electrode material. The three latter charge carrier flow processes are investigated below to give a physical interpretation of the proposed mathematical explanation above.

### 5.6.1  Photogeneration under illumination

When the semiconductor is illuminated, charge carriers are generated by excitation of electrons from the valance band (VB) to the conduction band (CB) and holes from conduction band to valance band, as sketched in Figure 5.6 for illumination at the electrolyte interface ($x = 0$). When we assume a sufficiently large absorption coefficient $\alpha$, we expect the steady-state concentration to increase with increasing light intensity close to the surface at which the electrode is illuminated.

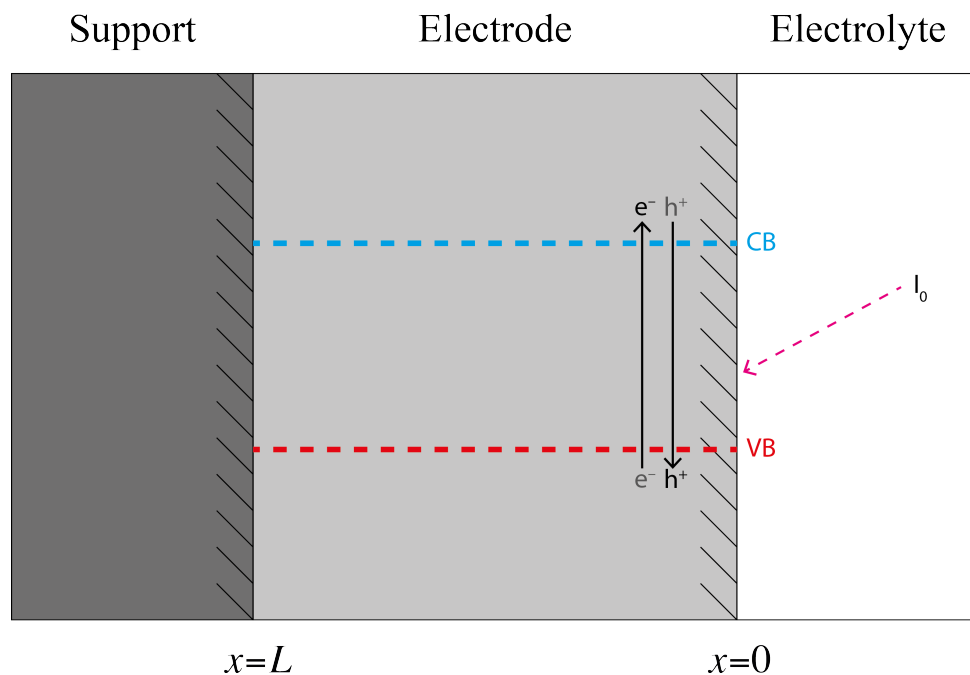Figure 5.6: Electrons are excited from VB to CB and holes from CB to VB producing a net increase in charge carrier concentration, generating a photocurrent.

### 5.6.2  Charge transfer and recombination

We assume a system that blocks positive species at the electrolyte interface ($x = 0$) and blocks negative species at the support interface ($x = L$). Thus, charge transfer at the electrolyte interface is given by

either feeding electrons to or draining electrons from the conduction band, and the charge transfer at the support interface is given by either feeding holes to or draining holes from the valance band. Charge carriers may also recombine to neutral species, described by the rate constant $k$. These two charge carrier flow processes are described in Figure 5.7.
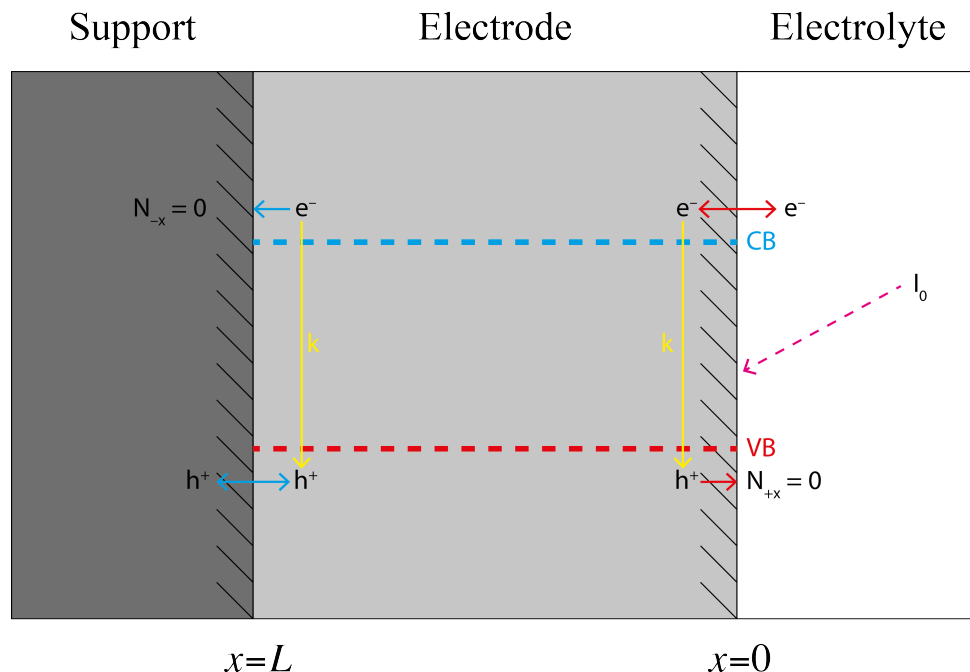


Figure 5.7: Representation of charge transfer and recombination processes in the electrode system. Electrons may transfer at the electrolyte interface at $x = 0$ and holes may transfer at the support interface at $x = L$. Charge carriers may also recombine to neutral species, described by the rate constant $k$.

### 5.6.3   Change in the net faradaic current density

The change in net faradaic current density is dependent on the concentration profile across the electrode material. As mentioned above, increasing the light intensity will increase the charge concentration close to the electrolyte surface when we assume a sufficiently large adsorption coefficient $\alpha$. For a reasonably high recombination rate, the photogenerated charge carriers will quickly recombine close to the solution interface before being able to diffuse into the electrode material, thus a steeper concentration profile is observed. In order to keep the potential constant, we expect an increase in the flux of charge carriers across the solution interface with increasing light intensity, thus an increase in the net the faradaic current density is observed. This is shown in Figure 5.8, where $N_{ix}$ represents the change in net charge carrier flux across the interface.

For low recombination rates, the photogenerated charge carriers diffuse to a larger degree into the material before they recombine. This may lead to a flattened concentration profile close to the solution interface. In order to keep the potential constant, the flux of charge carriers across the solu-
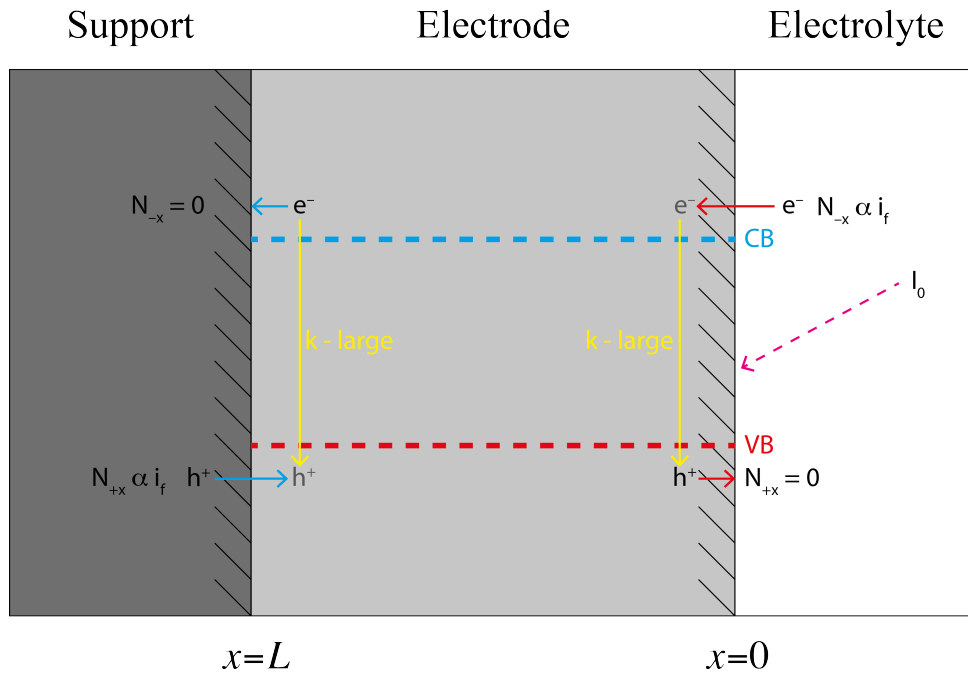
Figure 5.8: For large values of $k$, the photogenerated charge carriers close to the solution interface quickly recombine before being able diffusing into the electrode material. To keep the potential constant, an increase in the faradaic current density is observed, represented by a positive change in net charge carrier flux across the interface $N_{ix} > 0$.

tion interface needs to be reduced. Thus, we observe a decrease in the net faradaic current density with increasing light intensity. This is shown in Figure 5.9, where where $N_{ix}$ represents the change in net charge carrier flux across the interface.

### 5.6.4   Derivative analyisis

In Figure 5.10, the derivate of $c_e(x)$ with respect of $x$ is plotted across the electrode length for $k = 10^{-2}$ s$^{-1}$ for constant faradaic current and constant potential in Figure 5.10a and 5.10b, respectively. From the boundary conditions in Eq. (3.19) and (3.22), we expect the derivative to have a constant value at the electrode interfaces when keeping the faradaic current density constant, as shown in Figure 5.10a. However, by keeping the potential constant, the faradaic current at the interfaces need to accommodate for the competition between charge generation and recombination, as described above. This is shown in Figure 5.10b. First, the gradient increases in magnitude with increasing light intensity. However, when the light intensity reaches a certain threshold value, the recombination does not accommodate the charge generation, and the gradient, and thus the faradaic current is, reduced at the electrode interfaces.
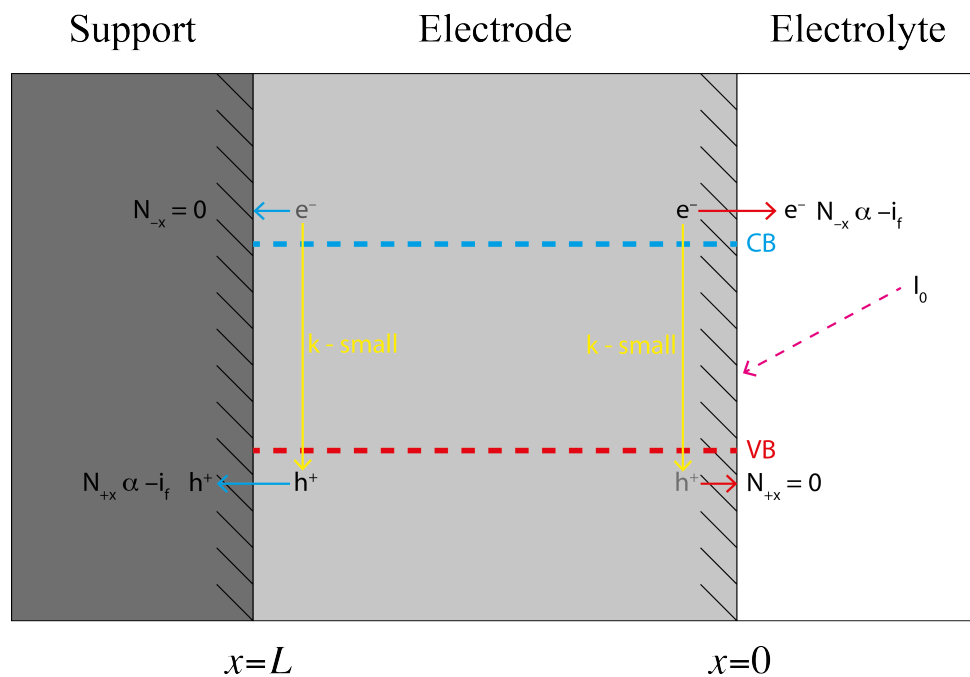
Figure 5.9: For low values of *k*, the photogenerated charge carriers close to the solution are able to diffuse into the electrode material before recombining. To keep the potential constant, a decrease in the faradaic current density is observed, represented by a negative change in net charge carrier flux across the interface $N_{ix} < 0$.

Figure 5.10: Derivative of the steady-state concentration with a constant faradaic current, and b constant potential. Calculations done for $k = 10^{-2}$ s$^{-1}$, $\alpha = 2500$ s$^{-1}$, and $i_{f,e} = 1$ A cm$^{-2}$ at $I_0 = 10^{-6}$ mol cm$^{-2}$ s$^{-1}$.

# 6 Conclusion

Mathematical models for electrochemical and photoelectrochemical impedance transfer functions for films have been developed. These models include electrochemical impedance spectroscopy (EIS), photoelectrochemical impedance spectroscopy (EIS), intensity-modulated photovoltage spectroscopy (IMVS), and intensity-modu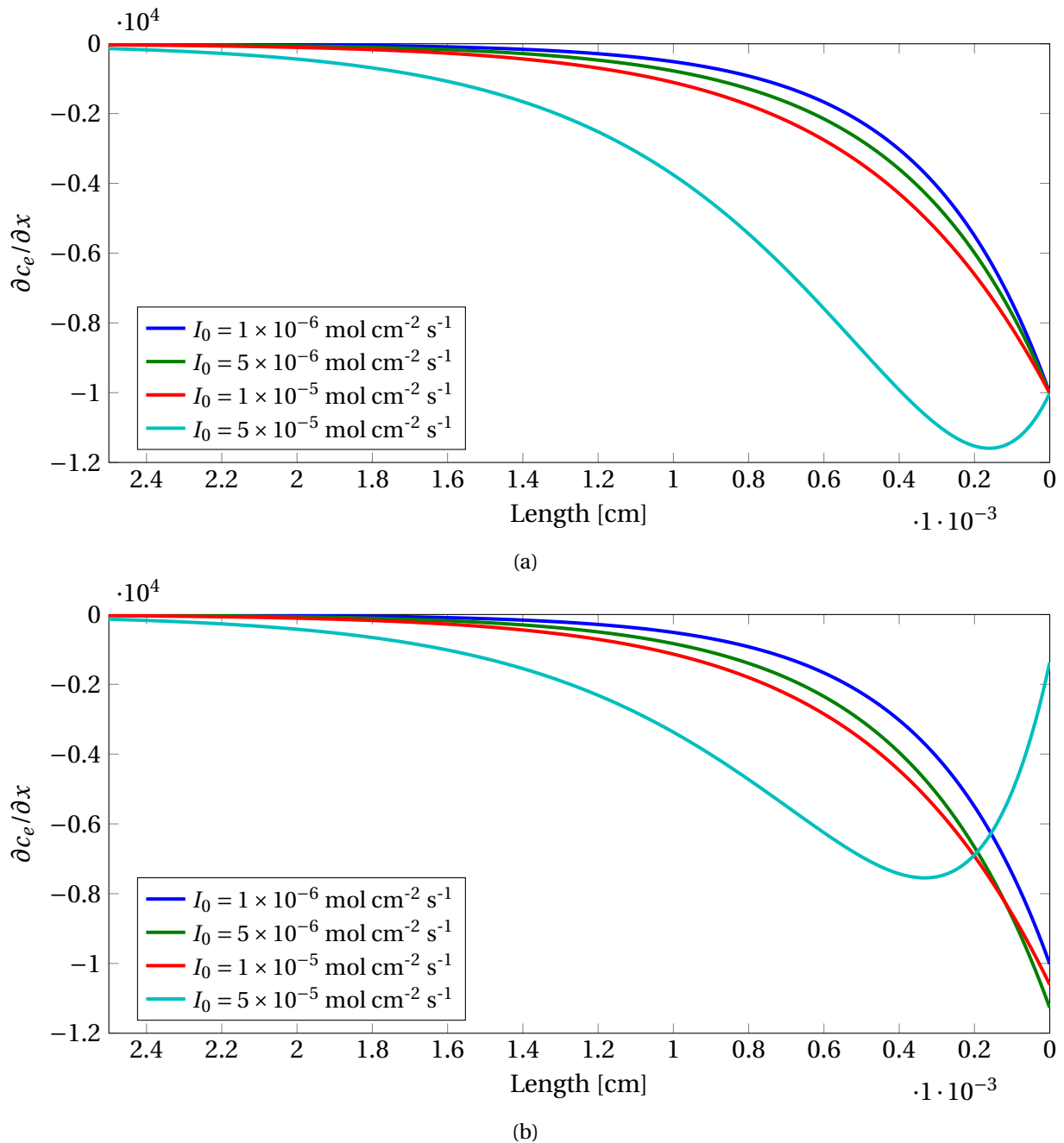lated photocurrent spectroscopy (IMPS) for mixed conducting photo-electrochemical thin films, and intensity-modulated photocurrent spectroscopy (IMPS) for mixed conducting microporous thin films. In addition a short study of the step size dependency of the convergence for numerical modeling approach using Newman's BAND(J) subroutine to solve a second order diffusion equation has beed performed.

It was found that the photoelectrochemical impedance (EIS) transfer function and intensity-modulated photocurrent spectroscopy (IMPS) transfer function was dependent on the degree of mixed conductivity. The intensity-modulated photovoltage spectroscopy (IMVS) transfer function, however, was found to be independent of degree of mixed conductivity.

The convergence of the numerical approach using Newman's BAND(J) subroutine does not show the expected convergency trend. It was proposed that this may be caused by the higher derivatives of the modeled equations, and a more detailed study of the numerical approach using a higher order Richardson's iteration method was suggested.

The electrochemical impedance spectroscopy (EIS) transfer function showed a reflective-like behavior, with a charge limiting dome in the low frequency region in the impedance plane plot corresponding to charge recombination across the bulk electrode.

The photoelectrochemical impedance spectroscopy (EIS) transfer function showed to distinct charge transfer limiting processes in the low frequency region. It was found that one of the domes corresponded to charge recombination across the bulk electrode. The other dome was assumed to correspond to a charge transfer process between the electrode and electrolyte described by the surface electrode kinetics at the solution interface.

The intensity-modulated photovoltage spectroscopy (IMVS) transfer function showed one charge limiting process corresponding to recombination across the bulk material. For low rate constants, the system is charge transfer limiting in the low frequency region and diffusion limiting in the high frequency region.

The intensity-modulated photocurrent spectroscopy (IMPS) transfer function showed to charge limiting processes. It was found that one of the domes corresponded to charge recombination across the bulk electrode. The other dome was assumed to correspond to a charge transfer process between the electrode and electrolyte described by the surface electrode kinetics at the solution interface. For high light intensities and low rate constants, the transfer function showed a change in quadrant. This

was explained by a change in the direction of charge transfer between electrode and electrolyte to maintain a constant potential when the photogeneration process rate exceeds the recombination process rate.

A relation between measured potential, current density, and light intensity was developed, and was utilized to explain the physical interpretation of the impedance transfer functions.

The derived steady-state concentration profile disregard the equilibrium concentration under zero illumination and applied current density. A route to include this by including an equilibrium concentration term in the steady-state diffusion equation and solving the equation with appropriate boundary conditions was suggested.

# 7 Suggested further work

The modeled impedance spectra may be used to assist the interpretation of experimental data. It is recommended to investigate the models validity by performing impedance measurement on known systems, and compare the experimental results to the calculated impedance spectra. This will locate any deviations or limitations with the derived models, and proper corrections to the derived models may be found.

A more detailed study of the inclusion of the equilibrium steady-state concentration under zero illumination and applied current-density is advised. One suggested route is to define the steady-state diffusion equation in similar terms as Cao et. al [21], and solve the corrected differential equation with the procedure described in this study. A steady-state concentration profile with an accurate inclusion of the equilibrium steady-state concentration should be obtained. This altered steady-state concentration profile may be readily included in the existing models, as it will not affect the nonsteady-state diffusion equation and resulting modulating concentration profile. The calculated impedance spectra may be changed compared to this study, and it is advised to do the equilibrium concentration inclusion simultaneously with experimental measurements. The discussed physical interpretation should still be valid, and may be used as aid in interpreting the new calculated impedance spectra.

A study of the two other derived IMPS transfer functions should be investigated in more detail. They may give aid to more clearly understanding and interpreting IMPS transfer functions as they are derived for more simple systems, and thus the physical interpretation should be straight forward.

The microporous thin film electrode in Section 3.4 should be analyzed in more detail. In the time span of this study, a more detailed study and description of this model was not performed and is highly recommended for further work. The analogy of describing the sink term in the diffusion equation as a recombination process from electrode to electrolyte across the micropore surface may be utilized when deriving impedance transfer functions for microporous systems.

# References

[1] United Nations. Department of Economic and Social Affairs, 1999.

[2] International Energy Agency (IEA). World energy outlook (2007). Available from: http://www.worldenergyoutlook.org/media/weowebsite/2008-1994/weo_2007.pdf, accessed December 12, 2013.

[3] H. Rogner, D. Zhou, R. Bradley, P. Crabbé, O. Edenhofer, B. Hare, L. Kuijpers, and M. Yamaguchi. Introduction In Climate Change 2007: Mitigation. Contribution of Working Group III to the Fourth Assessment Report of the Intergovernmental Panel on Climate Change. Available from: http://www.ipcc.ch/pdf/assessment-report/ar4/wg3/ar4-wg3-chapter1.pdf, accessed December 9, 2013.

[4] M. Tjelta. *Electrochemical and photoelectrochemical characterization of porous semiconducting electrodes.* PhD thesis, Norwegian University of Science and Technology (NTNU), 2013.

[5] Hamnett A. Hamann, C. H. and W. Vielstich. *Electrochemistry, 2nd Ed.* Wiley-VCH, 1985.

[6] M. A. Green. *Solar cells: Operating Principles, Technology and System Applications.* The University of New South Wales, 1982.

[7] Md K. Nazeeruddin, E. Baranoff, and M. Graetzel. Dye-sensitized solar cells: A brief overview. *Solar Energy*, 85(6):1172–1178, 2011.

[8] E. Barsoukov and R. MacDonald. *Impedance Spectroscopy: Theory, Experiment, and Applications, 2nd Edition.* Wiley, 2005.

[9] B. A. Boukamp, M. Verbraeken, D. H. A. Blank, and P. Holtappels. SOFC anodes - proof for a finite-length type gerischer impedance? *Solid State Ionics*, 177(26-32):2539–2541, 2006.

[10] R. Kern, R. Sastrawan, J. Ferber, R. Stangl, and J. Luther. Modeling and interpretation of electrical impedance spectra of dye solar cells operated under open-circuit conditions. *Electrochimica Acta*, 47(26):4213–4225, 2002.

[11] S. Soedergren, A. Hagfeldt, J. Olsson, and S. Lindquist. Theoretical Models for the Action Spectrum and the Current-Voltage Characteristics of Microporous Semiconductor Films in Photoelectrochemical Cells. *The Journal of Physical Chemistry*, 98(21):5552–6, 1994.

[12] A. Y. Kim and M. Kang. High efficiency dye-sensitized solar cells based on multilayer stacked $TiO_2$ nanoparticle/nanotube photoelectrodes. *Journal of Photochemistry and Photobiology A: Chemistry*, 233:20–23, 2012.

[13] T. Hoshikawa, M. Yamada, R. Kikuchi, and K. Eguchi. Impedance Analysis of Internal Resistance Affecting the Photoelectrochemical Performance of Dye-Sensitized Solar Cells. *Journal of The Electrochemical Society*, 152(2):E68–E73, 2005.

[14] G. Schlichthoerl, N. G. Park, and A. J. Frank. Evaluation of the Charge-Collection Efficiency of Dye-Sensitized Nanocrystalline $TiO_2$ Solar Cells. *The Journal of Physical Chemistry B*, 103(5): 782–791, 1999.

[15] L. M. Peter and K. G. U. Wijayantha. Intensity dependence of the electron diffusion length in dye-sensitised nanocrystalline $TiO_2$ photovoltaic cells. *Electrochemistry Communications*, 1(12): 576–580, 1999.

[16] A. C. Fisher, L. M. Peter, E. A. Ponomarev, A. B. Walker, and K. G. U. Wijayantha. Intensity Dependence of the Back Reaction and Transport of Electrons in Dye-Sensitized Nanocrystalline $TiO_2$ Solar Cells. *The Journal of Physical Chemistry B*, 104(5):949–958, 2000.

[17] G. Schlichthoerl, S. Y. Huang, J. Sprague, and A. J. Frank. Band Edge Movement and Recombination Kinetics in Dye-Sensitized Nanocrystalline $TiO_2$ Solar Cells: A Study by Intensity Modulated Photovoltage Spectroscopy. *The Journal of Physical Chemistry B*, 101(41):8141–8155, 1997.

[18] L. M. Peter. Dynamic aspects of semiconductor photoelectrochemistry. *Chemical Reviews*, 90 (5):753–69, 1990.

[19] L. M. Peter, J. Li, R. Peat, H. J. Lewerenz, and J. Stumper. Frequency response analysis of intensity modulated photocurrents at semiconductor electrodes. *Electrochimica Acta*, 35(10):1657–64, 1990.

[20] E. A. Ponomarev and L. M. Peter. A generalized theory of intensity modulated photocurrent spectroscopy (IMPS). *Journal of Electroanalytical Chemistry*, 396(1-2):219–26, 1995.

[21] F. Cao, G. Oskam, and P. C. Searson. Electron Transport in Porous Nanocrystalline $TiO_2$ Photoelectrochemical Cells. *Journal of Physical Chemistry*, 100(42):17021–17027, 1996.

[22] P. E. de Jongh and D. Vanmaekelbergh. Trap-limited electronic transport in assemblies of nanometer-size $TiO_2$ particles. *Physical Review Letters*, 77(16):3427–3430, 1996.

[23] P. E. de Jongh and D. Vanmaekelbergh. Investigation of the electronic transport properties of nanocrystalline particulate $TiO_2$ electrodes by intensity-modulated photocurrent spectroscopy. *The Journal of Physical Chemistry B*, 101(14):2716–2722, 1997.

[24] L. Dloczik, O. Ileperuma, I. Lauermann, L. M. Peter, E. A. Ponomarev, G. Redmond, N. J. Shaw, and I. Uhlendorf. Dynamic Response of Dye-Sensitized Nanocrystalline Solar Cells: Characterization by Intensity-Modulated Photocurrent Spectroscopy. *The Journal of Physical Chemistry B,* 101(49):10281–10289, 1997.

[25] G. Franco, J. Gehring, L. M. Peter, E. A. Ponomarev, and I. Uhlendorf. Frequency-Resolved Optical Detection of Photoinjected Electrons in Dye-Sensitized Nanocrystalline Photovoltaic Cells. *The Journal of Physical Chemistry B,* 103(4):692–698, 1999.

[26] B. Van der Zanden and A. Goossens. The nature of electron migration in dye-sensitized nanostructured $TiO_2$. *The Journal of Physical Chemistry B (ACS Publications),* 104(30):7171–7178, 2000.

[27] L. Bay and K. West. An equivalent circuit approach to the modelling of the dynamics of dye sensitized solar cells. *Solar Energy Materials Solar Cells,* 87(1-4):613–628, 2005.

[28] S. Sunde, I. A. Lervik, M. Tsypkin, and L. Owe. Impedance analysis of nanostructured iridium oxide electrocatalysts. *Electrochimica Acta,* 55(26):7751–7760, 2010.

[29] S. Sunde, I. A. Lervik, L. Owe, and M. Tsypkin. An Impedance Model for a Porous Intercalation Electrode with Mixed Conductivity. *Journal of The Electrochemical Society,* 156(8):B927–B937, 2009.

[30] J. S. Newman. *Electrochemical Systems.* Prentice-Hall International Series in the Physical and Chemical Engineering Sciences, 1973.

[31] D. R. Småbråten. Mathematical Modeling of Electrochemical and Photoelectrochemical Impedance - Specialization project. 2013.

[32] S. H. Glarum and J. H. Marshall. The a-c response of iridium oxide films. *Journal of The Electrochemical Society,* 127(7):1467–74, 1980.

[33] K. Rottmann. *Matematisk formelsamling.* Spektrum forlag, 2003.

[34] M. A. Vorotyntsev, L. I. Daikhin, and M. D. Levi. Modeling the impedance properties of electrodes coated with electroactive polymer films. *Journal of Electroanalytical Chemistry,* 364(1-2):37–49, 1994.

[35] L. F. Richardson. The Approximate Arithmetical Solution by Finite Differences of Physical problems Involving Differential Equations, with an Application to the Stresses in a Masonry Dam. *Philosophical Transactions of the Royal Society A,* (210):307–357, 1911.

[36] K. Schittkowski. *Numerical Data Fitting in Dynamical Systems: A Practical Introduction with Applications and Software (Applied Optimization)*. Kluwer Academic Publishers, 2002.

# A   Proof that the impedance can be derived by setting $s = j\omega$ in the Laplace-transform t-space equations

Laplace-transform:

$$\mathcal{L}\{f(t)\}(s) = \int_0^\infty f(t)e^{-st}\,dt = F(s) \tag{A.1}$$

where $s = \sigma + j\omega$ ($j = \sqrt{-1}$). Inverse transform:

$$\mathcal{L}^{-1}\{f(s)\} = \frac{1}{2\pi}\int_{\gamma-j\infty}^{\gamma+j\infty} f(s)e^{st}\,ds = f(t) \tag{A.2}$$

Some simple rules and examples:

$$\mathcal{L}\{t\} = \frac{1}{s^2} \tag{A.3}$$

$$\mathcal{L}\{t^2\} = \frac{2}{s^2} \tag{A.4}$$

$$\mathcal{L}\{\sin\beta t\} = \frac{\beta}{s^2 + \beta^2} \tag{A.5}$$

Applications in differential equations: Transform problem, solve transformed equations algebraically, and then transform back.

For complex equations, the back-transformation is usually quite difficult, and only limiting forms can (at best) be found. Numerical inversion is possible, but unstable. Some algorithms exist, see e. g. Schittkowski [36].

Response to a harmonic driving signal

$$u(t) = \begin{cases} u_0\sin\omega t & : \quad t > 0 \\ 0 & : \quad t < 0 \end{cases} \tag{A.6}$$

Driving signal:

$$u(s) = \frac{u_0\omega}{s^2 + \omega^2} \tag{A.7}$$

Response when the transfer function is $h(s)$:

$$y(s) = h(s)\frac{u_0\omega}{s^2 + \omega^2} \tag{A.8}$$

In t-space

$$y(t) = \mathcal{L}\{y(s)\}^{-1} = \frac{1}{2\pi j}\int_{\gamma-j\infty}^{\gamma+j\infty} h(s)\frac{u_0\omega}{s^2 + \omega^2}e^{st}\,ds \tag{A.9}$$

Residue theorem:

$$\oint_C f(z) = 2\pi j \sum_{k=1}^{N} Res f_{z=z_k}(z) \tag{A.10}$$

If simple poles only:

$$Res f_{z=z_k}(z) = \lim_{\xi \to z_0} (z - z_0) f(z) \tag{A.11}$$

If the transfer function $h(s)$ has N poles ($\frac{u_o \omega}{s^2 + \omega^2} = \frac{u_0 \omega}{(s + j\omega^2)(s - j\omega^2)}$) has two poles in $s = \pm j\omega$

$$
\begin{aligned}
y(t) &= \frac{1}{2\pi} \int_{\gamma - j\infty}^{\gamma + j\infty} h(s) \frac{u_0 \omega}{s^2 + \omega^2} e^{st} ds \\
&= \frac{h(j\omega) u_0 \omega e^{j\omega t}}{2j\omega} + \frac{h(-j\omega) u_0 \omega e^{j\omega t}}{-2j\omega} \\
&\quad \sum_{k=1}^{N} \frac{(s - s_k) h(s) u_0 \omega e^{st}}{s^2 + \omega^2}
\end{aligned}
\tag{A.12}
$$

If we are primarily interested in the steady-state response, then we inspect the expression in Eq. (A.12) when $t \to \infty$

- If all the poles are in the left half of the complex plane, $Re(s_k) < 0$, and the last term (the sum) dies out exponentially.

- If there are any poles in the right half-plane, the system is unstable and will not be interesting from an impedance point of view anyway.

- We therefore assume that $h(s)$ only has poles in the left half-plane.

$$\lim_{t \to \infty} y(t) = u_0 \left[ h(j\omega) \frac{e^{j\omega t}}{2j} - h(-j\omega) \frac{e^{-j\omega t}}{2j} \right] \tag{A.13}$$

Setting (physical systems always have poles symmetrically about the real axis):

$$h(j\omega) = |h(j\omega)| e^{\phi} (-j\omega) = |h(j\omega)| e^{-\phi} \tag{A.14}$$

we get

$$\lim_{t \to \infty} y(t) = u_0 |h(j\omega)| \sin(\omega + \phi) \tag{A.15}$$

---

The steady-state response of the system to a sine stimulus is thus also a sine. The amplitude is scaled by the absolute value of the transfer function. The phase is shifted by the phase of the transfer function.

---

We now assume that $u(t)$ takes the role of a voltage and $y(t)$ that of a current (for example). For electrical and electrochemical systems, the transfer function as written with the argument $s = j\omega$ is defined as the *admittance* of the system:

The *admittance* of an electrochemical system is the ratio of the Laplace-transformed current to the Laplace-transformed voltage. The *impedance* is the inverse of the admittance.

Note that we assumed that there is response linearly connected to the stimulus in the definition of the transfer function. If the experimental arrangement arrangement does not comply with this requirement, the analysis breaks down. In electrochemistry this is usually achieved by applying a small amplitude.